DEPARTAMENTO DE FÍSICA APLICADA
UNIVERSIDAD AUTÓNOMA DE MADRID

HAP/TiO_2 AND HAP/TiN STRUCTURES; SURFACE MODIFICATIONS FOR ENHANCED BIOCOMPATIBILITY

Memoria presentada por: MIGUEL MANSO SILVÁN
Para optar al grado de: DOCTOR EN CIENCIAS FÍSICAS
MADRID, OCTUBRE DE 2001

INSTITUT NATIONAL
POLYTECHNIQUE DE GRENOBLE

INSTITUTO DE CIENCIA DE
MATERIALES DE MADRID

AGRADECIMIENTOS

Al profesor José Manuel Martínez Duart por embarcarse en la pluridisciplinar carrera de los Biomateriales. De façon pareille, au Dr Michel Langlet pour son spécial implication dans touts les travaux accomplis.

A las doctoras Pilar Herrero, Predestinación García y Carmen Jiménez por su posición mas que activa en este trabajo y durante los proyectos paralelos que de ella han surgido. Al Dr José Pérez Rigueiro por su incomparable entusiasmo en todos los trabajos que hemos realizado juntos.

A la Dra Carmen Morant por su disposición en tiempos difíciles. Al Dr Raul Martin por participar en innumerables colaboraciones. Al Dr Manuel Hernández por abrir diversas vías. Al personal del ICMM-CSIC involucrado en esta tésis. Muy especialmente a la Dra Mercedes Fernández por la complicidad que nos une. Al Dr Luis Vázquez por sus iniciativas y detallados comentarios. A Olga Sánchez y José Maria Albella por mantener las puertas abiertas para cualquier discusión. Al Dr Emilio Delgado por la valía de sus exposiciones y por su apertura visual en el tratamiento de los biomateriales.

Au Dr Roland Madar, et à tout le personnel du LMGP-INPGrenoble, pour l'accueil inconditionnel pendant les successifs automnes depuis 1998. Aux Drs Eric Millon et Jaques Perriere de l'Université de Paris VI-VII pour les mesures, analyses et interpretations des spectres RBS.

A todo el personal técnico implicado en el desarrollo de esta tesis. En especial a Graciano Hueso y Rafael Ropero por combinar técnica y arte. A Ángel, Jesús y Adrián por compartir su saber en microscopia electrónica de transmisión. Très spécialement aux Mrs Chadouët et Bochu pour la precision de leur travail. Al personal del SIDI, a Tomás, a José Antonio y a Félix.

A toda una jerarquía de estudiantes de Madrid y de Grenoble por las numerosas sobremesas y otros momentos compartidos. A Gonzalo, Marta, Ripi, Carlos, Luis, Jorge, Lucía, Isabel, Fernando, Ángel, Pepa, Gema, Araceli, Raul, Juan Pablo, Laura . Remerciements très speciaux à l'equipe Aerosol-gel: Caroline, Montse, Alexi, Pierre, Martín, sans oublier la contribution a l'ambience de la part de Patrice, Milan, Igor, Guilhem, Wilfrid, Zeinul, Alexei, Remi, Sandrine, Sebastien, José, Dominique, Marco, Olga, Ben, Cédric... Sin olvidar a la compañía durante mis incursiones en el CBM: Samuel, Jaime, Isabel, Sonia, Eva, Beatriz, ...

A todos los que, sin pertenecer al entorno de trabajo, preguntaron alguna vez por el estado de esta tesis. A los que compartieron los momentos de evasión: Esther, Rubén, Carlos, Enrique, Paco, Alberto... a los triatletas y a los croseros.

A Nils, Fran, Benoît, Pietro, Andrés y Delphine por los meses de convivencia.

A mi familia, por quererme con adoración.

HAP/TiO_2 AND HAP/TiN SRUCTURES;
SURFACE MODIFICATIONS FOR ENHANCED BIOCOMPATIBILITY

CHAPTER I: *GENERAL INTRODUCTION AND OBJECTIVES.*

CHAPTER I: *GENERAL INTRODUCTION AND OBJECTIVES.*

1.1 BIOCOMPATIBLE COATINGS: LATEST ADVANCES AND NEW CHALLENGES.

The field of prosthetic biomaterials has demanded in the last decades a variety of solutions from thin film technology. These films, deposited on the surfaces of structural biomaterials, are designed to make compatible the concepts of bioactivity and fracture toughness. On one hand, the poor mechanical properties of bioactive ceramics do not allow the processing of cast load bearing ceramics [WIL96]. On the other, the surface properties of the metallic alloys traditionally used for these applications need alternative materials to improve the long-term in-vivo stability [LON98]. Bioactive coatings should thus produce an intimate contact with bone tissue and increase the corrosion resistance of the underlying material, which is exposed to highly alkaline conditions. Furthermore, it should minimise friction and wear in order to avoid debris particles, which are at the origin of a high proportion of revision surgeries.

Although the development of highly stable structural materials is far from being the ideal solution for the substitution of failed bone, the actual know-how in bone tissue regeneration and the intensity of several catastrophic damages do not allow a more correct approach. To illustrate the above mentioned deficiencies, a brief description of the bone structure and physiology is mandatory [WIL90, WEI99]. Bone is a biocomposite material formed by an inorganic microcrystalline fibre (70 wt %), an organic matrix (20 wt %) and water (10 wt %). The inorganic part is mainly composed of hydroxyapatite (HAP, $Ca_{10}(PO_4)_6(OH)_2$), which presents numerous substitutions in the structure (CO_3 for OH and PO_4 ions, F and Cl for OH and also Mg, Sr, Na and other alkaline elements in the Ca site). These crystals present a preferential direction of crystallization so that they present a characteristic needle like shape (30 nm x 3 nm). In cortical bone, this allows an axial distribution of the crystals, which remain embedded in a collagen fibre matrix as depicted in figure I.1.1. Both components are arranged in a helical manner forming cylindrical lamellae (5 μm). These structures form at the same the osteon (200 μm) by arrangement of concentric rings leaving an internal canal. This

configuration ensures a high mechanical response in loading, bending and torsional environments. Furthermore, the osteon canals provide the metabolic substances that allow the vascularisation of the structure, which promotes cell activity and thus, bone reconstruction and remodelling. In older humans, the vascularisation is progressively reduced, the organic matrix becomes fragile and the risk of fracture increases.

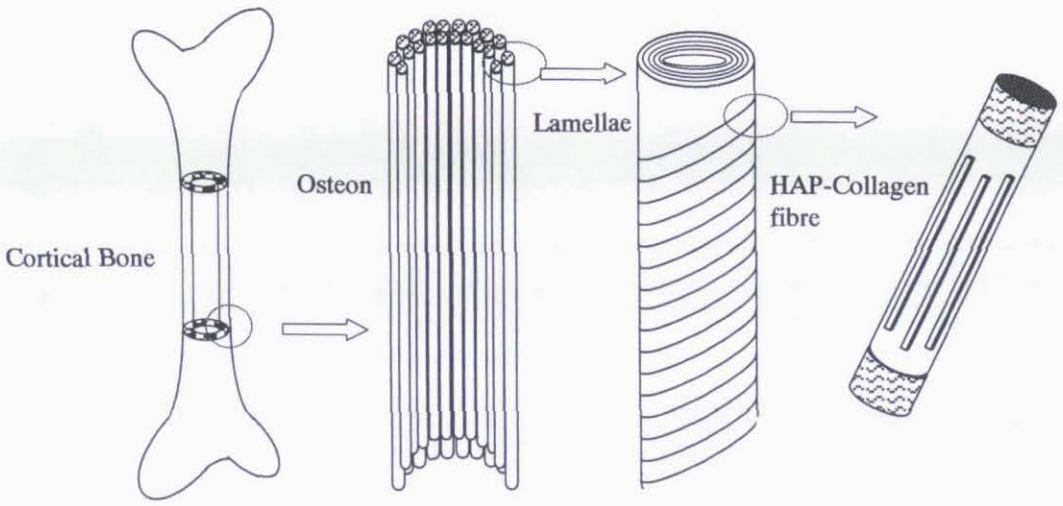

Figure I.1.1: Scaled structure of cortical bone.

At this point, the consequences of inserting in humans a bulk metallic alloy can already be derived. Even though the initial response to the implant may be positive, the absence of a free path for vascularisation will lead to a progressive encapsulation of the implant. In the long run, the response in the form of necrosis, infection and intense pain usually leads to a revision surgery [BUR00].

The tissue engineering solution to the problem of bone structural substitution passes through the preparation of bioactive materials with high resorption coefficients. These compounds should present porous structures and appropriate surface bonds to allow protein scaffolding. As soon as the cell colonies allow the formation of new bone tissue, the material is progressively eliminated by resorption until it becomes extinct [BRO97]. Among the materials with proper resorption properties for the design of new generation prostheses, we have to mention several calcium phosphates (CaP) [RAM91],

polymers [ROK00] and silk [LI99]. CaP and polymer materials have already found applications as biomaterials in drug delivery devices [LAN95].

However, as we have already mentioned, the actual procedure is to introduce a highly stable bulk ceramic or metallic implant. Although the ceramic materials present the advantage of porosity control, it has been shown that they present insufficient mechanical properties (case of HAP) or undesirable biological responses (case of Al_2O_3). Between the most referenced metallic alloys we have to mention CoCr, NiCr, stainless steels and the TiAlV family, which is undoubtedly the most widespread alloy used for biomechanic substitutions. In fact, Ti6Al4V is a light alloy, of good chemical stability and presenting a highly contrasted mechanical response [LON98]. Not in vain, it was initially designed for the aerospace industry. The Al and V atoms, although inserted at low concentrations in the Ti matrix as β phase stabilisers, have been reported to cause biological damage. This is a new reason for designing a passivating outer layer that avoids the direct contact with biomolecules.

Many materials in thin film configuration have been thus proposed as metallic substrate isolators, for example in the cones of hip-joint prostheses. In the case of Ti alloys, the choice of TiO_2 and TiN as protective coatings is the easiest selection ensuring the presence of a passivating layer with a high bonding strength. It is also evident to develop coatings composed of the material that the body synthesises itself, that is HAP. Among other proposed materials we have to mention diamond like carbon (DLC), carbon nitride (CN) [CUI00], silicon carbide (SiC) [ZHO96] and calcium titanate ($CaTiO_3$) [OHB99]. We must also include the group of polymers of ultra high molecular weight that are used in the heads of hip joint prostheses [PAR92].

Within this frame, the activity of the research group in the Department of Applied Physics (DFA-UAM) was initially focused in the development of HAP coatings. A first approach based on an electrodeposition method led to the formation of polycrystalline HAP coatings [MAN00]. In spite of the advantage of low temperature processing, the disadvantage of this technique arose from a limitation in the maximal value of accessible coating thickness, which was determined by the saturation of the

electrical activation. The characterisation of electrodeposited layers by structural, morphological and chemical techniques showed that polycrystalline HAP coatings could be obtained on Si and Ti substrates. The crystals presented several substitutions (principally Na) that led to a Ca/P molar ratio (mr) slightly lower than the value corresponding to HAP (1.67). In any case, the characteristic infrared spectrum of HAP was only altered by the carbonate substitutions in the structure. A study by surface force microscopy (SFM) showed that the coatings were formed by grains with mean sizes of approximately 100 nm (figure I.1.2a). These granular structures conformed surfaces with a lot of topographic variations as shown in the image of figure I.1.2b. Values of root mean square roughness of approximately 50 nm were obtained for scanned areas of 1000x1000 nm^2. The observation of grain boundaries showed the presence of very steep morphologic changes between neighboring grains (figure I.1.2c). An insight view of the granular structures allowed to observe the parallel assembling of the characteristic needle shaped HAP crystals that compose the coating grains (figure I.1.2d).

In this work we have diversified the materials under study to attempt the improvement of both, the surface properties of the metallic alloy and the implant matching to the bone tissue. We have thus selected TiN and TiO_2 coatings for the former and HAP films to accomplish the latter objective. In the most complex application of hip joint prostheses, Ti based thin films with enhanced surface properties should cover the whole prostheses. The HAP coating is only applied to the bone contacting stem, leaving the articular part free (figure I.1.3).

The suitability of TiN and TiO_2 materials for biological applications is not novel [TOR95, HAD96]. We have taken advantage of the previous know-how of the groups in Departamento de Física Aplicada (DFA-UAM) and Laboratoire de Materiaux et Genie Physique (LMGP-INPG) for the processing of TiN [JIM99] and TiO_2 [LAN01] by magnetron sputtering and aerosol-gel techniques, respectively. The mechanical properties and biocompatibility of these coatings will be described herein.

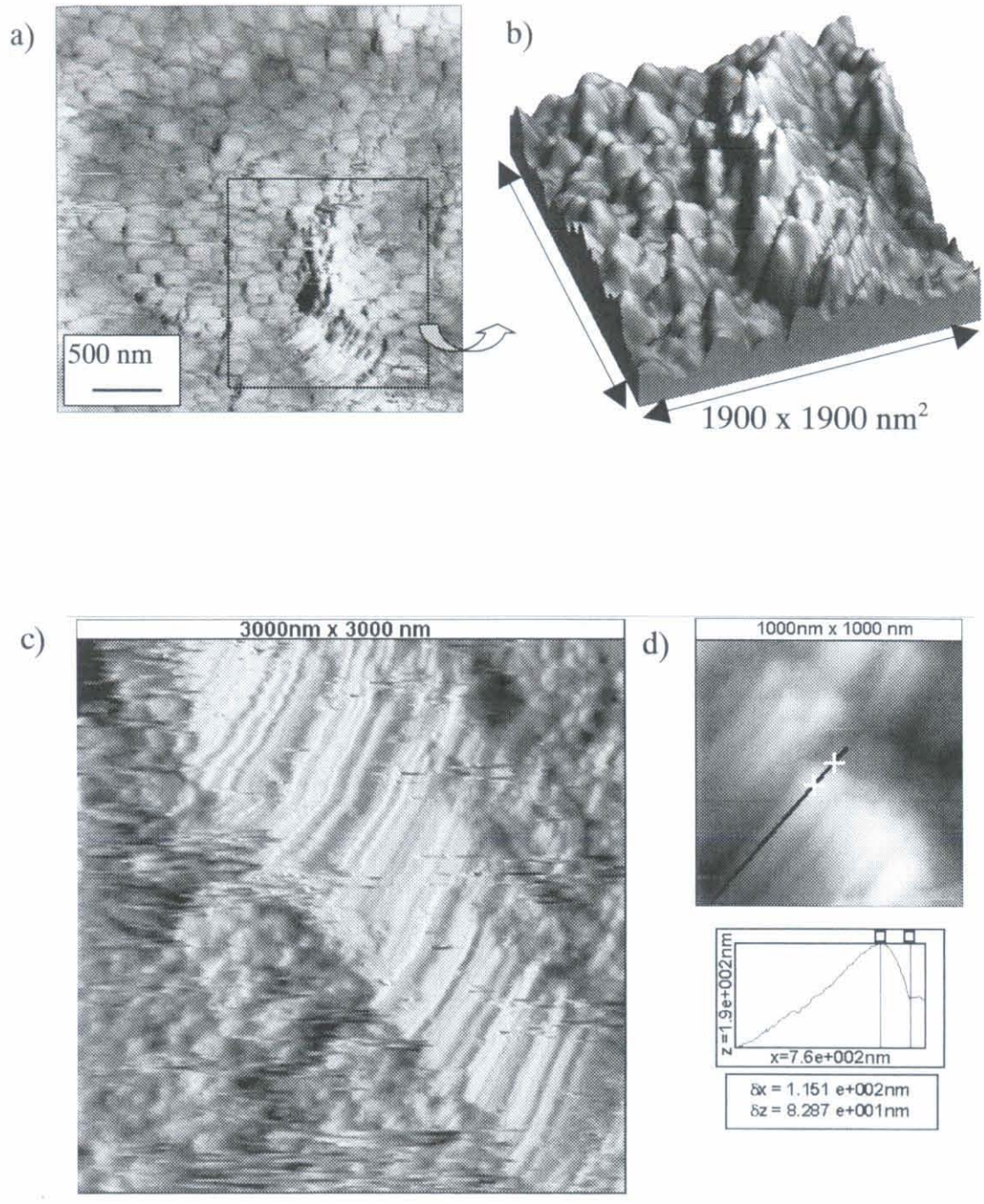

Figure I.1.2: Surface force microscopy images from electrodeposited HAP coatings. a) Friction image revealing general granular conformation. b) Topographic image outlining the surface roughness. c) Steep grain boundaries. d) Insight view of the HAP crystals conforming the HAP grains.

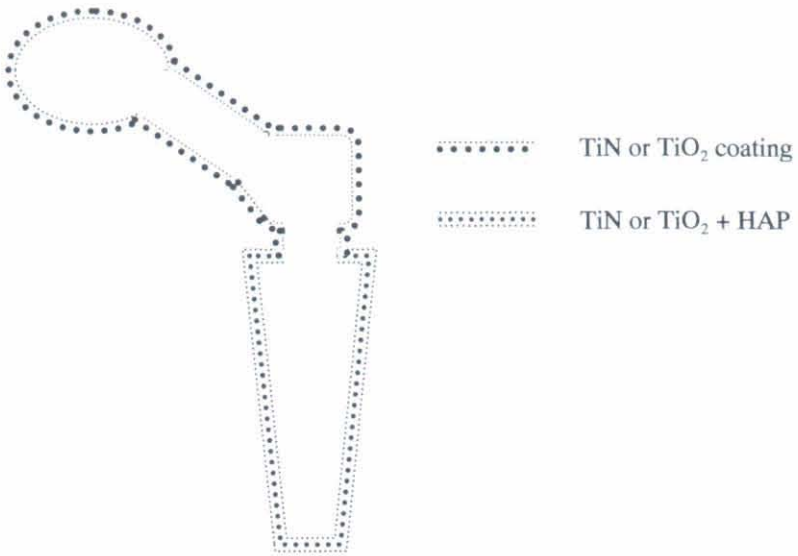

Figure I.1.3: Profile of a hip joint prostheses designed in its articular part with a TiN or TiO_2 coating and with a TiN or TiO_2 + an HAP coating in the bone contacting stem.

Concerning the preparation of HAP coatings, we have adapted the aerosol-gel technique for the processing of these coatings, thus overcoming the thickness constraint found in electrodeposition processing. This adaptation consists essentially in the selection of the appropriate precursors and the determination of the sol parameters that make compatible reactivity and aerosol formation.

In a more general view, the development of biologically active surfaces is not only interesting from the orthopaedic point of view. Surface activation is an old aim in biotechnologies for applications such as tissue regeneration [TEM00], DNA detection [MIR00], biological patterning [BLA98, CUR97], high performance bio-catalysts [KAO99] or the realisation of bioelectronic circuitry [SER99]. This kind of applications requires more complex solutions such as surface activation with biologically functional groups. It involves a scaffolding process from the inorganic substrate to the biological species by intermediate organic layers containing organic groups generally based on S (thioles), N (amines), CO (carboxides), etc. In this work, we have included our preliminary results in the development of surfaces with high densities of amine groups.

1.2 STATE OF THE ART IN TITANIUM BASED BIOCOMPATIBLE COATINGS.

Titania films prepared by diverse methods present promising biocompatible properties. Electrochemically prepared TiO_2 coatings have proved to be highly stable in surgical practice [SZA99]. In addition, sol-gel derived titania coatings have been described to act as apatite nucleation inducers not only *in vitro* but also *in vivo* [LI93]. It has been proposed that the nucleation of the CaP on titania surface is activated by the presence of hydroxyl functional groups in the film [HAD96-2]. Descriptions concerning thickness and morphology effects on the nucleation ability of these films have been reported [HAD96]. The formation of TiO_2 coatings on TiAlV alloys was thus proposed to ameliorate the biocompatibility of load bearing prostheses. The titania coatings present also a barrier function which would avoid the negative effects of Al and V ions released by wear processes over the TiAlV prostheses [LON98]. Furthermore, in vivo studies of the performance of hydroxyapatite coatings (HAP, $Ca_{10}(PO_4)_6(OH)_2$), have shown that failures of the bioactive HAP coatings are mainly produced at the interface with the metallic substrate due to lack of adhesion [HAY94]. Titania coatings can play the role of a protective barrier avoiding the diffusion of these ions into the implant. Both effects, i.e. apatite nucleation induction and diffusion barrier properties, permit to envisage applications for the improvement of metallic load bearing prostheses, even more when a high bonding strength to the commonly used TiAlV alloy is ensured.

The attractive properties of TiN films have recently led to study the biocompatibility of this material. TiN coatings present a high corrosion resistance [HUB93] and improve the wear resistance of high-speed-steels [JAR91]. These two factors are of extreme importance in the field of load bearing prostheses as they determine in the long run the formation of debris, and thus the lifetime of the prostheses. Ti6Al4V alloys, mainly used in prosthetics because of their good mechanical and corrosion performance, have already been coated with TiN. Ion implantation [TOR95,SCH98], PACVD [RIE95] and reactive r.f. sputtering [JON99] techniques have been used to test TiN coatings for biological applications. The former studies showed that the wear resistance was considerably increased by the TiN coatings [TOR95, RIE95] and the corrosion tests carried out by potentiodynamic polarisation in simulated

body fluids showed also a reduction in the breakdown potential [SCH98]. The latter study, comparing the haemocompatibility of different hard coatings, gave advanced performance for diamond like carbon coatings with respect to TiN [JON99]. Other tests performed with TiN biomaterials compared the *in-vivo* and *ex-vivo* interaction of TiN surfaces with leucocytes and the adsorption of proteins [DIO93], concluding that TiN could be considered as a suitable blood contacting material. Concerning the applications in biological media derived from its high electrical conductivity, TiN electrodes with fractal surfaces have been tested for cardiostimulation allowing to monitor the neural response of the myocardium [SCH95]. TiN coatings present also a barrier function on TiAlV alloys, so that they can avoid the above mentioned negative effects of Al and V ions. Furthermore, a high bonding strength to the TiAlV alloy is also ensured.

1.3 QUALITIES OF HYDROXYAPATITE COATINGS.

Hydroxyapatite ($Ca_{10}(PO_4)_6(OH)_2$, HAP) is a material mainly known for its special ability to contact bone tissue. In fact, HAP is part of the inorganic constituent of natural bone, teeth and several coralline biominerals. Although the mechanical properties of bulk HAP only allow applications for small non loaded structures [HEN91], the possibility of depositing it in the form of films has permitted to exploit its bioactive properties in structural prostheses such as for hip joint replacement. HAP coated implants, mainly prepared by plasma spraying, have shown to increase the quality of adhesion of structural prostheses [LAN89] and to reduce particle release from the metal substrate [SOU96], playing therefore an important role in diminishing the number of rejection cases. However, in vivo tests performed on these coatings have shown resorption or lack of bonding strength to the bioinert metallic substrate. These effects are mainly due to the presence of other CaP phases [HUA92] of poor stability in comparison with crystalline hydroxyapatite [RAD92]. Sintering at temperatures higher than 900°C is generally necessary to detect the real phases present in the coating, which depend on the overall stoichiometry of the CaP [ELL94]. High temperature sintering promotes segregation mechanisms so that, depending on the absolute Ca/P mr of the coating, one or more phases different from HAP may be identified in XRD patterns and FTIR spectra. Thus, β-tricalcium phosphate (β-TCP) is formed from Ca deficient HAP

at temperatures below 1200°C while α-tricalcium phosphate is formed above this transition temperature [KIV98]. In addition, sintering at temperatures higher than 800°C induces a dehydroxylation process, which creates vacancies in the HAP lattice [GRO98].

As a result, many other deposition methods have been proposed including magnetron sputtering [YAM94], laser ablation [GUI96], diverse electrochemical methods [RED96, CHE98] as well as several sol-gel assays. Concerning the sol-gel process, various deposition methods have been proposed: dip-coating [BRE92, LI96, WEN99, MAV00], spin-coating [HWA99, RUS96] and powder processing [MAS90, DEP92, JIL99]. In these works, $Ca(NO_3)_2$ is widely used as the calcium source but many different selections have been made for the phosphate inclusion (H_3PO_4, P_2O_5, phenyldichlorophosphine, n-butyl acid phosphate). Besides, the choice for solvent is also varied (ethanol, methanol, acetone, 2-methoxyethanol). An important and common condition selected in all the previous works is the value in the Ca/P mr of the precursor solutions, which was always equal to that of stoichiometric HAP. However, the study of chemical processes that lead to stoichiometric HAP sol-gel formation has not been deeply undertaken. A general study in the system of phosphate precursors is presented by Livage *et al* [LIV92]. Concerning the sol-gel processing of HAP, a formal polymerization route has been presented by Brendel *et al* [BRE93].

1.4 CELLULAR EVALUATION OF BIOMATERIALS.

The evaluation of new generation structural biomaterials is a complicated task that involves an *in vitro* proof prior to long term in vivo testing. The categorisation and classification of several biomaterials has often been carried out in simulated body fluids, which contain no bio-organic specimens. In this frame, the term *bioactive* has been assigned to those materials with a surface able to promote apatite nucleation [LI93]. Titania and silica gels, as well as hybrid preparations are outstanding materials with this property. However, this phenomenon should only be considered as a good catalytic property of the material surface, but does not justify the use of the term *bioactive* according to the conventional classification of biomaterials [HEN82]. It looks therefore

reasonable that biomaterial tests must include more realistic assays with bio-organic species prior to long term in vivo testing. These kind of tests include a wide band of protein adsorption tests [DIO93] and cellular assays covering haemocompatiblity [JON99] and more generally biocompatibility [HEN82]. The most powerful method for the evaluation of the cellular behaviour on biomaterials is the immunofluorescent staining process since it allows an in situ exploration of the cellular behaviour. Concerning the kind of cells used for these assays, there is an increasing interest in the evaluation by using human pluripotent mesenchymal stem cells (hMSCs), which are obtained from the bone marrow of adult individuals. These cells present relevant properties that merit a deeper description.

Pluripotent hMSCs, which are present in the bone marrow, contribute to the regeneration processes of mesenchymal tissues including cartilage, bone, muscle, ligament, tendon and stroma [CAP91, BRU98]. Their differentiation will depend on physical and chemical factors that surround them.

However, several limitations have been evidenced by tissue engineers for the material which serves as support for the differentiation process of mesenchymal cells [ANS00]. It has thus been shown by tissue engineers and surgeons that there is a growing need of producing biomaterials with active surfaces for the development of tissues from hMSCs. Different materials supported by accurate chemical signals can help to induce a variety of differentiation paths that will determine the function of the cell.

1.5 THESIS OBJECTIVES AND TEXT ORGANISATION.

The general introduction has given up to date information concerning the main problems in bone tissue regeneration and repair. From the aspects outlined in the previous sections, it can be derived that the goal of our work is to prepare a biocompatible structure that could overcome the actual deficits of bulk structural biomaterials. In order to ameliorate the surface properties of metallic alloys we propose structures with a passivating TiN or TiO_2 interlayer and a bioactive outer coating

composed of HAP. Taking into account this main objective, we analyse independently the processing and characterisation of the different materials as well as the study of the whole HAP/TiN or HAP/TiO_2 configurations. The overall target of this work can be divided in several tasks according to the different partial objectives. In order to guide the reader in the understanding of the deposition and characterisation techniques used for the preparation and analysis of the different materials, we have included a detailed experimental description in this manuscript (Chapter II). This chapter details not only the experimental conditions that allow the formation and accurate phisico-chemical characterisation of the coatings. We have also optimised an immune staining process to evaluate cell behaviour on these materials. We have already shown in this chapter the interest of both, the method for the visualisation of cells on opaque surfaces and the relevant characteristics of the cells used in these tests, specially in the case of human mesenchymal stem cells.

In order to describe the properties of aerosol-gel derived TiO_2 layers, we have included details concerning the chemical analysis by FTIR. The structural changes of the TiO_2 coatings related to the sintering temperature have been studied by XRD. Morphological features have been described by using SEM. Additionally, the mechanical characterisation of these coatings has been performed by ultra-microindentation. This technique has allowed the determination of the Young's modulus (E) and hardness (H) of the different coatings. It will be shown that the plastic energy of deformation (PED) and the mean indentation creep can be correlated with the physico-chemical properties of the films. Finally, the use of these materials for in-vivo applications requires a preliminary biological exploration, which is part of our partial objectives. Thus, the results from the biological assays performed with human chondrosarcome cells on TiO_2 coatings are also included. All these aspects are presented in chapter III, followed by an equivalent characterisation focussed on TiN interlayers prepared by plasma sputtering. In the case of TiN thin films, the biological tests have been carried out by using pluripotent mesenchymal stem cells.

An important partial objective has been the deep characterisation of CaP coatings in order to verify that our films present the correct physico-chemical properties

of bioactive HAP coatings. A detailed description of the deposition parameters of HAP coatings using the aerosol-gel process is included in chapter IV. A complete characterisation by chemical, structural and morphologic techniques allows to derive the differences of the coatings produced from different PO_4 precursors. Concerning the mechanical characterisation, the adhesion strength between the HAP grains is tested by means of ultra microindentation. Finally, we present the results of the biological characterisation performed by testing the adhesion of human mesenchymal stem cells.

As we have already mentioned, the main goal of this work is to prepare mixed structures by combining HAP coatings and Ti based layers. The physicochemical description of biocompatible bilayers with configurations HAP/TiO_2, HAP/TiN is carried out in chapter V. A special attention is paid to their characterisation by surface and interface spectroscopy (Auger electron spectroscopy AES, Rutherford Backscatering RBS). These tools facilitate a deep characterisation of the interface allowing to extract conclusions concerning specially diffusion aspects. Structural as well as morphological information from the surface and interface has been obtained by transmission electron microscopy (TEM) cross section images, and surface force microscopy (SFM) topographic images.

Concerning more general studies for biological applications, it has been part of our work to develop an appropriate scaffold to increase the specific attachment of bio-organic species to the surface of any material. In this manuscript, we have included our preliminary results concerning the surface functionalisation by sol-gel fixation of amine groups. The use of an hybrid sol increases the condensation rate of an aminosilane by including a more reactive metalorganic titanante. We aim to study the evolution of the amine composition on the surface by varying the sol stoichiometry and inducing the condensation at different temperatures. Biological tests of the surface functionalisation have been performed with a genomic application rather than with cell adhesion tests. All these aspects are presented in the self contained chapter VI.

At the end of this manuscript, we present a compilation of the most significant results derived from the different experimental chapters. A summary concerning the

properties of the different materials is presented followed by a proposal of application. These latter conclusions are presented in chapter VII.

Finally, we outline that the present study has opened new research lines that will merit our attention in forthcoming investigations. These perspective works are summarised in chapter VII.

CHAPTER II: *EXPERIMENTAL TECHNIQUES.*

CHAPTER II: *EXPERIMENTAL TECHNIQUES.*

A DEPOSITION TECHNIQUES.

In this section, we present the most relevant features of the deposition methods employed in this work. On one hand, the potentiality of the sol-gel process for the formation of solid oxide films and on the other, the suitability of Physical Vapour Deposition (PVD) for the processing of a variety of dense layers and, for what we are concerned, the deposition of nitride thin films.

2.1 THE SOL-GEL PROCESS.

2.1.1 Introduction.

The sol-gel method has become a very extended technique for the processing of a wide variety of materials in diverse configurations. In order to get a general overview, including the diversity of the applications, the reader is encouraged to read the most referenced guide in sol-gel processing [BRI90]. The basis of the sol-gel reaction is the inorganic polymerisation at room temperature of an oxide network by means of a wet route. The chemical variables that control the polymerisation process allow the preparation of monolithic glasses, fibres, thin films or nanopowders that can be processed with a high control of the stoichiometry, structure and morphology.

Concerning the applications of sol-gel derived materials to thin film technology, we have to cite recent studies performed at Laboratoire des Matériaux et du Génie Physique, Institut Nationale Polytechnique de Grenoble (LMGP-INPG) concerning optical antireflective multilayers [BUR01] and integrated waveguides or light amplifiers [COU00], as well as ferroelectric $BaTiO_3$ coatings, which have been processed in the Departamento de Física Aplicada, Universidad Autónoma de Madrid (DFA-UAM) [MAN01]. New applications in the lithographic field are being explored at LMGP-INPG by preparing hybrid inorganic-organic layers [TRE00]. To illustrate the range of applications of the sol-gel method, we can further mention its use for the preparation of

transducer materials for gas sensing [ZUS90], superconductor YBaCuO [MAS91], ferromagnetic oxides [YAM88], piezoelectric titanates [JIM88], transparent conducting ITO thin films [ARF84] and bioactive glasses [CHE99], among many other functional materials.

2.1.2 General aspects of the sol-gel transition.

The sol-gel process involves the inorganic polymerisation of a sol that leads to the formation of an oxide network. An initial monomer or oligomer precursor can derive to the formation of a gel or a precipitate. The gel is produced when neighbouring precursor molecules link to form associated clusters that determine a continuous solid structure enclosed by a continuous liquid phase. If the precursors present a high reactivity due to intrinsic or environmental characteristics, the polimerisation rate is high enough to produce dense and strongly crosslinked particles that precipitate in the solvent. Precipitates and gels present relevant structural differences, illustrated for example by different fractal dimensions [KOL85]. Dense precipitates present identical fractal and Euclidean dimensions while gel products present a fractal dimension much lower than 3.

From an experimental point of view, the precursor is diluted in a solvent (generally alcohol). Two kinds of precursors can be used.

- Inorganic precursors, usually metallic salts (nitrates, chlorides, sulphates), which react in aqueous media. In our case, calcium nitrate will be used for the processing of HAP coatings.
- Metalorganic (MO) precursors, which comprise a metal linked to an organic radical reacting in aqueous media. The most commonly used MO precursors are alkoxides, where the metal is linked to alkyl groups. For the deposition of our TiO_2 films, the alkoxide tetraisopropyl-orthotitanate (TIPT) has been employed.

The precursor solution polymerises through hydrolysis and condensation reactions. The partially polymerised solution is called a sol. In a first step, the

preparation of a solution in the presence of water leads to an hydrolysis reaction. For instance, in the case of a Ti alkoxide solution:

$$Ti\,(OR)_4 + H_2O \rightarrow OH\text{-}\,Ti\,(OR)_3 + ROH \qquad (1)$$

Where OR is an alkoxy radical.

Depending on the quantity of water, the hydrolysis reaction can be partially or totally completed. Hydrolysed molecules are then involved in condensation reactions, leading to oxygen bridging bonds. These reactions can liberate either a water or an alcohol molecule by means of an oxolation or alkoxolation reaction, respectively:

$$(OR)_3\,Ti - OH + OH\text{-}\,Ti\,(OR)_3 \rightarrow (OR)_3\,Ti - O\text{-}Ti\,(OR)_3 + H_2O \qquad (2)$$

$$(OR)_3\,Ti - OR + OH\text{-}\,Ti\,(OR)_3 \rightarrow (OR)_3\,Ti - O\text{-}Ti\,(OR)_3 + HOR \qquad (3)$$

Both hydrolysis and condensation reactions proceed together at room temperature and lead to an inorganic oxide network. These reactions involve phenomena that can be explained in terms of nucleophile addition and substitution mechanisms. These mechanisms are intimately linked to the presence of polar bonds in the polymer and thus, to the electronic configuration of the mediating mineral element. A nucleophilic substitution involves a previous nucleophile addition of the X-OH group over the nucleophile metal (a). A proton is then transferred to the OX radical (b). This charge transfer sets the nucleofuge radical free (c). For instance in the case of titanium:

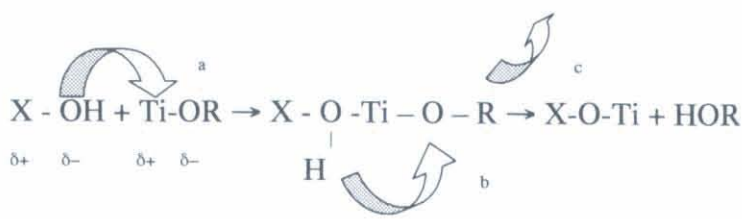

(4)

These substitution reactions are the most common in the sol gel transformations that lead to the formation of TiO_2. In equation 4, X=H in the case of an hydrolysis reaction and X=Ti in condensation reactions.

When the sols are exposed to drying conditions, solvent evaporation is induced, leading to the formation of a dry gel called xerogel. The volume reduction factor during xerogel formation depends on chemical variables such as pH, precursor concentration, water to precursor molar ratio, etc. These factors can also determine the kinetics of the transformation. Drying and polymerisation cannot be analysed independently in the case of a fast thin film or fibre processing (i.e. a few seconds) but can be followed by rheological techniques in the case of a slow monolith formation (i.e. days).

Drying is generally a critical stage, since capillary stresses are induced by the liquid evaporation. These stresses tend to reduce the sample porosity. In drastic cases (e.g. amorphous to crystalline transitions induced by thermal annealing), capillary forces can also induce the xerogel fracture.

2.1.3 Transition metal alkoxides: titanium case.

From a general point of view, alkoxides are the most expanded sol-gel precursors due to their adaptable reactivity for hydrolysis and condensation reactions. Titanium alkoxides are not always present in the form of monomers. In these precursors the coordination number, which is higher than the oxidation state, is not completely satisfied. To enhance the coordination of the metals, oligomerisation processes are induced, which take place preferentially via alkoxy bridging. In this frame, titanium ethoxide and titanium butoxide present oligomeric structures but Tetraisopropylorthotitanate (used in this work) remains monomeric.

The chemical behaviour of similar alkoxides (identical organic groups) can be extremely different and require specifically adapted experimental procedures. As an introductory example, for the deposition of titanates the sols are prepared taking care of avoiding a too fast and hardly controllable polymerisation. In the case of silicate films, the precursor reaction is catalysed to ensure a faster and homogeneous condensation process of the poorly reactive precursors. These differences can be directly related with the behaviour of the alkoxide in nucleophile substitution reactions. The polar bonds in

the organic precursor drastically depend on the electronegativity of the atoms involved in the bond. In order to quantify the intensity of the polar distributions, Henry and Livage [LIV88, LIV89] have applied the Partial Charge Model, which relies on the principle of equilibration of electronegativities due to orbital charge transfer. An atom involved in an heterogeneous bond presents a positive or negative partial charge δ_i. The charge transfer remains in equilibrium when all the atoms in the molecule reach the mean electronegativity of the molecule χ_m. Then the partial charge of an atom is defined by:

$$\delta_i = \frac{\chi_m - \chi_i^o}{k\sqrt{\chi_i^o}} \qquad \chi_m = \frac{\sum_{i=1}^{n} p_i \sqrt{\chi_i^o} + z}{\sum_{i=1}^{n} p_i / \sqrt{\chi_i^o}} \qquad (5,6)$$

Where the parameters χ_i^o, p_i, z and k represent the electronegativity of the i atom, the stoichiometric coefficient of the same atom, the total charge of the molecule and a constant of the electronegativity scale (Pauling, k= 1.36), respectively.

In table II.1.1 we list the values of the "metal" partial charge of several ethoxides as presented by Livage [LIV88, LIV92]. It appears that Ti alkoxides present preferential properties towards nucleophile reactions (i.e. a high positive partial charge of the metal) and are thus much more sol-gel reactive than, for instance, silicon or phosphorus alkoxides.

Precursor	**$Zr(OEt)_4$**	**$Ti(OEt)_4$**	**$Nb(OEt)_4$**	**$Ta(OEt)_4$**	**$V(OEt)_4$**	**$Si(OEt)_4$**	**$PO(OEt)_3$**
δ(M)	+0.65	+0.63	+0.52	+0.49	+0.46	+0.32	+0.13

Table II.1.1: Values of the partial charge of several transition metals in their tetraethyl alkoxide configuration.

Condensation reactions are often controlled by means of catalysts or inhibitors of the nucleophile substitution reactions. Depending on the pH, choice of the solvent or use

of a chemical additive, a series of mechanisms can take place. In the case of Ti alkoxides, it is essential to control their high reactivity. In fact, they precipitate in water even at very low concentrations. Acid or base catalysts play a key role in determining the hydrolysis vs condensation mechanisms. Acids are used to favour the last step of hydrolysis reactions by the protonation of the substituted species. If sufficient water is added the hydrolysis will be completed. On the opposite side, the condensation is retarded. Furthermore, acid catalysts tend to form extended rather than highly branched polymers, which is an advantage for the formation of thin films and monoliths.

The selection of the solvent for titanium alkoxides plays also a relevant role since it influences the chemical composition of the precursor, through exchange reactions, and thus modifies the polymerisation rate and structure of the final material. In particular, monomer or oligomer precursors, formed by alkoxy bridging, can be tailored by using the same precursor but different solvents.

2.1.4 Sol-gel processing of phosphates.

In the view to prepare HAP coatings through a sol-gel route, the sol-gel chemistry of phosphate precursors appears to be a key problem. The little information concerning this branch of materials is undoubtedly influenced by the low sol-gel reactivity of PO_4^{3-} ions (i.e. a weakly positive partial charge of phosphorus in alkoxy environment). However, some precious data can be found in [LIV92]. Even though there are structural similarities between silicate and phosphate materials (i.e. tetrahedral SiO_4^{4-} and PO_4^{3-} units), their solution chemistry is very different. Phosphate materials cannot be synthesised at room temperature from $PO(OR)_3$ or $PO(OH)_3$ sols. It has been shown that $PO(OR)_{3-x}(OH)_x$ sols are the most effective for the sol-gel synthesis of Ti phosphates and mixed silica phosphate glasses since the hydrolysis of $PO(OR)_3$ is very slow and the use of $PO(OH)_3$ leads to precipitates.

In order to form $PO(OR)_{3-x}(OH)_x$ from phosphate triesters, one may expose the precursors to basic conditions in aqueous media, which lead to $PO(OR)_2(OH)$. When

using phosphoric acid as a precursor, the condensation of an orthophosphate can be achieved by the following nucleophile substitution reaction:

$$2\ PO\text{-}(OH)_3 \rightarrow (OH)_2\text{-}OP-O\text{-}OP(OH)_2 + H_2O \qquad (7)$$

This oxolation reaction is mainly governed by the partial charges of the phosphorus atom and hydroxyl group, which should fulfil the following conditions for condensation to occur: $\delta(OH)<0$, $\delta(P)>3$. Table II.1.2 shows that, reducing the pH to increase the negative partial charge of OH groups, produces a deprotonation of the phosphate and thus a reduction of the phosphorus positive partial charge. That states again the impossibility of room temperature sol-gel condensation of this kind of precursor.

Precursor	**pH**	**δ(P)**	**δ(OH)**
H_3PO_4	+	+.035	0
$H_2PO_4^-$		+0.19	-0.2
HPO_4^{2-}	-	+0.03	-0.48

Table II.1.2: Values of the partial charge of the phosphate and hydroxyl groups in the totally and partially protonated precursors (pH dependence) [LIV92].

To overcome these constraints, we will show in chapter IV how the complexation power of phosphate anions towards metal cations can be beneficially used to form HAP mixed precursors

2.1.5 Traditional sol-gel deposition techniques.

The application of sol-gel chemistry for the processing of thin films was initially envisaged by using traditional methods of liquid solution deposition (dip- coating, spin-coating). The sol-gel deposition process can be divided into three steps although the first two steps can take place simultaneously:

1. Substrate covering with the reactive sol.

2. Solvent evaporation together with hydrolysis- polycondensation reactions leading to an adherent xerogel film.

3. Elimination of organic groups and solvent traces, usually by a thermal treatment.

These steps take place in a different manner depending on the deposition method. We give as a reference the steps that concern the commonly used dip- and spin-coating:

a) Dip-coating: The dip-coating procedure is based on the immersion of a substrate in the reactive sol and its subsequent slow removal (few cm/min). The dip-coating procedure can be depicted according to a four-step model (Figure II.1.2): I) immersion, II) removal, III) coating and draining, IV) evaporation and reaction.

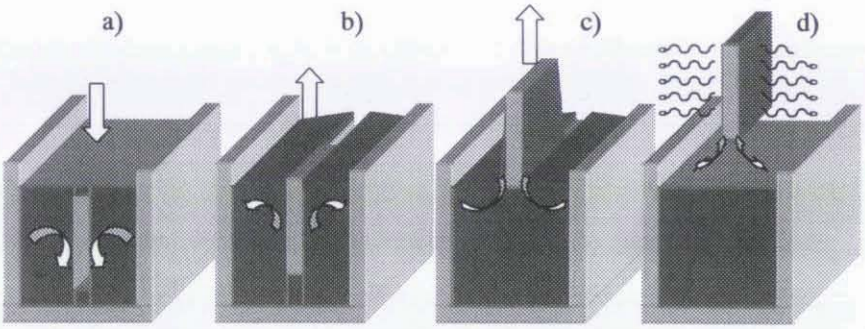

Figure II.1.2: The traditional sol-gel dip coating deposition technique.

The film thickness is determined by viscous friction and gravity mechanisms, so that the principal parameters controlling the thickness are the removal speed and the fluid properties (density, viscosity, surface tension). This technique is mainly adapted to substrates with axial symetry.

b) Spin-coating: The principle of spin-coating deposition is based on the centifuge spreading of the sol on a rotating substrate (several thousand rpm). The spin-coating deposition can be summarised by a three-step model (Figure II.1.3): I) deposition of an excess of sol, II) rotation of the substrate allowing a conformation of

the coating by evacuation of the extra sol, III) evaporation and reaction. The forces that determine the coating thickness are the viscous friction and the centrifuge force. In this case, the thickness for a given sol can be controlled by varying the angular speed (or even the angular acceleration) and the fluid properties. This technique is mainly adapted to substrates with radial symmetry.

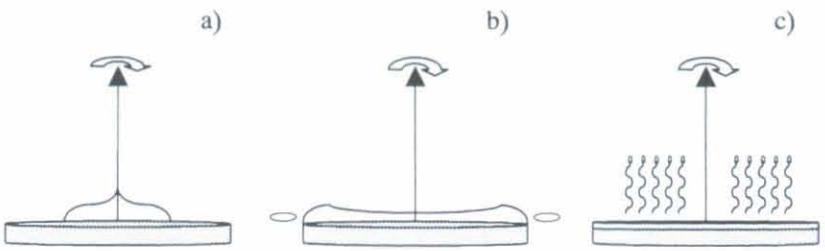

Figure II.1.3: The traditional sol-gel spin-coating deposition technique.

2.1.6 The Aerosol-gel process.

The aerosol-gel deposition used in this work for the processing of TiO_2 and HAP coatings is a development of the sol-gel procedure compatible with the main advantages of CVD (continuous in-time deposition process). Thus, this technique is well adapted to on-line technologies for low cost mass production. Moreover, the aerosol-gel procedure allows a further control of the deposition conditions than the traditional sol-gel techniques, since liquid deposition and evaporation steps do not overlap. In fact, it introduces the principle of atmosphere selectivity in the deposition chamber. Finally, films can be deposited on substrates without axial or radial symmetry or even over three dimensional structures. This is an important aspect when considering the need to coat orthopaedic implants with complex shapes. This process has been developed and patented at LMGP/INPG [LAN91].

The aerosol-gel process is based on the ultrasonic nebulisation of an aerosol from a reactive sol-gel solution. The aerosol, constituted of micro droplets, is driven onto the substrate where the droplets spread and coalesce, leading to a liquid film. After deposition, drying and sol-gel polymerisation take place, forming a xerogel film that can be then heat-treated. To obtain a visual idea of the process, a schematic view of the

reactor is presented in Figure II.1.4. Detailed information concerning the design, development and evolution of the aerosol-gel process can be obtained elsewhere [VAU98].

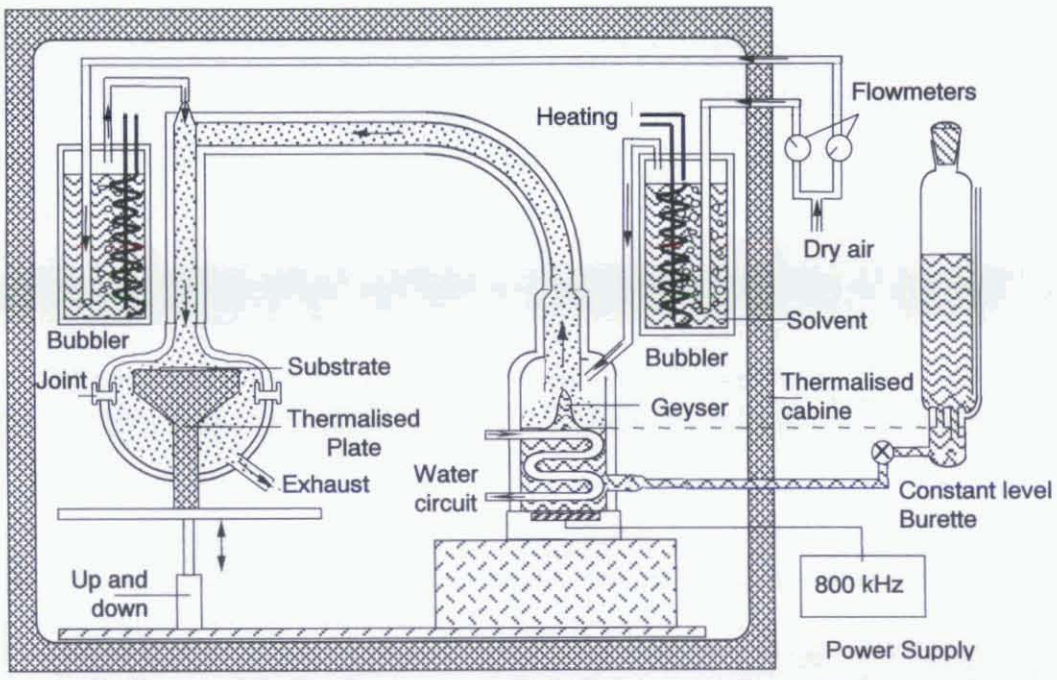

Figure II.1.4: The configuration of the aerosol-gel reactor.

The aerosol-gel deposition can be divided into four steps.

a) Aerosol formation: The sol is pulverised in a chamber consisting of a glass vessel, a water circulation cooling system and a piezoelectric transducer. The piezo is excited at its resonant frequency (800 kHz) and the wave propagation through the liquid induces the formation of an aerosol at the liquid/gas interface. Vibration and cavitation are the two responsible mechanisms for aerosol formation. The pulverisation efficiency is all the more important as low viscosity solutions are used. Taking into account that the sols used in this work are strongly diluted in ethanol, we can ascertain that the aerosol is formed by microdroplets (≈5-10 μm in diameter) [HID70, VAU98]. The thermalised water circulation plays a relevant role in avoiding a temperature increase, due to ultrasonic agitation, that may induce premature evaporation and sol-gel reaction of the liquid.

b) Aerosol transport: The reactive aerosol is then transported with an air flux previously saturated with the solvent used to dilute the precursor in the solution (ethanol in this work). This avoids solvent evaporation, increase of species concentration and subsequent premature reaction of the droplets during transport, which would lead to a detrimental liquid viscosity increase. For the same reason, the temperature of the transporting tube is also controlled at 20°C by maintaining the whole reactor in a thermostated chamber. Finally, the premature reaction control is more efficient as lower reactive sol-gel solutions are used.

c) Liquid film deposition: The flux of microdroplets covers the substrate forming a liquid film through droplet spreading and surface coalescence mechanisms. Coalescence is based on the minimisation of the liquid energy by reduction of the total surface area. This mechanism is detrimentally inhibited when highly viscous solutions are used or when the liquid viscosity increases during transport. Thus, the film uniformity depends closely on the solution properties (low reactivity and viscosity) and control of the transport conditions. When the aerosol production is stopped, the saturated gas flux is maintained until the last microdroplets are evacuated, preventing at the same time any evaporation from the liquid film. The film uniformity depends also on the deposited droplet quantity, i.e. the aerosol transport duration, and of course, on the substrate surface itself. For the reactor used in this work, the minimum aerosol flux duration needed to obtain an homogeneous liquid film (total coalescence) from standard sols has been estimated to be 20 s. A maximal thickness (deposition time) limitation is also imposed by film homogeneity constraints. When the liquid film thickness exceeds a given threshold, liquid flow occurs at the film surface, which alters the thickness uniformity. The range of times that allow the deposition of homogeneous and optical quality thin films have been studied at LMGP for solutions with different precursor concentrations [VAU98].

d) Xerogel film formation: To induce the evaporation stage, two procedures have been studied. One can either introduce a dry air flow within the deposition chamber or just open the chamber and put the substrate in contact with the cabinet atmosphere. The

evaporation will activate the standard sol-gel mechanisms. In order to obtain desired physico-chemical properties, the xerogel may be then thermally treated to induce film densification or crystallisation. It has to be noted that thick films can crack during drying or heat-treatment, due to capillary stresses. This is another reason to limit the maximal film thickness. After drying and heat-treatment, uncracked homogeneous films with a maximal thicknesses in the range [200 – 500 nm] can be obtained, depending on the deposited material. Thicker films (1 micron or more in thickness) can be obtained using a multilayer deposition procedure, i.e. repetition of deposition / heat-treatment cycles.

To begin with a deposition, the transporting tube must be in thermodynamic equilibrium (solvent saturation of the reactor). Hence, before a session of depositions, the aerosol is preliminarily transported during 10 min, after what the reactor is exposed for 10 min to a solvent saturated air flow. Then the deposition procedure can begin.

Between two consecutive deposition experiments, the saturated gas is again transported during 10 min through the vessel, tube and chamber in order to recover the reactor saturation (partially cancelled during the post-deposition drying period). At the end of a deposition series, a fast and easy cleaning of the saturated reactor is performed by injecting the solvent using a high pressure gas inlet.

2.1.7 Deposition parameters: TiO_2.

TiO_2 coatings were deposited considering that highly viscous solutions (for instance, due to a high precursor concentration or reactivity) are not easily transformed into an aerosol. Therefore, a 0.4 M tetraisopropyl-orthotitanate (TIPT, Fluka chemicals) solution diluted in ethanol with a TIPT/water molar ratio r_w= 0.82 and a pH= 1.27 was prepared [BUR01]. This solution exhibited a moderate reactivity and low viscosity (2 cP) compatible with aerosol-gel process implementation.

Silicon wafers (100) were used as substrates for the deposition of titania coatings. TiAlV plates were used for biocompatibility tests. Before deposition, the Si

wafers were treated in air at 500°C for 2h to eliminate adsorbed impurities and to form a thermally stable SiO_2 surface film.

The coatings were formed by following the next steps: I) A **pre-pulverisation** step (no gas sweeping) during 10 s in order to obtain a steady state aerosol. II) The ultrasonically nebulised aerosol was **transported** during 20 s by an ethanol saturated air flux into the thermally regulated deposition chamber (20°C). III) **Purge**: The piezoelectric transducer was switched off, while the flux of saturated gas was kept during 1 min until the microdroplets were fully evacuated. IV) The derived liquid films were then allowed to **dry** and to polymerise in air (open drying). Alternatively a dry air flow could be applied (in-situ drying).

The so-formed xerogel films were sintered in air at 150, 300, 500, and 800°C for 1 hr in a conventional furnace. After heat-treatment, the film thickness was about 100 nm. In order to prepare thicker TiO_2 films (about 1 micron thick), a multilayer deposition procedure was followed, i.e. the deposition/ heat-treatment cycle was repeated ten times and the film was heated at 150, 300, 500 or 800°C for 10 min before deposition of a new single-layer. The final coating was then sintered for 1h at the temperature used for the intermediate treatment. In these pages, the film nomenclature refers to the sintering temperature (i.e. TiO150, TiO300, TiO500 and TiO800).

2.1.8 Parameters for HAP deposition.

We have prepared aerosol-gel HAP coatings by using sols elaborated from two different phosphate precursors (phosphoric acid, PhAc H_3PO_4 and triethylphosphate TEP $(C_2H_5)_3PO_4$). The chemistry of these two precursors is extremely different and so are the procedures followed for the preparation of the sols. The sols preparation is considered as a part of the results of this thesis so that we will not justify herein the choice of these parameters (see chapter IV). It is important to mention that in the case of HAP we are interested in producing films with high surface areas, so that the deposition step could be made longer than for TiO_2 coatings.

a) TEP precursor: Sols were prepared from calcium nitrate ($Ca(NO_3)_2.4H_2O$) and triethylphosphate (TEP, $(C_2H_5)_3PO_4$) diluted in absolute ethanol. Here again, the solution preparation conditions were optimised to produce low viscosity solutions: solutions with a Ca concentration of 0.625 M and P concentrations of 0.375, 0.78 and 1.25 M were prepared to obtain the following Ca/P mr: 1.67, 0.8 and 0.5. The precursors were diluted separately in ethanol and, after mixing together, solutions were heated for 24h at 60°C. Such solutions were found to have a viscosity below 2 cP, compatible with the ultrasonic pulverisation of an aerosol.

b) PhAc H_3PO_4: These sols were prepared from calcium nitrate ($Ca(NO_3)_2.4H_2O$) and phosphoric acid (H_3PO_4) diluted in absolute ethanol. The H_3PO_4 1 M solution was prepared at room temperature by continuous slurring. The solution temperature was observed to raise moderately during this process. The calcium dissolution was also prepared at 1 M concentration and stored during 2 h at 60°C in order to stabilise it. The precursor was prepared by mixing different volume ratios of the calcium and phosphate dissolutions (Ca/P= 10/5, 10/6, 10/7). They were added in a high frequency ultrasound vase (800 kHz) following an analogous path to the procedure previously described for the formation of rare earth phosphates [GUO96]. The observed precipitate was vigorously resuspended and stabilised at natural pH of 1.8 during 2 h. The final suspension was filtered and the powders and sols were stored independently. The so-prepared sols presented also values of viscosity compatible with the ultrasonic pulverisation of an aerosol.

Silicon wafers (100), previously treated at 500°C for 2h were used as substrates for the primary study. As we will see in chapter V, the best performing coatings in terms of HAP formation were also deposited on TiAlV, TiN and TiO_2. Aerosol-gel deposition was performed as follows. A steady state aerosol production was reached through preliminary excitation of the solution for 10 s without gas sweeping. Then, the aerosol was conducted into the deposition chamber during three minutes by an ethanol saturated air flux. Homogeneous liquid coatings were thus obtained over the silicon substrates. The coatings were then stabilised at 500°C for 5 min. This treatment was performed immediately after liquid film deposition, i.e. before the formation of a xerogel film. The

choice of such a procedure will be detailed in chapter IV. A multilayer deposition procedure was followed. The aerosol coating/ stabilisation procedure was repeated up to ten times in order to obtain films of approximately 5 μm in thickness. The multilayer coatings were finally sintered for 15 min at 500, 650, 800 and 1000°C in a conventional air furnace. The coatings are defined with respect to the Ca/P molar ratio (mr) of the solution and film sintering temperature (T). The nomenclature used is CP-mr-T (for instance *CP-167-800* refers to a coating formed from a solution with *Ca/P=1.67* and sintered at 800ºC).

2.2 MAGNETRON SPUTTERING.

2.2.1 Introduction.

In this section we present the basis of the deposition technique used for the formation of TiN coatings. The reactive planar magnetron sputtering process has been the main deposition tool of several PhD thesis at DFA-UAM [JIM89, PER95, GUT99]. These works, as well as more general bibliography [WAI78], have been used for this brief description.

2.2.2 Technical features of the sputtering deposition method.

Planar magnetron sources, as well as ion getter pumps, were late technical developments after the discovery of the sputtering principle by Penning. In a dc planar magnetron sputtering system, a cathode containing the target material is faced parallel to an anode substrate holder (grounded or biased). The cathodes present two asymmetrically polarised magnets (electric or permanent) in such a way that the magnetic field lines will have a component parallel to the cathode surface (Figure II.2.1). Positively charged particles in the plasma, Ar^+ cations in our case, will be then accelerated to the cathode.

The collision will produce sputtering (ejected atoms due to collision and Ar insolubility) and secondary electrons from the cathode will be trapped in the plasma

describing trajectories determined by the magnetic field (magnetron) and electric field (anode-cathode). This confinement due to the helical trajectories enhances the ionisation and therefore the sputtering yield, which also depends on the anode-cathode difference of potential (20- 1000 V).

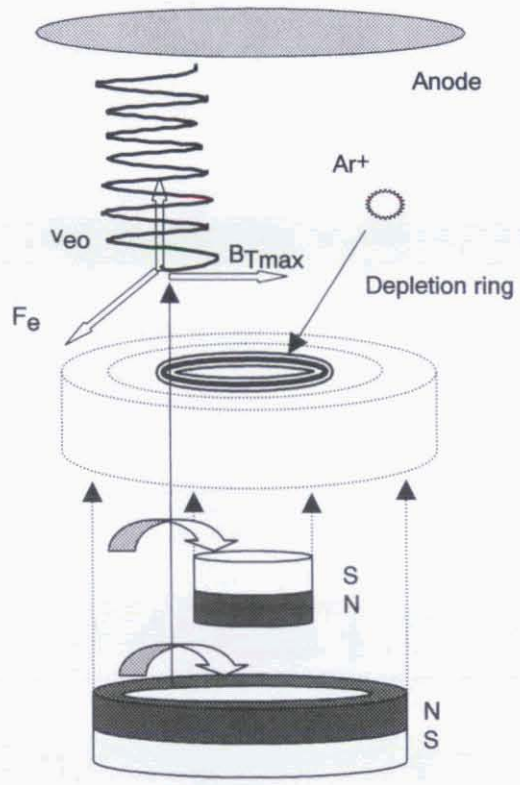

Figure II.2.1: Sputtering process and schematic mounting of a planar magnetron cathode faced parallel to the substrate anode.

Concerning the preparation of cathodes, they should be free of voids and bubbles since these defects favour local melting (lack of dissipation sites) and hence, spitting rather than sputtering is produced. To avoid fracture, the cathode must be stress free since the electromagnetic field and ion collisions will accelerate crack propagation. One disadvantage of the planar cathode configuration is that the target is preferentially eroded where the transverse magnetic field is maximum (B_{Tmax} depletion ring, Figure II.2.1), thus producing a V shaped profile that shortens cathode life. Furthermore, it complicates the inherently nonuniform deposition of planar magnetron. This uniformity can be only guaranteed when the planar magnetron radius (r) is much smaller than the cathode-anode distance (l). Increasing l reduces the growth rate, so a compromise must

be found depending on the coating application. Of course, the deposition rate depends also on the electric power, source material and chamber pressure. Generally, the current I can be expressed as an n power of the voltage V so that the total power can be expressed as follows:

$$I = kV^n \qquad P = kV^{n+1} \tag{8}$$

As we have previously mentioned, the anode may be biased in order to reduce electron charging. This becomes another relevant factor for evaluating the deposition rate, since charging will prevent further electron bombardment (specially for insulating substrates).

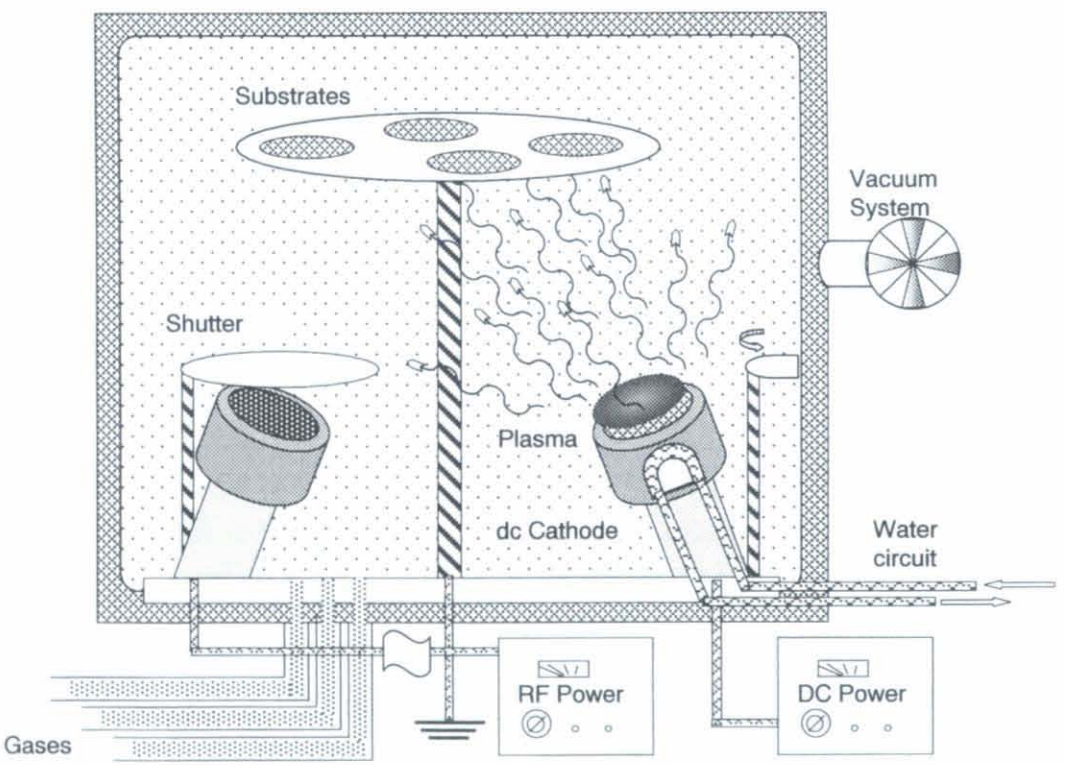

Figure II.2.2: General view of a double cathode planar magnetron sputtering.

The use of an rf source in the cathode (10-30 MHz) enables targeting non conductive materials. Although the electrons are in principle highly bonded,

neutralisation of the surface charge is made by electron bombardment during the positive part of the RF cycle. The possibilities are further increased when a reactive gas is included in the chamber (reactive sputtering) or by using heterogeneous targets. In this latter case, the stoichiometry conservation of the deposited film is not factual if one of the species is volatile. The preferential sputtering can not be corrected by the increase of the concentration of the element with lower sputtering efficiency. In this frame, for the deposition of Si_3N_4 films, an hybrid configuration (reactive sputtering + Si_3N_4 cathodes) has been usually used [GUT99]. In our system, two disk shaped cathodes allow the simultaneous deposition from two different targets increasing even more the processing possibilities (Figure II.2.2).

2.2.3 Parameters for the deposition of TiN coatings.

The TiN coatings prepared in this work were obtained by using high purity titanium targets (Kurt J Lesker, 99.99%) in an Ion-Tech system equipped with two planar magnetrons. Two pre-sputtering periods of 30 min were applied (i.e. shutter covering the substrate) to clean the target material and achieve a steady reactive atmosphere. During a first period there was no N_2 in the atmosphere and the second was performed with 30 sccm Ar and 3.4 sccm N_2. Five depositions of 30 minutes on grounded Si (100) or TiAlV substrates with a total sputtering power of 300 W (typically 600 V and 0.5 A DC supply), Ar/N_2= 9/1 atmosphere and chamber pressure of $1.5.10^{-3}$ mbar led to TiN coatings approximately 1 μm thick. The films were allowed to cool in Ar atmosphere during 1 h.

The coatings where then sintered by rapid thermal annealing in an SHS 100 (AST elektronik, München) in a N_2 atmosphere at 300, 400, and 600ºC. For this treatment, a 5 min plateau was applied after 3 min vacuum (10^{-2} mbar) and 5 min N_2 purge. The temperature ramp was in all cases about 50ºC/s during heating and was not controlled during cooling in N_2.

B CHARACTERISATION TECHNIQUES:

2.3 CHEMICAL TECHNIQUES.

2.3.1 Auger electron spectroscopy (AES).

Auger electron spectroscopy is an analytical technique with high sensitivity for the exploration of the first atomic surface layers. In an Auger event, electrons are ejected from the atoms with energies < 2 keV. The escaping electrons are strongly absorbed so that only those originated at the first atomic surface layers can escape and be detected by an outside analyser. In the following paragraphs we present the most relevant aspects of Auger electron spectroscopy [CRI91].

The Auger process initiates when an atom is ionised (f.i. in its K shell) by an incoming primary electron. The created hole can be filled by the de-excitation of a higher energetic electron (L_1). The released energy can be either emitted as a photon or given to another electron (L_{23}) which is ejected from the atom (Auger electron). Hence, the Auger process implies a final state of double ionisation. The whole process is depicted in figure II.3.1.

The energy of the Auger electron for an element with atomic number Z can be calculated from the diagram of figure II.3.1. Taking into account the work function of the analyser Φ_A and the correction of the Auger level due to previous ionisation, one can obtain an expression for the measured energy. Going on with those levels depicted in figure II.3.1, it is accepted that the energy of the excited L_{23} level is equal to the value for the L_{23} level of a corrected next heavier element $Z+\Delta$. We can therefore write:

$$E(Z)= K(Z)- L_1(Z)- L_{23}(Z+\Delta)-\Phi_A \qquad (9)$$

This equation can be solved by consulting atomic single ionisation tables. In general, the same applies to transition families LMM, MNN, ... etc.

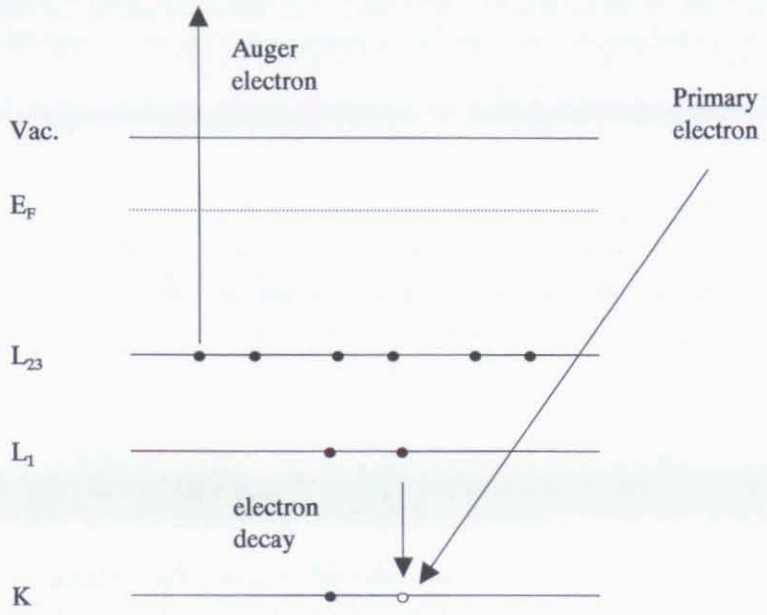

Figure II.3.1: An Auger process induced by the ionisation of a K electron, de-excitation of an L_1 electron and ejection of an L_{23} electron.

By representing the energy distribution of secondary electrons N(E), one can identify Auger peaks associated with plasmon and ionisation losses (Energy loss spectra). In any case, the Auger spectra are usually presented in a differential form to exacerbate the relatively small but sharp Auger peaks from the intense quasi-constant background of secondary electrons. The minimum of this differential spectra N'(E) is almost always more intense, so that it is a convention to attribute this energy as the correspondent to the Auger transition. The higher sharpness of the lower side of the differential spectrum is due to the presence of more electrons in the low energy part of the distribution due to energy loss mechanisms. These features are depicted in figure II.3.2.

Concerning technical requirements, vacuum pressures $<10^{-9}$ Torr should be attained in the chamber to minimise the presence of adsorbed impurities (mainly CO_2, H_2O) that would react and adsorb on the surface during electron bombardment. The Auger equipment should include a gas inlet network and an ion gun, indispensable for surface cleaning and obtaining depth profiles by inert gas ion bombardment of the surface. For these depth profiles, it is important to consider that the original roughness

of the surface can be one of the most important factors that limits the "in –depth" resolution. In general this is lower than about a 10 % of the roughness of the film surface over sampled areas. Concerning the analysers, a lot of technical efforts (electric vs magnetic detection, different geometries, etc) have been devoted to develop analysers with improved signal to noise ratios.

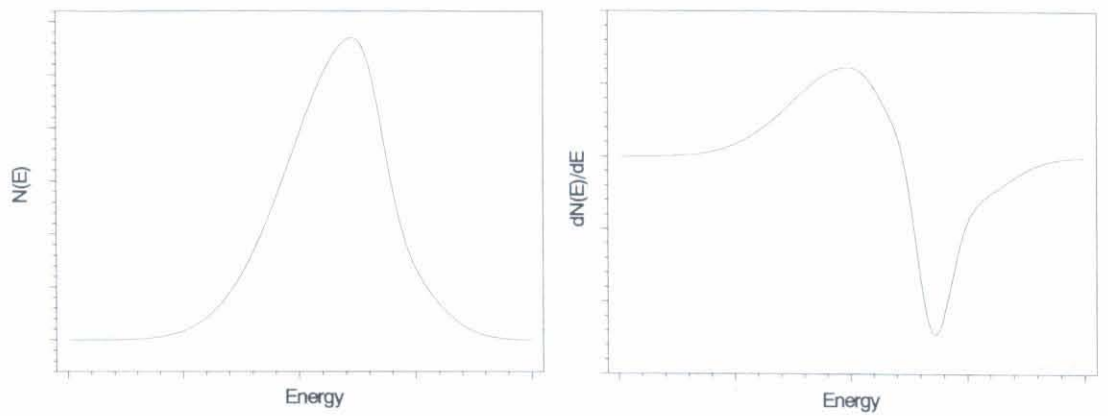

Figure II.3.2: General view of the electronic distribution in an Auger peak N(E) and its differential representation dN(E)/dE.

Another relevant feature of this spectroscopy is that Auger electrons from the valence band are relatively sensitive to the atom environment, so that structural (fine structure peaks related to crystallinity) and chemical bonding conclusions (energy shifts due to variations of electron affinity) can be extracted from Auger spectra.

Quantitative analysis from Auger spectra can be derived from the phenomenological equation that gives the current I_i due to the Auger transition i:

$$I_i = I_p \rho X_i D B \phi \psi_i R T \qquad (10)$$

where these interrelated factors represent the excitation beam current (I_p), atomic density (ρ), normalised atom concentration (X_i), escape depth (D), backscattering factor (B>1, correction to the single event consideration), ionisation cross section (ϕ),Auger

transition probability (ψ_i), surface roughness factor (R), and instrumentation transmission (T).

This equation has led to the study of the sensitivity factors that allow direct evaluation of atomic quantification. Nevertheless, we have not made use of them but we have based our analysis of HAP on a comparison with a standard material.

In our case, Auger spectra were obtained in a JEOL system (JAMP-10S, e^- probe diameter 0.1 mm, 5 KeV) on HAP coated TiAlV plates (with and without TiO_2, TiN intermediate coatings) as well as on a HAP standard (Strem chemicals). For stoichiometric comparisons (Chapter IV), the spectra were recorded after 5 min Ar^+ bombardment (2 KeV, 2x2 mm^2 rastered area). In order to obtain depth profiles revealing the composition evolution at the interface (Chapter V), spectra were recorded every 6 min for a total of 350 min.

2.3.2 Rutherford backscattering spectroscopy (RBS).

The interpretation of the energy of the backscattered particles (i.e. H^+ or He^{4+} at ~MeV) after collision with a target material, enables to extract information concerning the probed material, generally without producing damage to the sample. The spectra are related to the scattering cross section and kinematic factor of the elements in the sample, which gives a characteristic profile to the spectrum of the compound [CHU78].

In the range of energies and ion particles used for RBS we can describe the two body ion-atom collision within the framework of classical theory since we are outside the relativistic and quantum mechanical regimes (high energy limit) and molecular interactions (low energy regime). This allows to extract several kinematic relations that describe particle behaviour as a result of the collision (see figure II.3.3).

These equations are usually derived in the centre of mass system (CMS) but they can be transformed to the laboratory system (LS) by using the appropriate transforming

relation. The elastic collision consideration fits fairly well experimental results so that the transformation from one system to another can be determined.

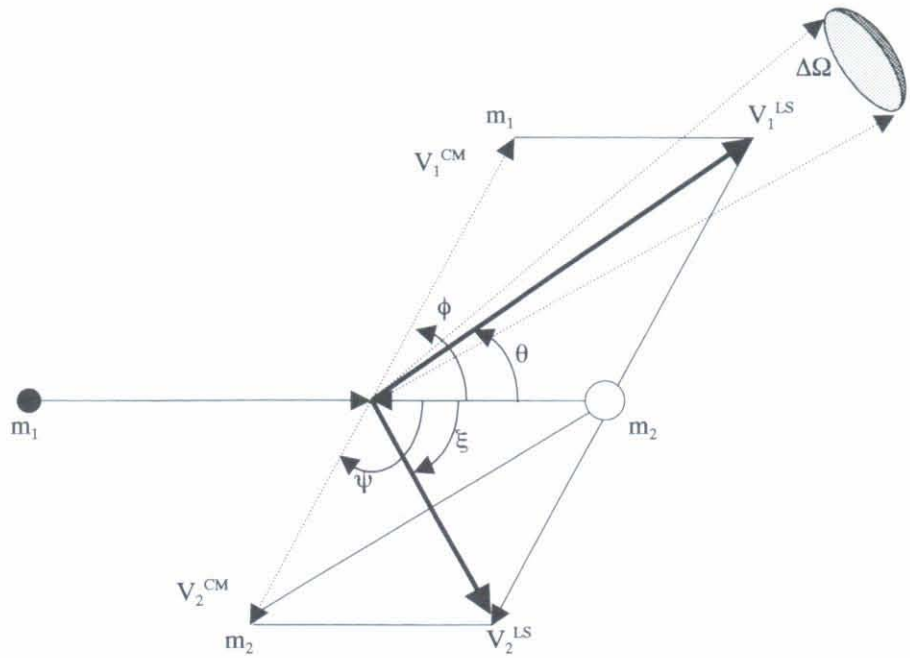

Figure II.3.3: Vector diagram for the derivation of the kinematic relations. Laboratory System (LS), Centre of Mass system (CM), ϕ scattering angle (CM), θ scattering angle (LS), ψ recoil angle (CM), ξ recoil angle (LS).

In the elastic collision consideration we can obtain the analytical expression that relates the energy of the outgoing particle (scattered (E_s) or recoiled (E_r)) as a function of the energy of the incident beam E_o and detection angle θ or ξ, for backscattered or recoiled particles, respectively (kinematic factor, K).

$$K_s = \left[\frac{\cos\theta \pm \sqrt{\mu^2 - \sin^2\theta}}{\mu + 1}\right]^2 \qquad K_r = \frac{4\mu}{(\mu+1)^2}\cos^2\xi \qquad (11)$$

In these expressions μ is the relation between the mass of the target atoms and that of the incoming particle (m_2/m_1). In general, one can be interested in analysing the energy of the incident particles after backscattering and uses light elements in the beam (higher μ relations) since, for a given angle, mass separation decreases with m_2.

Alternatively, one determines the energy of atoms from the sample that are recoiled after a collision with a beam of heavier ions (induce recoiling). These are the basis of RBS and Energy recoil detection analysis (ERDA), respectively. In the case of RBS, the kinematic factor K can be used to determine the energy of an ion backscattered by a specific surface atom. We have to state that only a small fraction of the incident ions will be backscattered so that the efficiency of the detector and a good configuration are key factors in the design of the experimental set up.

At this point, we are interested in describing the dependence of the number of backscattered particles as a function of the scattering angle (cross section). Considering abrupt changes in the trajectories and a Coulomb potential (again a good approximation in this range of energies since, the interaction is dominated by the electrostatic repulsion between the target element and the ions of the beam), one can derive the expression for this cross section (ϕ is the backscattering angle in CMS):

$$\sigma(\phi) = \frac{1}{4}\left[\frac{KZ_1Z_2e^2}{2E_o}\right]^2 \frac{1}{\sin^4\left(\frac{1}{2}\phi\right)} \tag{12}$$

This is the well known Rutherford cross section formula, which presents a quadratic dependence on the atomic numbers of the ion beam Z_1 and target material Z_2. The number of detected particles N_{det} can be then calculated after transforming to the LS:

$$N_{\det} = N_{ion}N_{target}\varepsilon \int_{\Delta\Omega} \sigma(\theta) 2\pi \sin\theta d\theta \tag{13}$$

where N_{ion} is the ion beam density, ε the detector efficiency and $\Delta\Omega$ the subtended detector solid angle around an angle θ (see figure II.3.3).

The RBS spectra provide a distribution of the concentration of backscattered particles as a function of their energy. If we remain in the previously mentioned regimes

(i.e. ~1 MeV for H^+ or He^{4+}), we can neglect electronic and nuclear stopping. The RBS spectrum can be then modelled by calculating the yield at a certain energy as a function of the stopping power and scattering cross section of the elements present in the sample. The stopping power is intimately related to the depth, so that a profile distribution for a certain element can be obtained. All these factors and relations have been included in RUMP [DOO85]. This interactive computer tool allows the simulation of the spectra by a trial and error procedure.

In the example depicted in figure II.3.4, an element A present at the surface of a sample will be detected at an energy K_AE_o (no stopping influence) and will produce a background as determined by the in-depth stopping power (I). A lighter element B, also present at the surface, will be also detected at an energy K_BE_o with a background equivalent to its corresponding stopping power (II). This background is reduced if its stoichiometry is also reduced in the sublayers (III). Another element C, lighter than A but heavier than B, will not appear in its K_CE_o if it is not present at the surface, but at an energy shifted by the mean stopping power of the previous films (IV). This example has been simulated for a 500 nm thick SiO_2 coating deposited on a MgO substrate (A → Si, B → O, C → Mg).

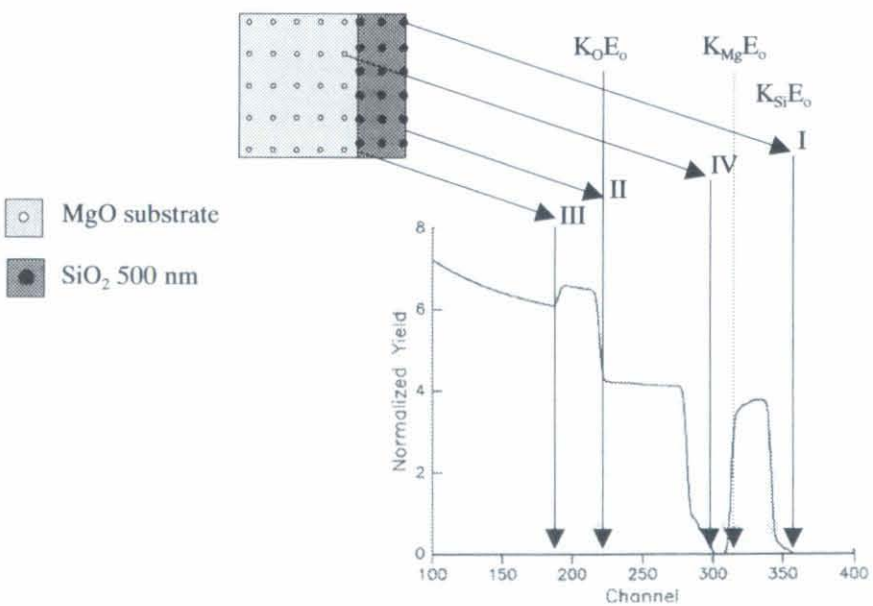

Figure II.3.4: Analysis of a simulated RBS spectrum from a 500 nm thick SiO_2 coating deposited on a MgO substrate.

In our case of HAP coatings deposited on Si with and without TiO_2 and TiN interlayers, the films were analyzed by Rutherford backscattering spectroscopy using a $^4He^+$ beam at 1.82 MeV. The surface obtained after subjecting the structure to a chemical etching with acetic acid (HAc) was also investigated by this technique in order to reach the ceramic-metaloxide interface. The experiments were carried out in the accelerator of the Groupe de Physique des Solides, Université Paris VI, VII.

2.3.3 Fourier Transform Infrared Spectroscopy (FTIR).

FTIR spectroscopy is a technical development of the traditional infrared spectroscopy. It is based on the measurement of the power density and optical path, which form a Fourier pair with the light intensity and wave number of the electromagnetic radiation. The traditional IR systems have been thus substituted by more sophisticated equipment based on Michelson interferometers (figure II.3.5). The beam, originated at the source S, interacts with a beam splitter. The transmitted part is driven to a moving mirror that allows the variation of the optical path δ. The reflected beam reflects on a fix mirror so that the beams meet again, transmitting an intensity signal to the detector D. In this way, by varying the optical path, one can register the interference pattern.

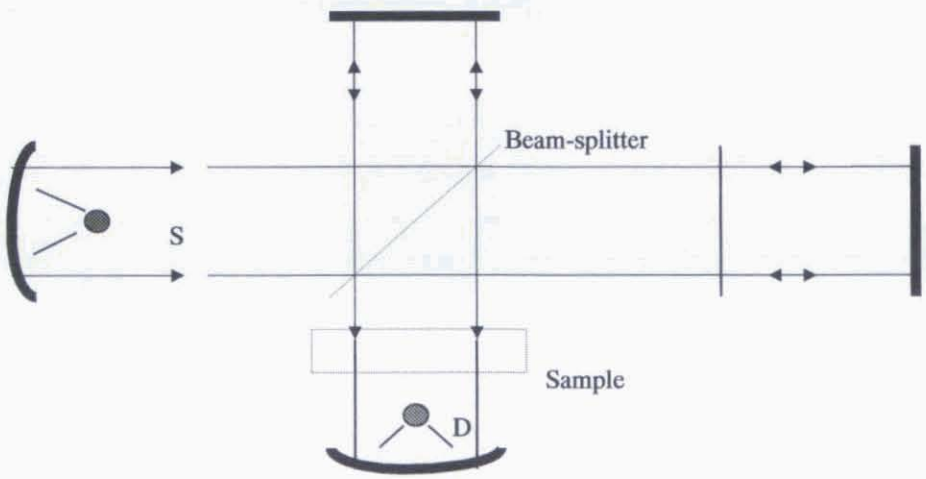

Figure II.3.5: Schematic representation of the Michelson interferometer, fundamental element in the Fourier Transform Infrared Spectrometer.

The active bands of different materials can be assigned to vibration or rotation modes related to bonds between two or more atoms in the structure. Many of these vibrational modes can be calculated by solving the harmonic oscillator equations in the classical theory. However, only the quantum theory is able to reproduce the whole discrete spectrum.

TiO_2 and HAP coatings were intensively studied by transmission FTIR measurement. The electrical conductivity of TiN induces a high reflectivity of light in the whole infrared region. This excludes the use of a transmission tool for the characterisation of the TiN coatings prepared in this work. Only at low temperatures it is possible to detect a weak band at 1037 cm^{-1} [FRO81]. The spectra of HAP and TiO_2 coatings were recorded using a Bio-Rad FTS165 spectrometer (100 scans at 20Hz, 4cm^{-1} resolution). The Si substrate contribution was subtracted from the spectra for the analysis of the different coatings.

2.4 STRUCTURAL AND MORPHOLOGICAL TECHNIQUES.

2.4.1 Transmission Electron Microscopy (TEM).

The principle of TEM is the projection of the contrast image produced by the interaction of a monochromatic electron beam (100-1000 KeV) with the atoms of a thin sample (100 Å) [GOO88, BEE81]. The microscope is basically composed of an electron gun (thermoionic or field emission) and a series of electromagnetic lenses inserted in a high vacuum chamber. These lenses control the electron beam diameter and convergence angle, providing an homogeneous ion flux until they are focussed in the detector (luminescent foil, photographic paper, digital camera). The process of image formation is depicted in figure II.4.1 for both a magnified image and an electron diffraction diagram.

Images and electron diffractograms are implicitly obtained, as derived from figure II.4.1. Two beams from the object (specimen) are projected forming a diffraction

pattern in the back focal plane and finally an inverted image in the intermediate lens. Depending on the intermediate lens selection, a reoriented image (left) or diffraction pattern (right) are formed.

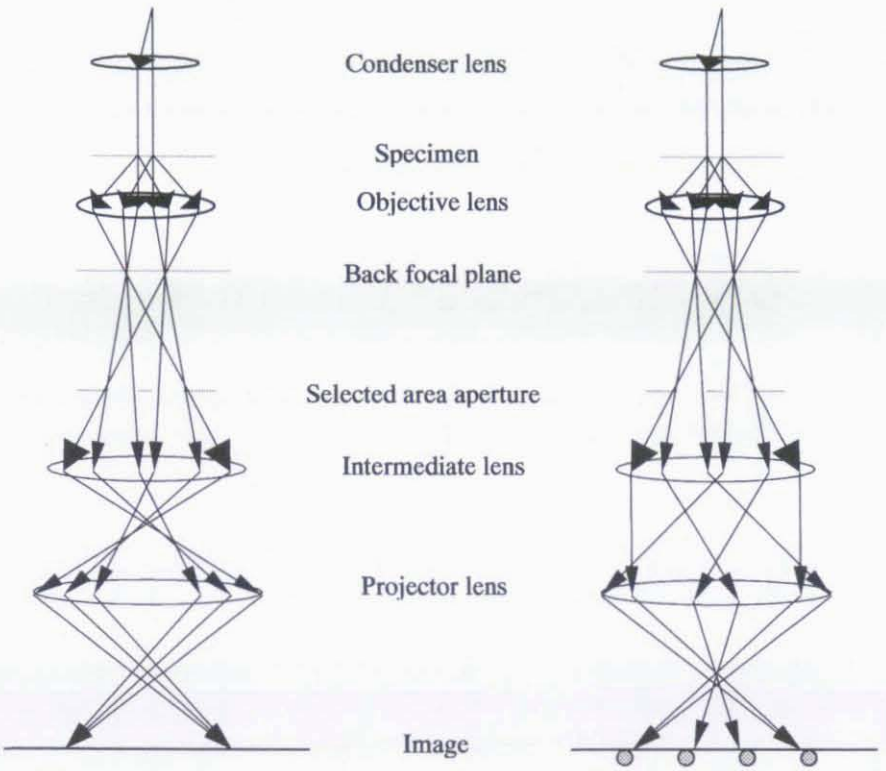

Fig II.4.1 Beam diagram in the system of lenses of a TEM producing focussed image (right) and diffraction planes (left).

The image resolution depends on the microscope characteristics (electron beam energy, stability, aberrations) and on the sample itself (thickness, composition). The least resolved distance is determined by the expression:

$$\Delta x \cong 0{,}6 C_s^{1/4} \lambda^{3/4} \qquad (15)$$

where C_s is the spherical aberration coefficient and λ is the electron wavelength calculated by the relativistic transformation from the acceleration voltage. This suggests that higher voltages are of increasing interest although the limitation is in the technical development of the electromagnetic lenses and beam stabilisers (i.e. do not increase C_s).

The electron diffractograms are intimately related to the structure of the samples. In fact, they form a Fourier pair so that they can be obtained the one from the other by a Fourier transformation. When the wave vector ***k*** of the electrons coincides with a ***g*** vector in the reciprocal space (Fourier space), it produces a preferential deflection of the electron beam according to Bragg's law. It is evident that those periodical ***g*** vectors only exist for crystalline materials. In the low angle approximation the Bragg condition can be simplified knowing that $\sin\theta \sim \theta \sim r/2L$, where θ is half the angle between the incident electron beam and the diffracted electrons, r is the distance between the spots corresponding to the diffracted and incident beam and L is the chamber length.

$$n\lambda = 2d_{hkl}\,\mathrm{sen}\,\theta \qquad n\lambda = 2d\theta \qquad \lambda = d\frac{r}{L} \Rightarrow rd = L\lambda \tag{16}$$

The factor $L\lambda$ is a constant during the diffraction process so that the interplanar distances d_{hkl} of the crystal can be directly obtained by measuring inter-spot distances. When an electron beam interacts with a single-crystal, a spot diagram is obtained and the spot distribution depends on the crystal structure and incident axis (zone axis, usually referred with square brackets []). Each one of the spots refers to a plane of the crystal which are identified by using normal brackets ( ). When a polycrystalline sample is analysed, arbitrary orientations are dominant (multiple zone axis are active at the same time with even several crystals rotated for each zone axis) so that the number of spots increases conforming a ring pattern. If the material is amorphous, the incident beam finds no preferential orientations so that a diffuse electron distribution is obtained.

In our work, TEM observations were performed with a JEOL 2000 FX II, 200 kV on both thin film cross sections and scraped particles (HAP). The preparation procedure of TEM cross sections is presented in annex I.

2.4.2 X-Ray diffraction (XRD).

X-ray sources in diffractometers are generated by the deceleration of electrons colliding with an anode supplied at 10-30 KeV. Characteristic Kα emission is the most

intense due to the higher ionisation cross section of the K shell and higher probability of the lower energy relaxation transitions. These lines are generally monochromatised and act as probe X-ray beams in the traditional diffractometers.

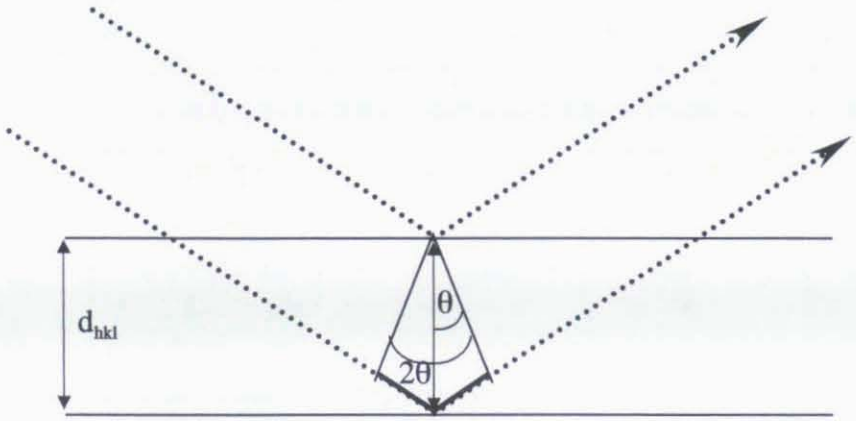

Figure II.4.2: Geometric representation of Brag's law.

A diffracted beam arises from constructive interferences of beams with the same wavelength. The Bragg law (14) regulates the conditions that lead to these interferences in crystalline solids (figure II.4.2).

XRD has been used as an essential technique to obtain structural information and phase identification of the different sample series (TiO_2, TiN, HAP). The samples were analysed with a Siemens D5000 with CuKα radiation in the θ/2θ configuration. If not otherwise mentioned the scan step was 0.04° with 6 s integration time. Samples deposited on Si(100) were tilted by an angle of 0.5° in order to minimise the single crystal substrate contribution.

2.4.3 Surface Force Microscopy (SFM).

The obtention of surface force microscopy images relies on the measurement of interactions between a microtip and a surface, taking into account the elastic deformation of the tip cantilever [MAY92, RUG90]. The sample movement can be precisely controlled by the piezoelectric base so that the tip can scan two dimensionally the surface features. In general, the interaction forces can be resolved up to distances of

100 nm, so that Van der Waals dipole-dipole interactions, ferromagnetic domains and electrostatic interactions can be studied in detail. The tip-sample interactions are interpreted by analysing the laser reflection on the back of the cantilever (or alternatively by interferometric measurements). These reflections can be detected by a diode and converted into an electric signal. The calibration of these signals allow the transformation to the final image. Figure II.4.3 shows a scheme of a SFM apparatus.

In the contact operation mode, the tip is forced to remain at a constant deflection during the scanning of the surface, so that the cantilever corrections reveal the morphology of the area. A four quadrant photodiode allows not only the detection of the vertical shift (topographic image), but also the torsion of the lever (friction image).

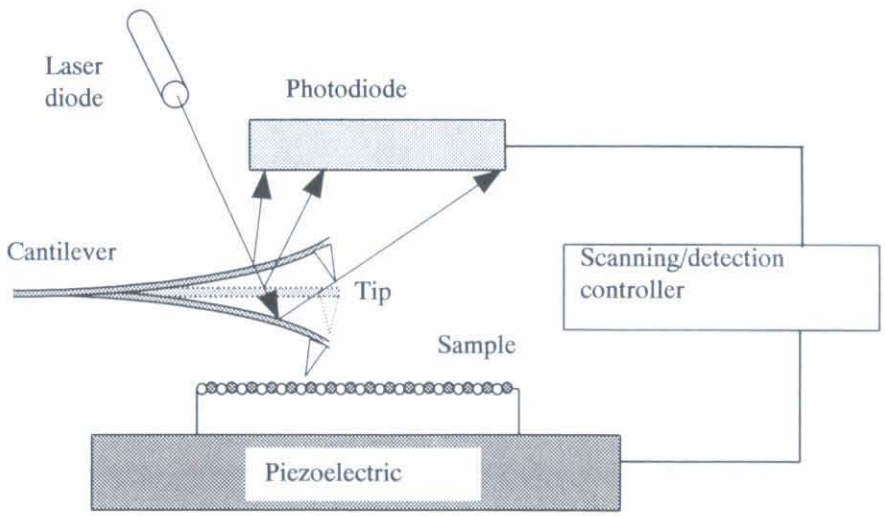

Fig II.4.3 Operational scheme of a SFM with reflective light detection.

In contact modes, the interaction force between the tip and the sample can be generally calculated in the elastic approximation:

$$F = C.\Delta z \qquad (17)$$

where C is the normal force constant and Δz is the lever shift from the rest position.

In non contact modes equation (17) is corrected since the oscilation is forced to explore the surface with a constant amplitude. In this case, a topographic variation

induces a change in the amplitude that can be used to obtain the image. In the most usual tapping mode, a frequency near to the resonance is selected by applying a piezoelectric transducer. In this case, the normal force constant is modified to $C = C_o + F'$, where F' is the force gradient. In this way, an attractive force induces the reduction of the resonant frequency ($f_r \propto \sqrt{C_o - F'}$).

In our SFM measurements on HAP/TiO_2, HAP/TiN and HAP/Si structures, surface features were revealed at a scale not reached by SEM, which is limited by electron charging processes. For these measurements, the tip-surface scans were performed using a Nanoscope III operated in tapping mode.

2.4.4 Scanning Electron Microscopy and Energy Disperse X-ray Microanalysis (SEM-EDX).

SEM microscopes take advantage of the high sensibility of the secondary electrons to surface features. This allows to reveal the sample morphology after excitation with an electron beam (≈ 10 KeV). Observations were performed systematically in HAP specimens by using a Phillips XL30 microscope operated at 15 kV. Top views as well as cross sections were performed to observe morphology evolutions and estimate coating growth rates. These observations were not generalised in the case of TiN and TiO_2 samples although they were punctually used. In the case of HAP coatings, no conductive overcoating was deposited in order to enhance the efficiency of EDX microanalysis.

Characteristic X-rays are one of the most common ways of energy dispersion after excitation of a sample with electrons of energies around 10 KeV. This phenomenon is the basis of EDX. When an electron of the incident beam creates a hole in a core level of the atom (f.i. the 1s orbital with principal quantum number n=1), the vacancy is occupied by means of the de-excitation of an electron from an upper energy level (i.e. the lower binding energy level n=2), which will produce the emission of a photon with energies:

$$E_2 - E_1 = h.\nu = \frac{h.c}{\lambda} \qquad (14)$$

The distribution of the emitted X-rays gives place to a discrete characteristic spectrum. The principal X ray lines generated by the core electronic transitions give rise to characteristic transitions such as Kα, Kβ, Kγ/ Lα, Lβ, Lγ/ Mα, Mβ, where L, M, N... indicate the principal atomic number of the orbital where the ionisation was produced (n= 1, 2, 3...) and α, β, γ indicate the origin of the decayed electron (one level up to two, three...). Since the atomic orbitals present rupture of the degeneracy due to the electron angular momentum (determined by the quantum number l), the transitions are split into different lines ($K\alpha_1$, $K\alpha_2$).

The intensity of the characteristic lines is related to the concentration of the element itself and to the atomic number Z (determining the ionisation cross section of the atom and the probability of photon emission after ionisation). The absorption A and the fluorescence coefficient F are two more factors influencing this intensity. This parameters give raise to ZAF corrections that allow a semiquantitative analysis of the target sample. This analysis is always carried out after determination of the contribution from the different lines of the element.

We have applied this technique to the analysis of HAP coatings since it provides a semiquantitative estimation of the Ca/P molar ratio of the coatings. Hence, it was used for the characterisation of the different series of HAP coatings. EDX microanalysis was performed using the electron source of a Phillips XL30 microscope operated at 10 kV and an Oxford instruments X-ray detector. The data were analysed in the light element approximation for ZAF corrections.

2.5 OTHER CHARACTERISATION TECHNIQUES.

2.5.1 Ellipsometry.

The ellipsometry technique has been applied to study the thickness and refractive index of TiO_2 thin films. This optical technique is suitable for the analysis of dielectric

materials with polished surfaces. The change in polarisation of an incident laser beam can be studied as a function of the wavelength. For our purposes, this excludes the applicability to TiN (i.e. good electrical conductivity) and HAP (i.e. high surface roughness).

The thickness and refractive index values of transparent coatings grown on Si can be obtained in these conditions from the values of the phase ellipsometric parameter Δ, and the amplitude parameter ψ. These parameters determine the complex reflection ratio ρ, analysed in terms of a parallel and a perpendicular component to the surface. This complex reflection ratio is indicative of the changes in polarisation of the incident and reflected beams:

$$\rho = \frac{r_p}{r_s} = \tan\psi e^{i\Delta} \qquad r_p = \frac{E_{p,refl}}{E_{p,inc}} \qquad r_s = \frac{E_{s,refl}}{E_{s,inc}}$$

The thickness and refractive index of aerosol-gel derived TiO_2 coatings were measured by ellipsometry (Gaertner L116B) at a 632.8 nm wavelength and using a 70° beam incidence.

2.5.2 Ultra-microindentation.

This technique is a powerful tool that has already been used by several groups to establish the mechanical differences between bulk materials and their corresponding thin film structures. It has also proved to be useful to evidence different orientations of single-crystals and to measure the stresses in thin films grown by different techniques or over different substrates [MAN99]. In addition, it has been successfully applied to biological systems to characterise human cortical and trabecular lamellar bone [RHO97].

The Young´s modulus (E_m) and hardness (H) of the series of TiN and TiO_2 coatings have been determined by using this technique. In the present work, the

mechanical model described by Pharr & Oliver has been followed [OLIV92]. The basis of this method is the introduction of geometrical and experimental corrections to the analytic expression used for the calculation of the projected area of contact, which is obtained from the estimation of the depth of indentation. The details of this model are presented in annex II.

Indentation tests over TiO_2 samples were performed using a Shimadzu DUH-200 dynamic ultra microhardness tester with resolutions of 0.02 mN in load and 0.005 μm in depth. Six full loading-unloading tests (10 mN maximal load) were applied to each sample to obtain the plastic energy of deformation (PED). The behaviour of TiO_2 coatings under constant load was analysed by measuring the mean indentation creep (MIC). Each sample was probed 10 times at 30 mN during 60 s. For the hardness and Young's modulus calculation, maximal loads of 6, 10, 18 and 30 mN were applied. For a statistic purpose, the sample surface was probed at six different places with a Berkowich diamond tip indentor (trigonal pyramid, 115° apical angle). Five loading cycles were monitored, allowing a 50% unload after 1 s. The tip area had been previously calibrated using quartz and aluminium references.

For the characterisation of the TiN coatings, six full loading-unloading tests with a maximal load up to 20 mN were applied to each sample to obtain values of the plastic energy of deformation. The mean indentation creep was measured by applying a constant force of 30 mN during 60 s. For the calculation of the hardness and Young modulus, maximal loads of 6, 10, 15 and 20 mN were applied. The samples were probed at six different locations with the Berkowich diamond tip indentor. Five loading cycles were measured allowing a 40% unload after 1 s time.

In order to perform the adherence tests of HAP coatings deposited on TiAlV alloys, the samples were also loaded with the Berkovich indenter adapted to the same apparatus. Indentation techniques have been extensively used for testing the adherence of glass and ceramic materials [ROS84, LU00]. The system permits a continuous monitoring of the load and displacement of the probe, thus allowing the reliable detection of the failure point. 20 loading-unloading tests (30 mN maximal load, 0.3

mN/s, every 3 s) were applied to monitor the effects of the propagation of a critical crack on the adherence of HAP coatings. The failure load (L_f) and failure depth (d_f) were found to be the most relevant parameters to determine the adhesive strength from the estimation of the contact area.

C BIOLOGICAL CHARACTERISATION:

2.6 INTRODUCTION

The evaluation of aerosol-gel titania films biocompatibility has been carried out by using chondrocytes , cells involved in cartilage regeneration and bone formation/ regeneration. For our studies, a human chondrosarcome cell line (hCSRCs) was used. DC sputtered TiN and aerosol-gel derived HAP films were tested with human pluripotent mesenchymal stem cells (hMSCs), which were obtained from the bone marrow of adult individuals. The observation of the cells was carried out by an immunofluorescent staining technique.

2.7 PRINCIPLES OF IMMUNOFLUORESCENT STAINING.

The aim of this section is to describe the basis of the method used for the evaluation of the behaviour and proliferation of cells cultured onto biomaterial surfaces. This method allows an *in-situ* exploration of cells adhered onto biomaterial surfaces revealing information about the number of cells, cytoskeleton, morphology and amount of extracellular matrix. The process implies the induction of an immune reaction. This reaction has not only been applied to cell systems, but more generally, for the evaluation of protein adsorption on organic biomaterials [TJI00]. It is thus a powerful technique with an increasing range of applications.

The room temperature exposure of the seeded cells to a serum from transgenic mice is the first step of the process. These mice suffer from an auto-immune disease and present antibodies against nuclear and cytoskeleton proteins [OGU00] that recognise human homologous proteins. The antigen-antibody complexes can be explored by

incubating a secondary antibody, an antimouse in this specific case, labelled with a luminescent molecule. Thus, the sites of specific binding can be visualised by exciting the molecular dye at the correct wavelength with a fluorescence microscope. The luminescence principle of molecular dyes is similar to the ones of rare earths (Er, Tb, Y etc) or semiconductor quantum dots. That is, electronic transitions in a band structure. In this case, transitions belonging to the molecular level are responsible of the luminescence rather than atomic transitions (rare earths) or semiconductor band gap transitions.

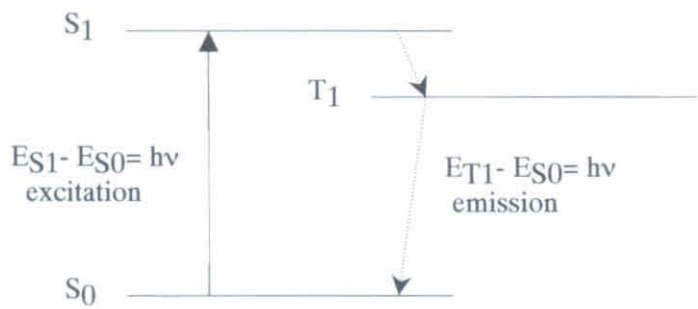

Figure II.7.1: General electronic energy levels corresponding to an organic dye. Excitation and radiative transitions.

Electronic energy level diagrams of molecular dyes consist of a singlet ground state S_0, a singlet excited state S_1 and an intermediate triplet T_1 of longer lifetime (figure II.7.1). Light absorption promotes electron excitation and therefore radiative transitions. Figure II.7.2 shows the excitation and emission scheme of the most common molecular dyes used in immunofluorescent assays. The combined use of green and red emitting dyes increases the number of applications allowing a reliable localisation of neighbour biomolecules with different functionalities. Concerning the fluorescence lifetime, absorption of high energy light (usually UV) induces a certain damage to the molecules so that, some bonds brake and consequently the corresponding molecule is no longer active. This mechanism explains the photodegradation of molecular dyes (exponential decay with time) [GAR97].

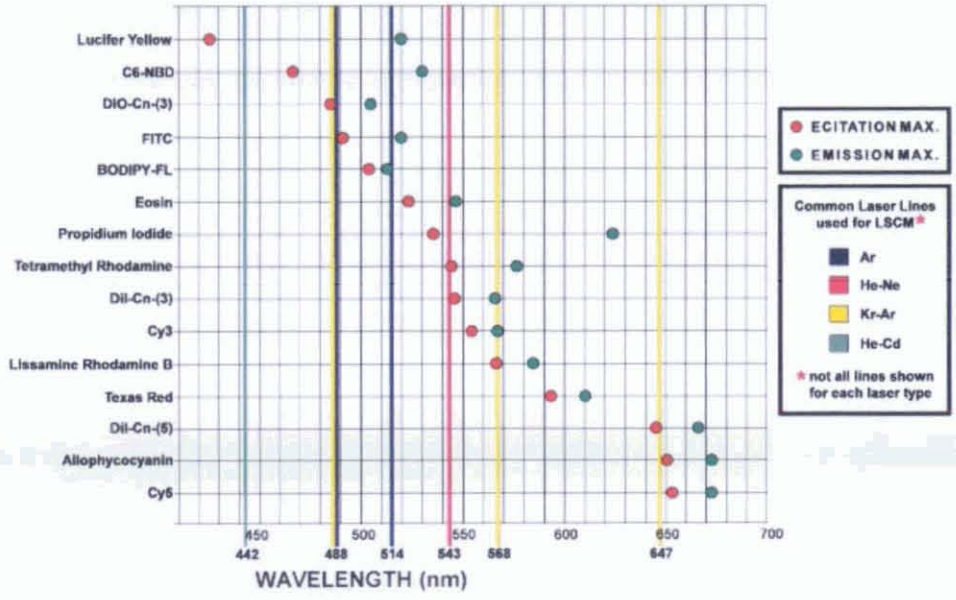

Figure II.7.2: Excitation and emission scheme of the molecular dyes used in immunofluorescent assays [GRA01].

2.8 DEVELOPMENT OF THE IMMUNOFLUORESCENT STAINING PROCESS.

2.8.1 Cell culture:

For the cellular assays, we have used a hCSRC line from ATT biosciences and hMSCs isolated from adult bone marrow following a previously described procedure [LEN96]. The cells were cultured in DMEM-low glucose supplemented with 10% Fetal Bovine Serum (FBS). After a week of culture they formed colonies. After three weeks, the cells were harvested by treatment with 0.05% trypsin/0.53 mM EDTA during 5 min and collected by centrifugation.

2.8.2 Cell seeding.

a) Seeding of: In order to test the biocompatibility of TiO_2 coatings in comparison with the bare surface of the well known TiAlV alloy, hCSRCs were seeded onto both materials. The experimental procedure followed for the cells observation on opaque substrates is described in figure II.8.1. Several plaques (1 cm^2) consisting of a

titania coating sintered at 500°C, as well as bare TiAlV substrates, were washed with phosphate buffer saline (PBS). After this, the plaques were placed individually on tissue culture dishes and sterilised in a culture cabin by 12h exposure to UV radiation. Approximately 200,000 cells were seeded on each surface and incubated during 48 hours at 37°C in an O_2/CO_2 (96/4 v/v) atmosphere. The cells were finally washed with PBS, fixed with methanol and kept in PBS at 4°C until observation.

b) Seeding of hMSCs: The adhesion of hMSCs on TiN and TiAlV surfaces was compared by seeding pluripotent hMSCs. The cells were cultured onto TiN and TiAlV surfaces as described previously for hCSRCs onto TiO_2 surfaces. The same experimental procedure applies for the seeding of these cells onto HAP surfaces.

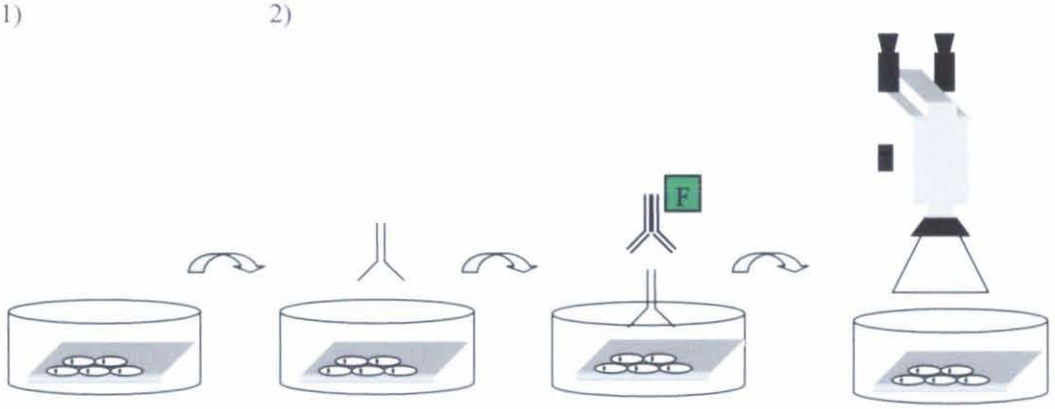

Figure II.8.1. Experimental procedure followed for the observation of the cell on opaque substrates. 1) Cell incubation. Fixation and albumin blockage. 2) Autoimmune serum incubation. 1 h. 3) Secondary antibody reaction. 30 min. 4) Observation. 495 nm.

2.8.3 Visualisation of cells over opaque surfaces:

The surfaces cultured with hCSRCs or hMSCs were blocked with 5 % milk protein in TBST (10 mM Tris-HCl pH 7.5, 150 mM NaCl and 0.05 Tween 20) during 2 hours. After repeated wash with 1 ml of 1% milk protein in TBST, we proceeded to the incubation at room temperature of 200 µl of serum from transgenic mice at 1/400 dilution in TBST for 2 h. The surfaces were washed for three times with 1% milk

protein in TBST and incubated in dark conditions for 30 min with a secondary antibody labelled with fluorescein (anti-mouse, Santa Cruz, Ca, at 1/4000 dilution). The surfaces were finally washed and the cells were visualised by illumination at 495 nm in a fluorescence microscope (Axiovert 35). Three different experiments were carried out with triplicate samples from TiO_2 and TiAlV for hCSRCs and TiN and TiAlV for hMSCs.

CHAPTER III: *TiO_2, AND TiN THIN FILMS*

CHAPTER III: *TIO_2 AND TiN THIN FILMS.*

3.1 INTRODUCTION.

In this chapter, we focus our attention on the chemical, structural, mechanical and biological characterisation of aerosol gel derived TiO_2 and magnetron sputtered TiN coatings. We emphasise our analysis in the description of those properties directly related with the application as passivating and insulting layers. These coatings are expected to provide a chemical stability to the underlying TiAlV alloy and to present a good mechanical response. However, in order to study the fundamental properties of the coatings, we have used Si(100) substrates of high resistivity (ρ> 20 MΩ.cm) thus minimising substrate influence in the FTIR transmission measurements. Concerning the nomenclature of the coatings, we have referred it to the sintering temperature, irrespective of the preparation method (conventional or RTP) so that, TiO150 refers to a TiO_2 coating sintered at 150ºC and a TiN500 refers to a TiN film annealed at 500ºC. To determine whether titanium based buffer coatings could present a suitable biocompatibility, we have observed the behaviour of different human cells seeded onto TiO_2 and TiN surfaces. Two experimental procedures were used to perform the biological characterisation. In the case of TiO_2 surfaces, human chondrosarchome cells (hCSRCs) were used. To perform the evaluation of TiN interlayers, human Mesenchymal Stem Cells (hMSCs) were seeded onto TiN surfaces. We emphasise that these latter tests are not only interesting from the point of view of biomaterial evaluation but also from the biological potential of these cells. As we have previously mentioned, hMSCs contribute to the regeneration processes of mesenchymal tissues including cartilage, bone, muscle, ligament, tendon and stroma [CAP91, BRU98].

3.2 AEROSOL-GEL DERIVED TiO_2.

3.2.1 FTIR.

The FTIR spectra corresponding to the TiO_2 coatings sintered at different temperatures are presented in figure III.2.1. Several bands associated with Ti-alkoxi

bonds [BUR99] are detected at 930, 1040, 1070, 1125 and 1375 cm^{-1} in the TiO150 coatings. These bands originate from remnant organic species not completely eliminated after the polycondensation process. Their intensity is drastically reduced or they even disappear after sintering at 300ºC. A relevant feature concerning the vibration bands of Ti-O and Ti-O-Ti bonds (800-400 cm^{-1}) is the band shift from 450 cm^{-1} for the TiO150 coating to 435 cm^{-1} for the coatings sintered at higher temperatures (inset of figure III.2.1). This evolution is related to structural and chemical changes in the environment of the titanium atoms, from the non hydrolysed alkoxide to the solid oxide obtained after hydrolysis/ polycondensation. Sintering at 500ºC causes a notable intensity increase of the Ti-O-Ti band, which is produced by the amorphous to crystalline transition (see XRD in next paragraph). An extra band appears at 1070 cm^{-1} in the spectrum of the TiO800 coating due to the increasing absorption of the SiO_2 film, which grows on the non coated backside of the substrate. The band at 1625 cm^{-1} associated with molecular water is also discerned with decreasing intensity for the samples prepared with increasing sintering temperature. The wide band observed at 3600-3100 cm^{-1} is assigned to hydroxyl groups, which are also gradually eliminated for increasing sintering temperatures

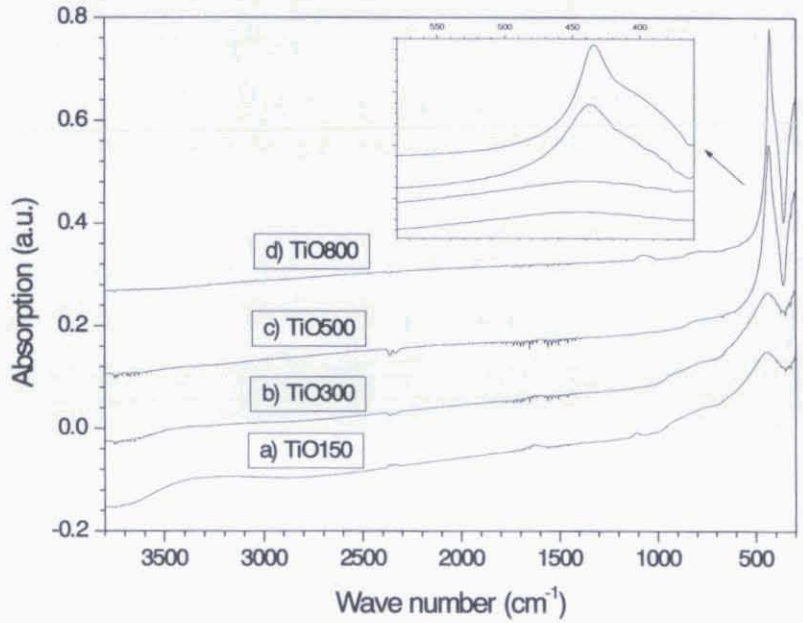

Figure III.2.1 FTIR spectra of aerosol-gel derived TiO_2 coatings obtained after sintering: a) TiO150, b) TiO300, c) TiO500, d) TiO800.

3.2. XRD.

The results from the characterisation of the TiO_2 coatings by XRD are depicted in figure III.2.2. The diffractograms corresponding to TiO150 and TiO300 samples (a and b, respectively) present no peaks arising from the coating, indicating that the thermal activation is not high enough to overcome the amorphous phase obtained after xerogel formation. Sintering at higher temperatures drastically activates the film crystallisation. Multiple peaks appear in the TiO500 and TiO800 XRD diagrams (figure III.2.2c and d), proving that a polycrystalline coating is formed. The position of the peaks is in agreement with the formation of a pure anatase phase corresponding to the Miller indexes inserted in figure III.2.2 (JCPDS 84-1286). The tetragonal lattice of the anatase phase is depicted in figure III.2.3 showing the two characteristic chemical units per unit cell. Two residual peaks from the Si substrate are also present in the diagrams. Sintering at 800ºC led to narrower and more intense peaks that prove an increase in the crystallite size of the titania coating. The relative intensities of the diffraction peaks are in agreement with those obtained from anatase standards, showing that the substrate induces no preferential growth directions in the films.

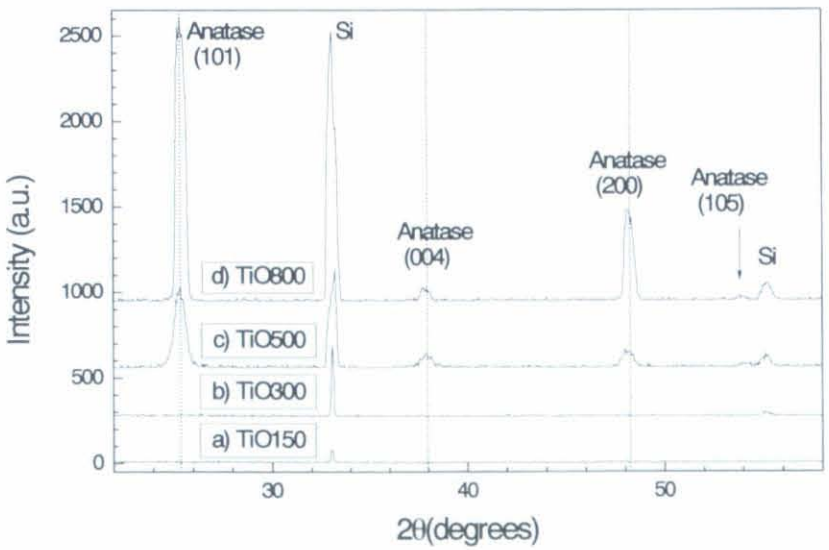

Figure III.2.2 XRD diffractograms of aerosol-gel derived TiO_2 coatings obtained after sintering: a) TiO150, b) TiO300, c) TiO500, d) TiO800.

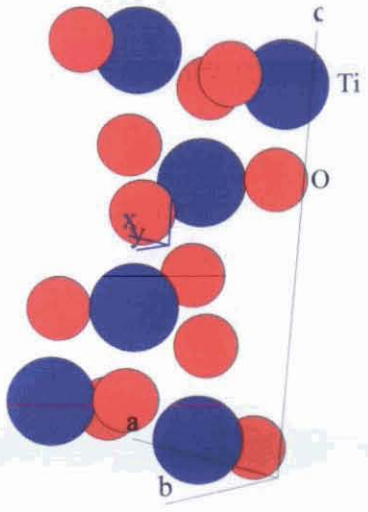

Figure III.2.3 Tetragonal TiO_2 anatase cell.

3.2.3 Ellipsometry.

Ellipsometry measurements performed on TiO_2 films fired at 500°C showed that the thickness of a single layer was about 0.1 μm and that the film thickness increased linearly with the number of deposition/ heat-treatment cycles. The thickness of the final coating after 10 cycles was thus estimated to be around 1 μm. Such a thickness was necessary to perform nanoindentation measurements reasonably insensitive to the substrate response. The surface homogeneity was proved by the low dispersion (+/- 0.5%) in the values of the refractive index measured throughout the film surface. For films fired at 500°C, the averaged value of the refractive index was 2.22. Ellipsometry measurements carried out on the rest of the coatings showed an increase of the refractive index for an increasing annealing temperature. Values of 1.93 and 2.34 where obtained for TiO150 and TiO800 coatings, respectively. The refractive index increase with raising temperature reflects a thermally activated densification mechanism as previously reported for aerosol-gel TiO_2 coatings [BUR99].

3.2.4 SEM.

The main objective of this SEM study was to confirm that it is possible to deposit optical quality TiO_2 thin films by the aerosol-gel process. Figure III.2.4a shows

a cross section image of a TiO150 sample observed after five multilayer depositions. No relevant surface feature is observed in the μm scale. Only slight wavy features with smooth topographic changes can be detected below that scale.

The activation at higher temperatures provides a more pronounced densification process leading to TiO300, TiO500 and TiO800 coatings with reduced roughness. The densification process is carried out at a rate slow enough to produce no crack in the coatings (i.e. due to tensile or compressive stresses) even at the highest sintering temperatures (figure III.2.4b).

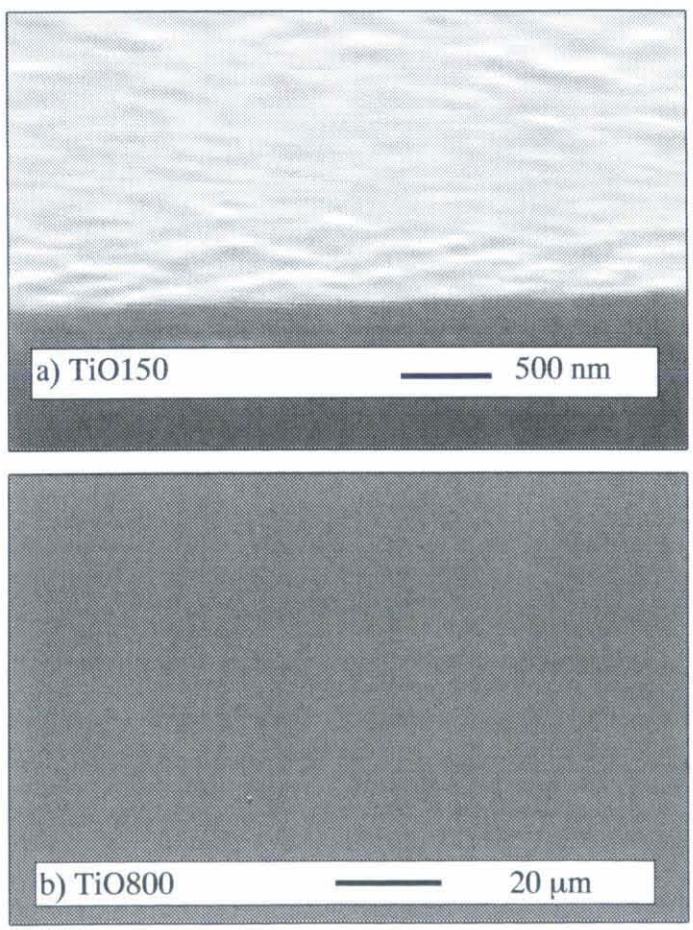

Figure III.2.4 SEM images of: a) a cross section view of a TiO150 coating showing several topographic features. b) Top view image of the morphology of a TiO800 coating.

3.2.5 Ultramicroindentation.

The ultramicroindentation technique has allowed to derive several mechanical parameters that establish a range of mechanical responses for the aerosol-gel TiO_2 coatings. Typical 10 mN loading-unloading versus displacement curves are presented in figure III.2.5 for the different coatings. All the mechanical parameters are derived from the differences existing between these curves after an averaging process. At first sight, it can be observed that the mechanical response depends on the annealing treatment applied to the coating.

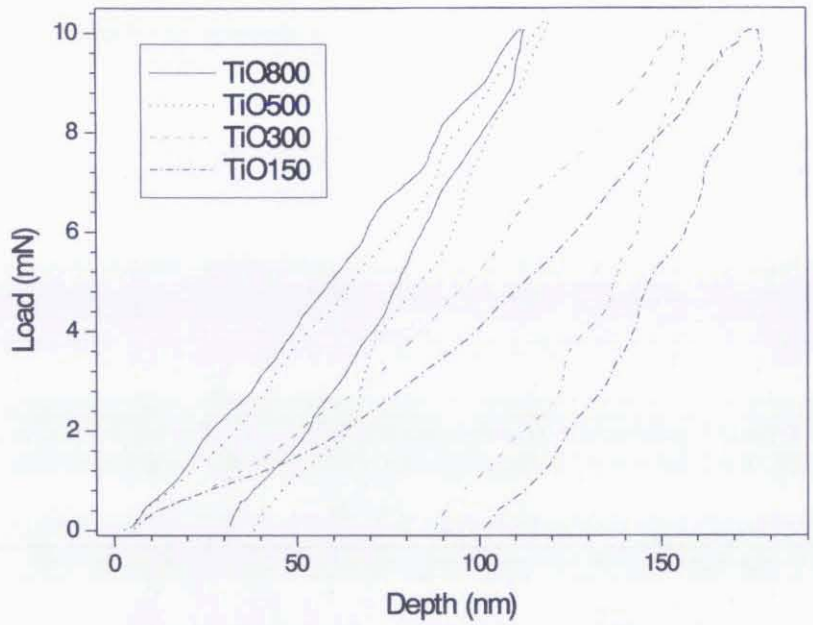

Figure III.2.5 Loading-unloading ultramicroindentation curves for the titania coatings (10 mN maximal load): a) TiO150, b) TiO300, c) TiO500, d) TiO800.

The subtraction of the area enclosed by the unloading curve from that defined by the loading curve determines that coatings sintered at 150 and 300ºC suffered from considerably higher plastic deformation than coatings sintered at 500 and 800ºC (figure III.2.6, left axis). This difference is linked to the structural evolutions depicted by FTIR, XRD and ellipsometry. The mean indentation creep (MIC) measured at 30 mN (figure II.2.6, right axis) are also correlated with the structural evolution of the coatings. Polycrystalline TiO500 and TiO800 coatings present much lower deformations in

comparison to the TiO150 and TiO300 coatings. The mechanical differences are also evidenced by the values of maximal indentation depth and by the unloading slope.

The maximal indentation depth of the different TiO_2 coatings, obtained from the root mean square of 6 measurements after five loading-unloading cycles, are presented in figure III.2.7 versus the maximal indentation load. It is clearly observed that the coatings sintered at lower temperatures generate a weaker opposite force to the loads and suffer from deeper indentations.

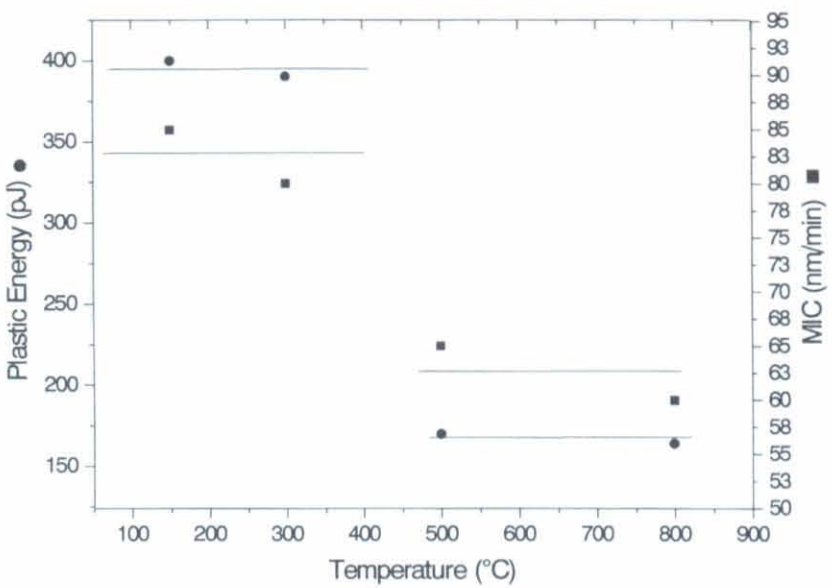

Figure III.2.6 Values of the plastic energy of deformation (PED, ● left axis) and mean indentation creep (MIC, ■ right axis) versus the sintering temperature applied to the titania coating.

In figure III.2.7, two groups of samples can be distinguished in terms of resistance to the indentation load (TiO150 and TiO300 vs the stiffer TiO500 and TiO800). These results are again correlated with XRD, FTIR and ellipsometry data. However, both groups could no longer be distinguished for the highest load (all the samples are almost equally spaced in depth for loads of 30 nm), presumably due to an increasing influence of the probe on the sample.

The values of hardness (H) are presented in table III.2.1 with the references of the load and the maximal depth reached for every coating. The Young's moduli (E_m) were 142± 7, 150± 9, 170± 20, 190± 20 GPa for coatings sintered at 150, 300, 500 and 800°C, respectively. Both H and E_m values confirm that a clear correlation exist between sintering temperature and the mechanical properties.

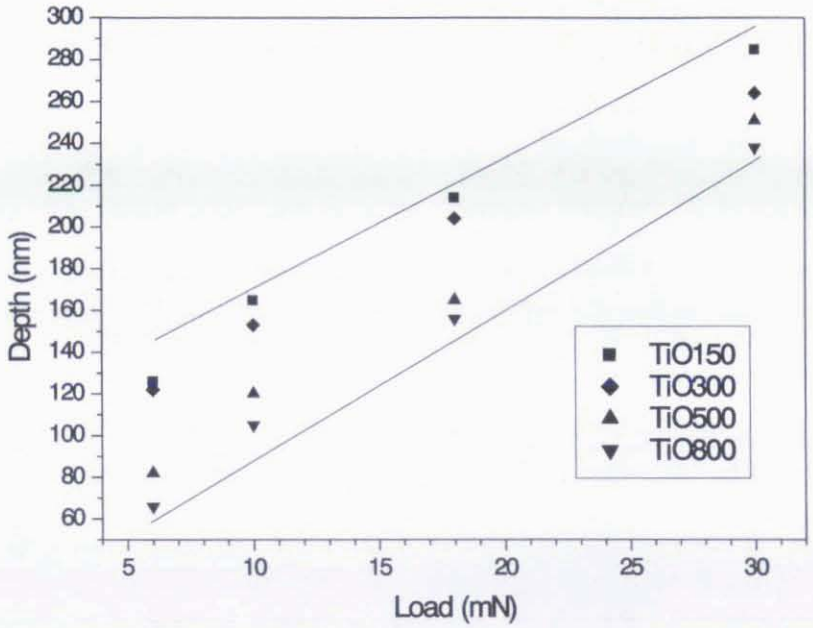

Figure III.2.7. Plot of the maximal depth versus maximal load for TiO150 ■, TiO300 ◆, TiO500 ▲ and TiO800 ▼ coatings.

	TiO150		**TiO300**		**TiO500**		**TiO800**	
L (mN)	hmax(nm)	H (GPa)	hmax (nm)	H (GPa)	hmax (nm)	H (GPa)	hmax (nm)	H (GPa)
6	125	9	120	9	80	16	65	18
10	155	11	155	12	120	19	105	19
18	200	15	195	18	165	19	160	20
30	285	16	265	18	250	19	240	20

Table III.2.1: Hardness values (H, ± 1 GPa) and maximal depth (hmax, ± 5 nm) vs load (L) for the different TiO_2 coatings.

Thus, the overall results confirmed that the condensation, crystallisation and densification degrees of the coatings, reached after sintering at 500°C, drastically influence the film mechanical behaviour.

6.1.2 Chondrosarcome cells onto TiO_2.

The aim of this section is to demonstrate the good biological behaviour of the previously described TiO_2 films. We have compared the adhesion of hCSRCs with the behaviour corresponding to standard Ti6Al4V surfaces. The adherence and growth of hCSRC was studied on a coating sintered at 500°C (TiO500). As detailed in Chapter II, the immuno assay performed to visualise adhered cells on opaque surfaces was achieved through a two step process. In the first immune reaction, nuclear and cytoskeleton proteins were recognised by an auto-immune serum from mouse. Secondly, the immune complexes formed were reacted with an anti-mouse antibody labelled with fluorescein, which excites the fluorescence reactions in cell nuclei and cytoskeleton (figure III.2.8).

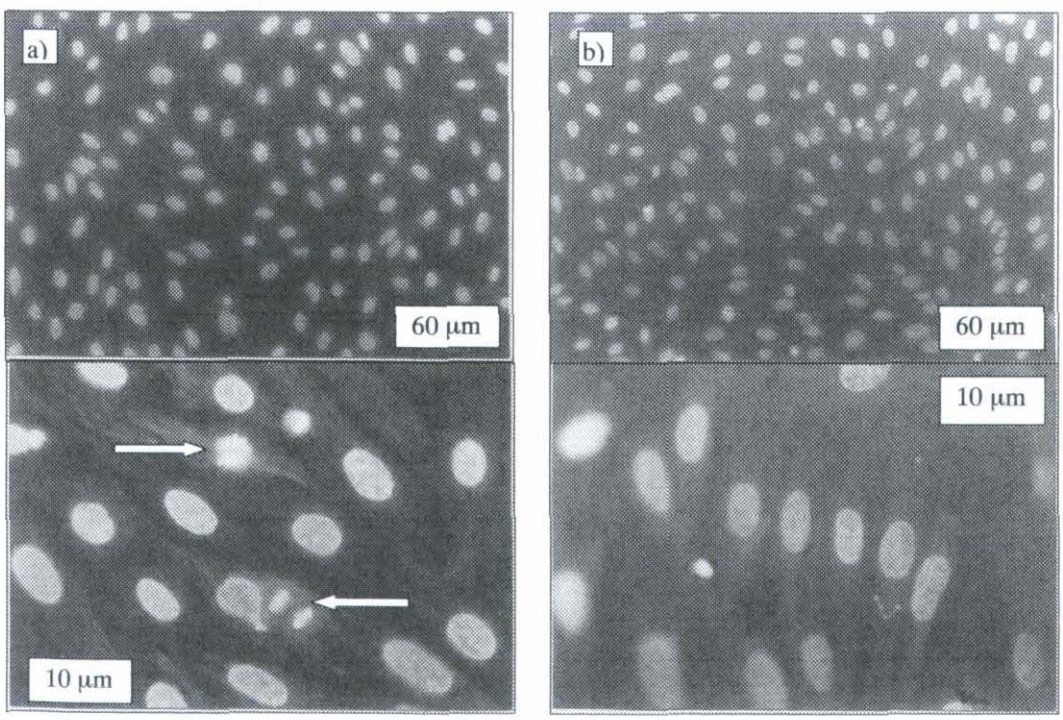

Figure III.2.8: Fluorescence micrograph showing at different magnifications the behaviour of hCSRCs seeded on a) TiO500 and b) TiAlV alloy.

It was established that 80% of seeded cells were adhered to both TiO500 and TiAlV surfaces. However, some differences were observed. For the titania surface (figure III.2.8a), the distance between cells was larger than that observed for the bare TiAlV surface (figure III.2.8b). This can be due to an increase in extracellular matrix components of cells adhered to titania. At higher magnification, the cytoskeleton of cells on titania showed a polygonal array, while cells on TiAlV presented a more parallel appearance. In addition, cells on titania surfaces showed proliferation signals since several stages of the cellular cycle could be observed. The arrows in figure III.2.8 show these evolving nuclei, which were not observed on TiAlV substrates. Thus, it can be concluded that aerosol-gel deposited titania coatings show improved biocompatible properties while compared to a TiAlV surface.

3.2.7 Summary and conclusions.

The structure of titania coatings deposited by the aerosol-gel process has been found to closely depend on the applied sintering temperature. FTIR and XRD analysis help to understand the sequence of processes taking place during sintering. It was shown that an important activation of the Ti-O-Ti network condensation and crystallisation is produced when a temperature of 500ºC is reached. Ellipsometric measurements of the refractive index show that the processes are accompanied by a significant film densification. SEM images confirm the homogeneity of the coatings in the μm scale. Concerning the morphology of similar coatings in the nm scale, the morphology of aerosol-gel TiO_2 coatings condensed at low temperatures has been previously studied by AFM [VII00, LAN01]. Surface roughness inferior to 5 nm were measured over scanned areas of 2x2 μm.

Indentation tests showed that physicochemical differences between the samples can be correlated with a characteristic mechanical behaviour. It was stated that the coatings can be classified into two groups. Coatings sintered at 500ºC or higher temperatures present lower MIC and show better performances in terms of lower plastic deformations. This behaviour can be related with the main mechanism governing the

indentation process, which is characterised by the plastic deformation suffered for a fixed applied load. Coatings sintered at 150 and 300ºC suffer a dominant cutting mechanism (higher plastic deformations), while coatings sintered at 500 and 800ºC undergo a compressive strain mechanism (lower plastic deformations) [SAM86]. FTIR, ellipsometry and XRD measurements show that this feature is closely related to the Ti-O-Ti network polycondensation, densification and crystallisation. Coatings sintered at higher temperatures are also harder and present higher Young's moduli. It must be stated at this point that, taking into account the properties of the TiO150 and TiO300 samples, these coatings are more prone to suffer from substrate influence during indentation. Furthermore, these coatings suffer from higher plastic deformations, so that the force applied during the measurement could act at the same time as a driving force for the condensation and strengthening of the coating. These two factors may explain the relatively high values of E_m obtained for the not completely densified TiO150 and TiO300 films.

Cellular adhesion tests proved that TiO_2 coatings prepared in this work are biocompatible materials. In particular, TiO_2 surfaces were demonstrated to show improved surface properties with respect to a standard TiAlV alloy, since a considerably higher number of hCSRCs was observed to adhere and develop on those surfaces. Not only the adherence, but also the growth of the cells, prove the high potential of aerosol-gel titania coatings for being safely used in prosthetic applications.

A comparison of these coatings with other titania films produced by alternative methods reveal interesting features. The hardness and Young's modulus of ion bombarded spin-coated films measured by ultra-microindentation are considerably lower than the values obtained for any of our coatings [JAM98]. The results for arc deposited titania coatings are nearer to the values obtained in our study [BEN00]. When amorphous arc coatings are produced, the Young's modulus (140 GPa) is quite close to the value of our TiO150 coatings (142 GPa). When rutile crystalline coatings are produced, the Young's modulus (180 GPa) shows a good level of coincidence with the value of our TiO800 coating (190 GPa). However, it should be mentioned that the hardness values of aerosol-gel titania coatings are higher than those obtained for the arc

deposited TiO_2 coatings. In any case, our hardness values appeared systematically lower than the values measured for rf sputtered titania films (23 GPa) [BAL98].

Comparing titania coatings prepared by the aforementioned techniques, it is worth mentioning that the aerosol-gel titania coatings introduce a noticeable advantage from the point of view of their mechanical properties. Depending on the sintering temperature, they present a range of mechanical properties that makes it possible to tailor their response under stress. Consequently, a multilayer deposition procedure with various sintering temperatures can produce coatings with gradual mechanical properties. This configuration is considered of primary interest for prosthetic applications since it has been shown that the drastic differences in Young's modulus between bone (30 GPa) and the prostheses alloy (up to 200 GPa) can produce severe damage. This effect is dramatic in the case of femur heads sustaining hip-joint prostheses [LON98].

3.3 TiN COATINGS PREPARED BY PLASMA SPUTTERING.

3.3.1 Physicochemical characterisation.

The XRD diagrams corresponding to as-deposited TiN (TiN-AS) and annealed films (TiN-300, TiN-400, TiN-600) showed, as can be observed in figure III.3.1, the presence of a weak (111) TiN cubic phase peak with almost non detectable (200) peaks. This effect is a consequence of the preferential growth of the coatings in the (111) direction, as deduced from the comparison with reported intensity charts (PDF 38-1420). The unit cell of TiN is depicted in figure II.3.2. The characteristic AB planar conformation of Ti and N atoms along (111) direction is observed, explaining the intrinsic tendency to grow in that direction. The annealing treatments at 300 and 400°C produced only a slight increase of the (002) peak but did not produce a critical enhancement of the film crystallinity. Sintering at 600 °C activated a slight densification process as derived from the change of intensity of the (100) peak at $2\theta = 36.65$.

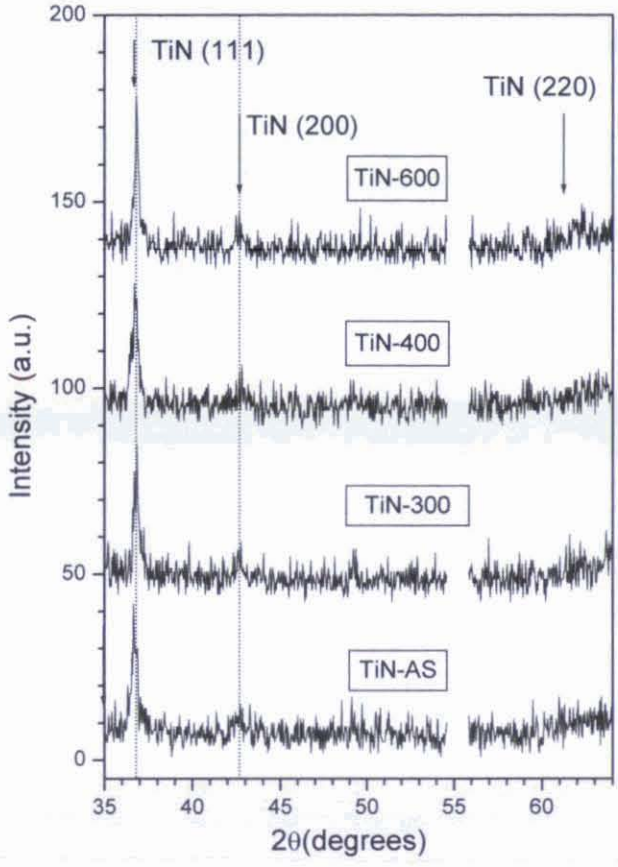

Figure III.3.1. XRD diagrams from TiN-AS, TiN-300, TiN-400 and TiN-600 coatings.

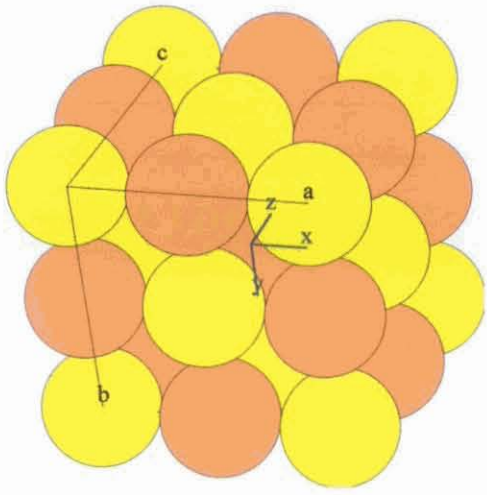

Figure III.3.2. Cubic unit cell corresponding to TiN.

3.3.2 Morphology of TiN coatings.

SEM micrographs of the TiN films show extremely homogeneous coatings as depicted in figure III.3.3. The top view image (a), which was focused with the reference of an induced surface mark, shows the absence of relevant surface roughness at the micron scale. This fact was also confirmed for the coatings sintered at higher temperatures. The cross section image shown in the inset (b) was obtained from backscattered electrons, which are sensible to the species present in a compound although the images present lower spatial resolution. This image confirmed that the final thickness of the coating is of the order of 1 μm, in agreement with the estimations obtained from the sputtering growth rate.

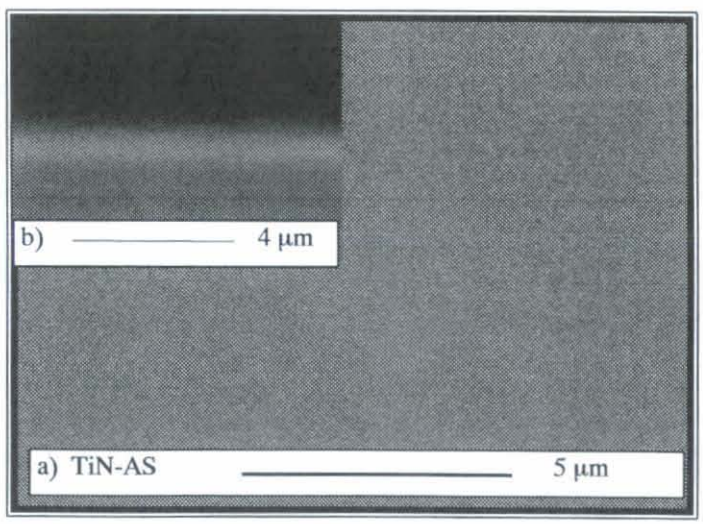

Figure III.3.3: SEM images from the TiN-AS sample. a) Top view. b) Cross sectional view in the backscattered electron mode.

3.3.3 Mechanical properties.

Typical 20 mN loading-unloading versus displacement curves for the different coatings are presented in figure III.3.4. It is observed that all the coatings present very similar mechanical behaviours. The values of the plastic energy of deformation are

presented in the second column of table III.3.1 and can serve to establish the slight mechanical differences existing between the samples. The error on the PED values was determined from the standard deviations after 6 measurements on each sample rather than derived from the apparatus precision. These values show that annealed coatings exhibit a slightly lower plastic deformation (760 pJ) than the TiN-AS coatings (1000 pJ). The mechanical similarities are also evidenced from the closeness of the values of maximal indentation depth and unloading slope. The annealed TiN-600 coatings are somewhat stiffer since they present smaller maximal depths and higher unloading slopes than the other coatings, as discerned from the loading-unloading charts of figure III.3.4.

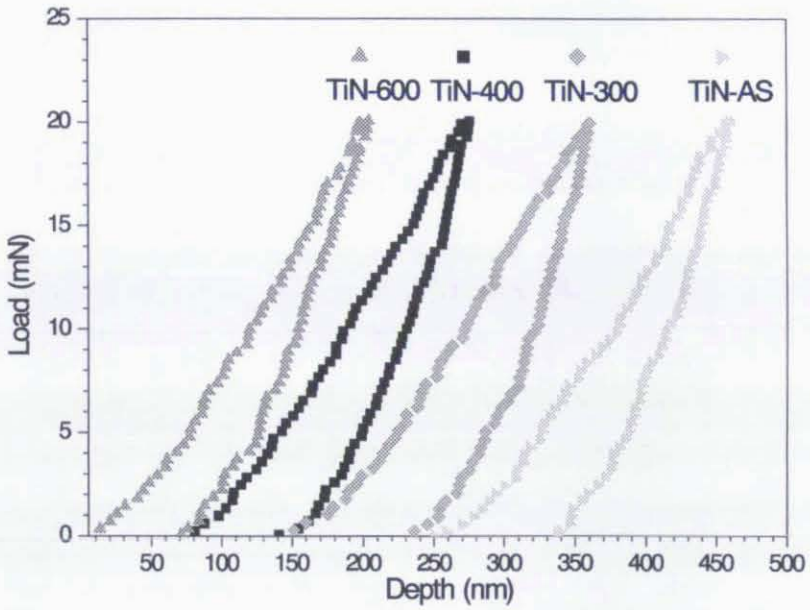

Figure III.3.4: Full loading-unloading versus depth curves of TiN coatings (maximal loads of 20 mN).

The deformation of the TiN coatings under constant loads, estimated by measuring the MIC, further confirmed the uniformity of the mechanical response of the TiN coatings. The values obtained for the different TiN coatings after the statistical analysis of 10 measurements are presented in the third column of table III.3.1. Figure III.3.5 shows the evolution of the indentation at constant load (30 mN) on a TiN-AS

coating. It is clearly seen that, except for the very first seconds, the coating deformation can be considered as a single linear curve.

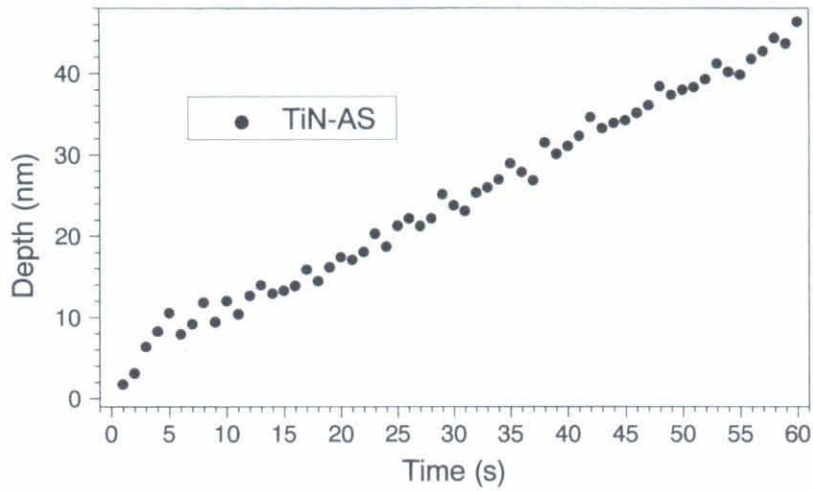

Figure III.3.5 Measurement of the indentation creep for a TiN-AS coating. A constant load of 30 mN was applied during 60s.

Sample	PED (pJ)	MIC (nm/min)	H (GPa)	E_m (GPa)
TiN-AS	1000± 40	45±5	18.8± 0.7	286± 8
TiN-300	920± 40	45±5	18.9± 0.8	299± 8
TiN-400	890± 40	50±5	19.2± 0.9	300± 20
TiN-600	760± 40	45±5	19.5± 0.9	310± 20

Table III.3.1: Values of the plastic energy of deformation (PED), hardness (H), mean indentation creep (MIC) and Young's modulus (E_m) obtained form the TiN coatings.

The mechanical similarity between the coatings is confirmed by the calculation of the values of H and E_m, which are listed in table III.3.1. The values of H were observed to be only slightly dependent on indentation depth reaching a maximum value for maximal loads of 20 mN (fourth column, table III.3.1). The E_m values are independent of the indentation load as derived from the model of Oliver & Pharr [OLI92]. Finally, it can be observed that, taking into account the error bars, the slightly

increase of both H and E_m for increasing annealing temperature (from 18.8 to 19.5 GPa and from 286 to 310 GPa for H and E_m, respectively) cannot be considered as a factual tendency.

3.3.4 Mesenchymal cells onto TiN.

TiN surfaces have been tested with hMSCs and compared with the standard TiAlV alloy. The biological behaviour of TiN was tested on as-sputtered (AS) coatings. In order to overcome the material opacity and to be able to visualise the cells on material surfaces, we have used the immune technique introduced in chapter II. The results summarised in figure III.3.6 show that the fluorescent activity was concentrated over the cell nuclei, allowing no reliable observation of the cell cytoskeleton.

Concerning the adhesion of the cells, it can be observed that hMSCs adhere on both TiN and TiAlV material surfaces (figures III.3.6a and b). However, if we consider the coverage rates, we observe a great discrepancy in the behaviour of cells deposited on TiN and TiAlV. It was established that almost 90% of the cultured cells adhere onto TiN, compared to less than 40% for hMSCs onto TiAlV.

Paying attention to the cell morphology, the appearance of the nuclei observed in figure III.3.6 was consistent with normal hMSCs in culture presenting no apoptotic sign. The nuclei of the hMSCs form isolated groups on TiAlV surfaces (figure III.3.6b), which can be attributed to an initial stadium of cellular growth. The cells on the TiN surface have overcome that stadium and present a tendency to be homogeneously distributed on the surface. Furthermore, several nuclei can be observed forming pairs (see arrows on the high magnification micrograph in figure III.3.6c). This is interpreted as a proof of the hMSCs activity while adhered on TiN. These results support the notion of improved biocompatible properties of reactively sputtered TiN in comparison with the TiAlV surface.

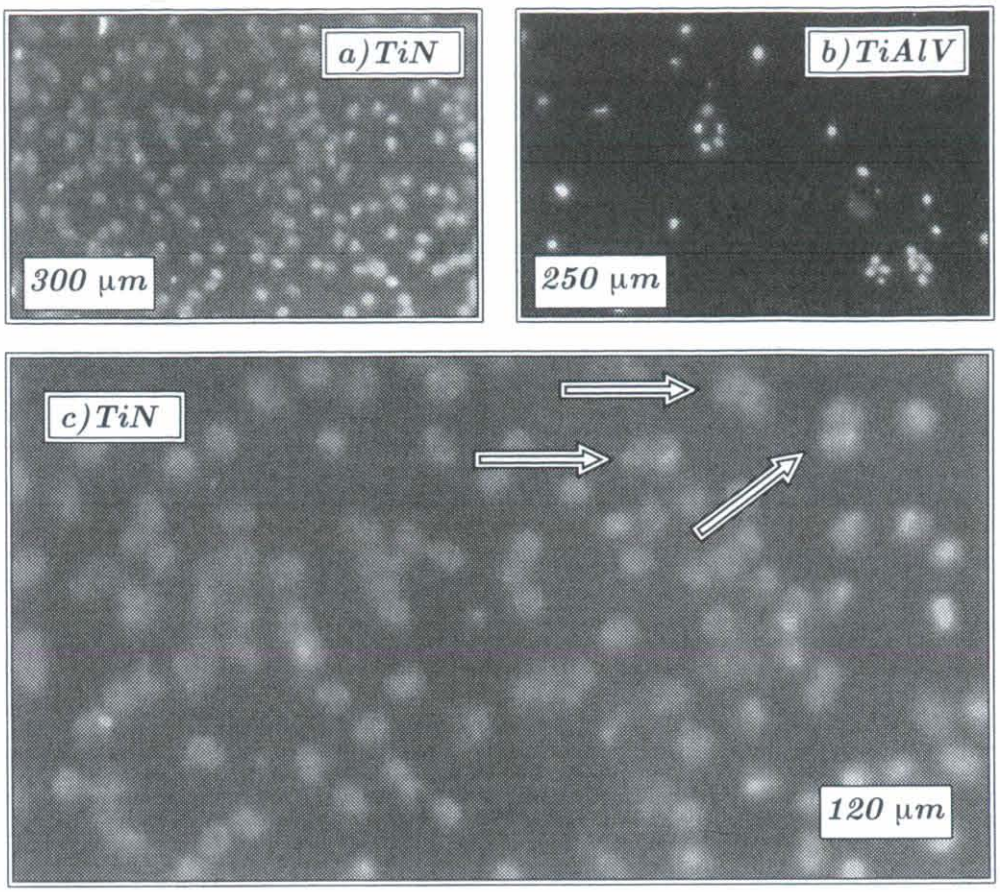

Figure III.3.6: Fluorescence micrographs showing the evolution of the nuclei from hMSCs seeded on a) TiN-AS, b) TiAlV alloy and c) TiN-AS with a higher magnification.

3.3.5. Summary and conclusions.

The TiN coatings formed by DC magnetron sputtering have been found to present very stable structures and morphologies, even after annealing at 300, 400 and 600°C, as derived from XRD and SEM results. For all the TiN coatings, the low substrate temperature involved during processing induced a preferential growth of the coating along the (111) direction [CHU99]. Only a slight densification process, could be observed on the TiN600 sample. This densification process has been previously observed with a transition temperature around 450°C on sputtered TiN thin films [PAR95]. Indentation tests have shown that the structural similarity existing between

the as prepared and annealed TiN coatings correlates with a very similar mechanical behaviour. The values of H and E_m remain constant within the experimental error although it has been established that coatings sintered at 600ºC suffer from lower plastic deformations. In other words, TiN coatings sintered at 600ºC present a more pronounced elastic indentation mechanism [SAM86].

The comparison of the mechanical properties of these coatings with those from other TiN films produced by alternative methods reveals the high performance of our coatings. Compared to the results obtained in the present work, TiN thin films prepared by the dynamic ion mixing technique [HAY99] and measured by nanoindentation gave very low values of both H and E_m (H= 4 GPa and E_m= 200 GPa). The results for planar magnetron sputtered coatings with different crystalline orientations are closer to the values obtained in our study [LJU96]. The H values of such coatings (20 GPa) are quite close to the values of our TiN coatings although a relevant difference was found with respect to E_m values (450 GPa). In general, it has been concluded from flexural resonant frequency studies that the maximal values of E_m for TiN_x coatings is obtained for x= 1 and reaches values up to 640 GPa [TOR87]. Although our weaker E_m values may indicate some deficiency in N content in our coatings, we consider that the huge differences obtained in the cited values could be partially explained by the differences between the measurement techniques.

The biological tests performed with hMSCs proved that TiN thin films prepared in this work are biocompatible. TiN surfaces showed a remarkably higher number of adhered hMSCs when compared with a standard TiAlV alloy.

The combination of the electrical, mechanical and biological properties of TiN coatings is considered of primary interest for prosthetic applications. In particular, the high level of hMSCs adhesion could be beneficially associated with the good conductivity of TiN substrates in order to *in-situ* stimulate the cells by electric pulses, which might help to determine their differentiation. Such a cellular treatment would considerably enhance the bone-prosthesis osteointegration at the early stages of implantation.

CHAPTER IV: *AEROSOL-GEL DERIVED HAP COATINGS.*

CHAPTER IV: *AEROSOL-GEL DERIVED HAP COATINGS*

4.1 PREPARATION OF HAP SOLUTIONS FROM ESTER AND ACIDIC PHOSPHATE PRECURSORS.

In this chapter, we aim to describe in detail the processes that lead to the formation of HAP coatings by the aerosol-gel technique. This ceramic outlayer should act as a bioactive ceramic in contact with bone tissue, allowing a rapid integration of the coated prostheses. We have used two different kinds of phosphate precursors. In the case of ester sols, we will focus on Ca-P stoichiometric variations. These more general calcium phosphate coatings will be referred as CP (calcium phosphate) samples in subsections labelled with A. In the case of coatings produced from phosphoric acid sols, we will only present results for the solution composition (Ca/P mr of 10/7) that leads to stoichiometric HAP coatings, so that the coatings will be referred as HAP in subsections labelled with B.

4.2 SOL PARAMETERS AND THERMAL STABILISATION.

As we have already argued in the experimental part, a lot of experimental efforts have been made for the determination of the aerosol-gel deposition parameters that allow the processing of high quality HAP coatings. We have included these results since they lead to relevant aspects for the subsequent discussion of the deposition process.

A) Phosphate Ester based sols (TEP).

In a first run of experiments, after the aerosol deposition and liquid film settlement, the precursor films were allowed to dry at room temperature. However, the films experienced a dramatic radial shrinkage, and substrate dewetting effects were observed due to the poor sol-gel reactivity of the TEP precursors. It was found that a thermal treatment at 500ºC, performed immediately after liquid film formation, helped to retain phosphate groups in the form of stable phases, which will be later described. In that case, no significant radial shrinkage was observed. However, EDX analysis showed

that a partial evaporation of the phosphate precursor is unavoidable, as the coatings presented always a lower phosphate content than expected from the Ca/P mr of the solution (see following sections). Stabilisation treatments at 150 or 300°C were found to accelerate P evaporation rather than inducing a liquid to solid transformation. An extensive characterisation of the coatings issued from different Ca/P mr solutions and stabilised at 500°C was thus performed in relation to these general features.

Addition of water and HCl or NH_3 to the solutions with Ca/P mr= 1.67 was studied in order to test to which extent the reactivity of the TEP precursors to the hydrolysis/ polycondensation mechanisms could be catalysed by acidic or basic conditions. As shown in the FTIR spectra presented in figure IV.2.1, a pH variation in the range 1 to 10 did not produce appreciable differences in the coating composition. EDX showed also that no improvement could be obtained in terms of phosphorus deficit. These features confirm that no or insufficient sol-gel transformation is involved in the formation of CaP coatings from calcium nitrate and TEP precursors. Finally, the addition of water to the solution, expected to activate the hydrolysis reaction and subsequent gel formation, led to a poor substrate wetting behaviour of the liquid film.

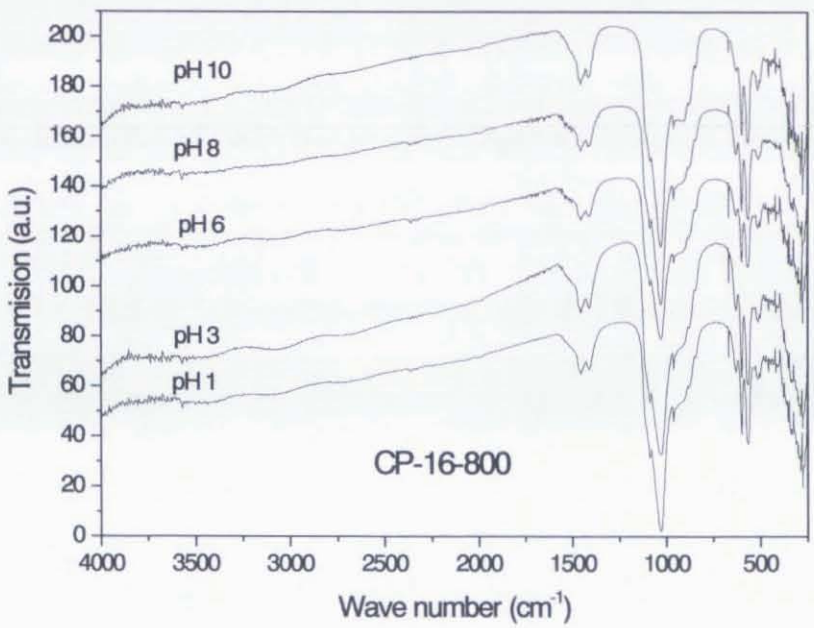

Figure IV.2.1: FTIR spectra of coatings formed from solutions with Ca/P=1.67 and pH ranging from 1 to 10. The coatings were sintered at 800°C.

Consequently, we will only describe in this paper the properties of films deposited from solutions prepared without water, HCl or NH_3.

B) Phosphoric Acid based sols (PhAc).

The preparation of HAP sols from PhAc involved a two step process and the independent storage, after ultrasonic slurring and filtering, of the precipitate and final sol. A detailed analysis (XRD, SEM and EDX techniques) of as-precipitated and sintered powders was carried out by varying the Ca/P mr of the precursor mixture. This procedure allows a control of the properties of the final precursor (leading to HAP). Several pH values were assayed by adding ammonia into the final precursor. The effects of the pH and the stabilisation temperature on the composition of the coatings were studied by FTIR.

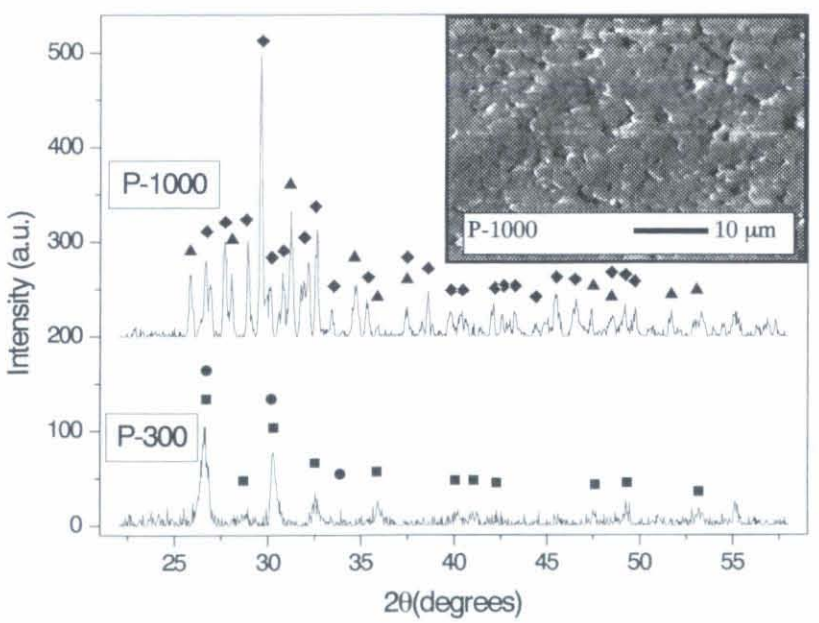

Figure IV.2.2 a) XRD diagrams of the precipitated particles sintered at: bottom 300°C, and top 1000°C. Identified phases are ●: $Ca_3(CO_3)_2(OH)_2$, ■: $CaPO_3OH$, Monetite, ♦: $Ca_2P_2O_7$, ▲: $Ca_3(PO_4)_2$, Whithlokite. b) SEM image from particles sintered at 1000°C.

XRD diagrams presented in figure IV.2.2a show the changes of the powder structure for two different sintering temperatures. The phases identified in the XRD diagrams of the particles sintered at 300ºC (figure IV.2.2a, bottom), were mainly Ca_3PO_4OH (Monetite, PDF 9-0080) and $Ca_3(CO_3)(OH)_2$ (PDF 23-0106) with a substoichiometric Ca/P mr with respect to HAP. Note that the peaks at $2\theta = 26.5^o$ and $2\theta = 30.5^o$ arise from a combined contribution of these compounds. The high temperature stabilisation of the particles at 1000ºC (figure IV.2.2a, top) produced a segregation into the solid solution of $Ca_2P_2O_7$ (PDF 33-0297) and $Ca_3(PO_4)_2$ (Whithlokite, PDF 9-0169). In this compound, we cannot discard the partial carbonate substitution in PO_4 sites. Furthermore, slight deviations from reported lattice parameters in Whithlockite support this incorporation [ELL94]. These phases were consistently observed in particles from solutions prepared with Ca(1M)/P(1M) volume ratios between 10/5 and 10/7. As depicted in figure IV.2.2b, the particles present a spherical-like shape and homogeneous particle size (1.5 μm). EDX measurements were performed on these samples after sintering between 300ºC and 1000ºC. The estimations of the Ca/P mr confirmed that the particles are calcium substoichiometric with respect to a HAP standard. A Ca/P mr close to 1.10 was found for both sintering temperatures.

These results have direct implications in the solution preparation. Since mixed suspensions with an initial Ca/P mr 1.67 lead to a Ca deficient precipitate, the filtered liquid solution should exhibit a Ca/P mr greater than the HAP stoichiometric value. According to this fact, the solutions were prepared by mixing 1M Ca and PO_4 solutions with a volume ratio of 10/7. A slight increase in PO_4 concentration, combined with a slight diminution of Ca concentration, was expected to produce a re-equilibration of the Ca/P mr in the filtered solution leading to a value nearer to 1.67.

Studies concerning the effects of the precursor solution pH on the composition of the films were performed by FTIR. The spectra presented in figure IV.2.3 prove that the solution pH drastically influences the coating formation. At this point it is interesting to introduce that structural hydroxyl groups in the HAP structure generate bands at 3570 (pure stretching band), 630 (librational mode) and 335 cm^{-1} (this last one, produced by Ca-OH stretching, is sometimes observed as a shoulder). Bands located in

the range 1030-1090 cm^{-1} are due to asymmetric phosphate stretching bands and those at 960, 605, 570 and 470 cm^{-1} are coincident with symmetric stretching and bending absorptions from the same group in HAP. Bands corresponding to Ca-PO_4 lattice modes are identified at lower wave numbers (295, 275 cm^{-1}). Thus, it was derived from the intensity of the bands at 630 and 3570 cm^{-1} that OH ion incorporation is deeply inhibited for increasing pH. No structural OH content could be identified from FTIR spectra in samples prepared at pH 7 or higher (figure IV.2.3b, c).

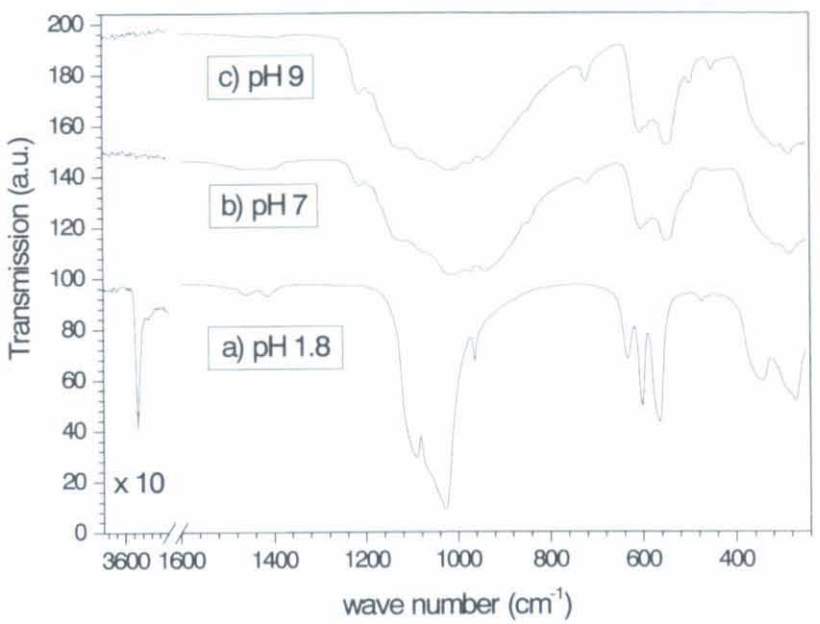

Figure IV.2.3 FTIR spectra of the coatings produced from precursors with different pH.

Here again, no sol-gel reaction could be evidenced during the post-deposition drying step at room temperature, so that a heat treatment was again necessary to achieve the liquid to solid state transformation.

In order to determine the temperature of stabilisation that best suits the formation of HAP, the FTIR spectra of coatings stabilised at 150, 300 and 500°C and finally sintered at 500°C were compared. According to the FTIR results of figure IV.2.4a-c, the stabilisation temperature was finally fixed at 500°C. It can be observed that this temperature (figure IV.2.3c) promotes OH incorporation into the structure (OH bands centred at 3570 and 630 cm^{-1}) at levels not reached after stabilisation at 150 or 300°C.

The presence of structural OH is a sign of the apatite stability. If not otherwise mentioned, the following sections will describe the coatings stabilised at 500°C and obtained from solutions prepared with a Ca/P mr of 10/7 at natural pH (i.e. pH= 1.8).

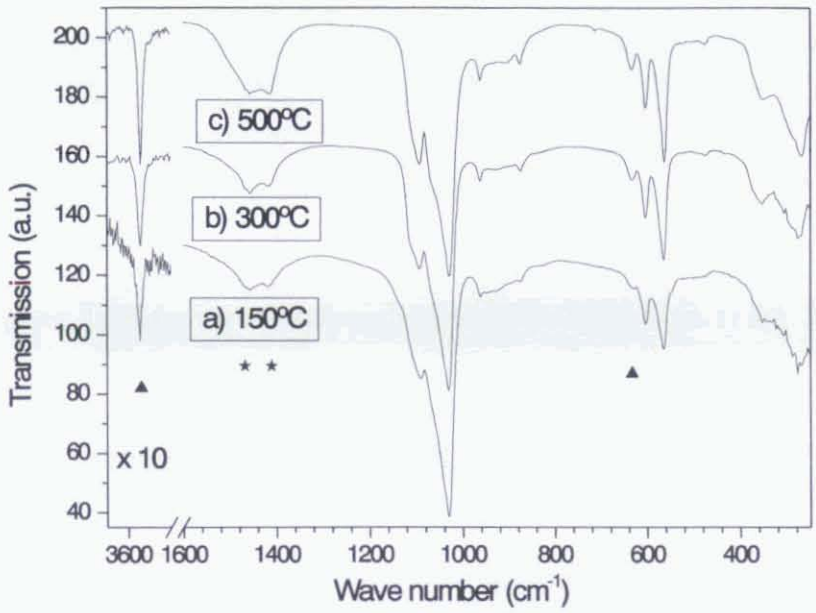

Figure IV.2.4 FTIR spectra of coatings obtained at different stabilisation temperatures and finally sintered at 500°C. ▲: OH, ★: CO_3.

4.3 FTIR CHARACTERISATION.

A) IR bands corresponding to TEP derived CaP coatings.

Characteristic HAP absorption bands [FOW74] were observed in all the sintered coatings. The spectra are presented in figures IV.3.1-IV.3.3. The assignment of the different bands is summarised in Table IV.3.1. Structural hydroxyl groups in the HAP structure generate bands at 3570 (pure stretching band), 630 (librational mode) and 335 cm^{-1} (this last one, produced by Ca-OH stretching, is sometimes observed as a shoulder). Bands located in the range 1030-1090 cm^{-1} are due to asymmetric phosphate stretching modes and those at 960, 605, 570 and 470 cm^{-1} are coincident with symmetric stretching and bending modes from the same group in HAP. Bands corresponding to Ca-PO_4 lattice modes are identified at lower wave numbers (295, 275 cm^{-1}). Additional bands at 940 and 720 cm^{-1} on the one hand and at 1455, 1420 and 875 cm^{-1} on the other, illustrate

differences with respect to a stoichiometric HAP. These bands have been assigned to calcium oxide (CaO) [NYQ97] and carbonate compounds [NAK97], respectively. Finally, several extra bands are punctually observed, depending on the experimental conditions. In the following paragraphs, the respective evolution of the different bands is analysed in relation to the Ca/P mr and sintering temperature.

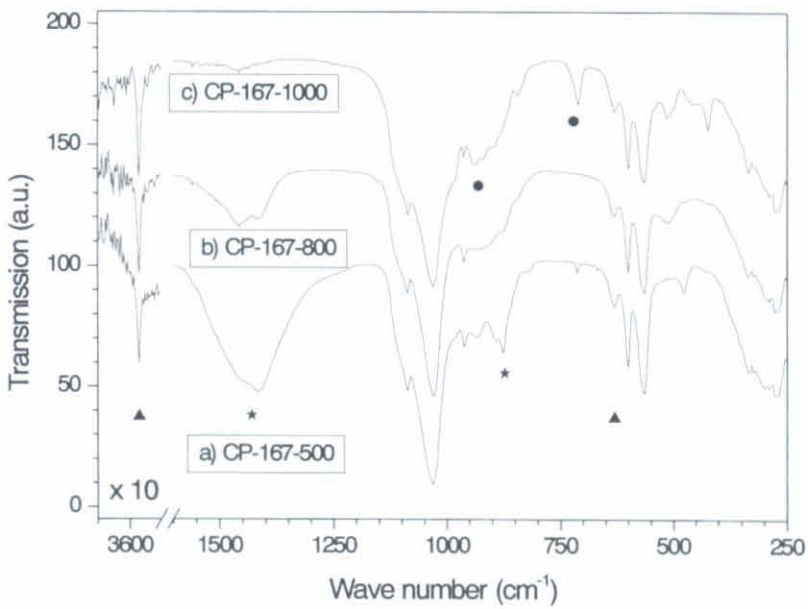

Figure IV.3.1: FTIR spectra of coatings prepared from TEP sols with Ca/P mr=1.67: after sintering at different temperatures. ▲: OH, ★: CO_3, ●: CaO.

CP-167-T coatings: The carbonate bands observed after sintering at 500°C present moderate intensities (figure IV.3.1a). The band at 875 cm^{-1} is more intense than the CaO band at 940 cm^{-1}. It is also observed that the one at 1420 cm^{-1} is more intense than that at 1455 cm^{-1}. For coatings sintered at 800°C, an important change in relative absorbances can be observed (figure IV.3.1b). The carbonate bands suffer a drastic diminution and the CaO band at 940 cm^{-1} becomes more intense than the carbonate band at 875 cm^{-1}. A similar intensity inversion is also observed for the carbonate bands at 1455 and 1420 cm^{-1}. These features appear again more pronounced after sintering at 1000°C (figure IV.3.1c). The carbonate component located at 1455 cm^{-1} has almost disappeared. On the other hand, the CaO absorption band at 720 cm^{-1} experiences a notable absorbance increase. Generally speaking, no significant change is observed in HAP characteristic bands with respect to the sintering temperature.

CP-80-T coatings: The bands described for the CP-167-T coatings are still present. Remarkable differences are however observed in the carbonate groups and CaO bands. The absorption of these bands has diminished for all the sintering temperatures in comparison with the CP-167-T coatings (figure IV.3.2). Only the carbonate band at 875 cm^{-1} remains clearly detectable. The CaO band at 940 cm^{-1} appears as a shoulder.

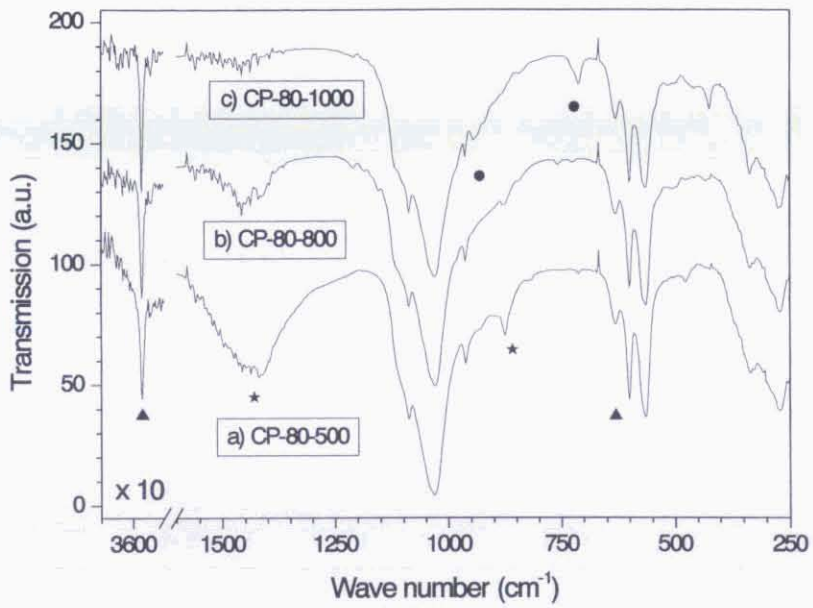

Figure IV.3.2: FTIR spectra of coatings prepared from TEP sols with Ca/P mr= 0.8 after sintering at different temperatures. ▲: OH, ★: CO_3, ●: CaO.

The evolution of band intensity with increasing sintering temperature is similar to the behaviour observed for CP-167-T coatings. This confirms that a carbonate compound is eliminated as a consequence of the sintering treatment. After heat-treatment at 1000°C (figure IV.3.2c), the main features consist in the absoption decrease of the principal carbonate bands and the increase of the CaO band at 720 cm^{-1}. In addition, the hydroxyl bands (especially those at 3570 and 630 cm^{-1}) suffer a slight increase in absorbance when increasing the sintering temperature.

CP-50-T coatings: The decrease of Ca/P mr down to 0.5 leads to notable changes in the films that affect, not only carbonate bands, but also the general composition of the CaP coating. The first remarkable feature is the lower hydroxylation

degree of the coatings, which is evidenced by the weaker absorbance of bands assigned to the hydroxyl groups. As shown in figure IV.3.3, this trend is observed for every sintering temperature. The hydroxyl band at 630 cm^{-1} is only present as a shoulder for the CP-50-800 and CP-50-1000 coatings (figures IV.3.3b and IV.3.3c). This effect is in contrast with the behaviour of the CP-167-T and CP-80-T samples where this band presents a well defined component for every sintering temperature.

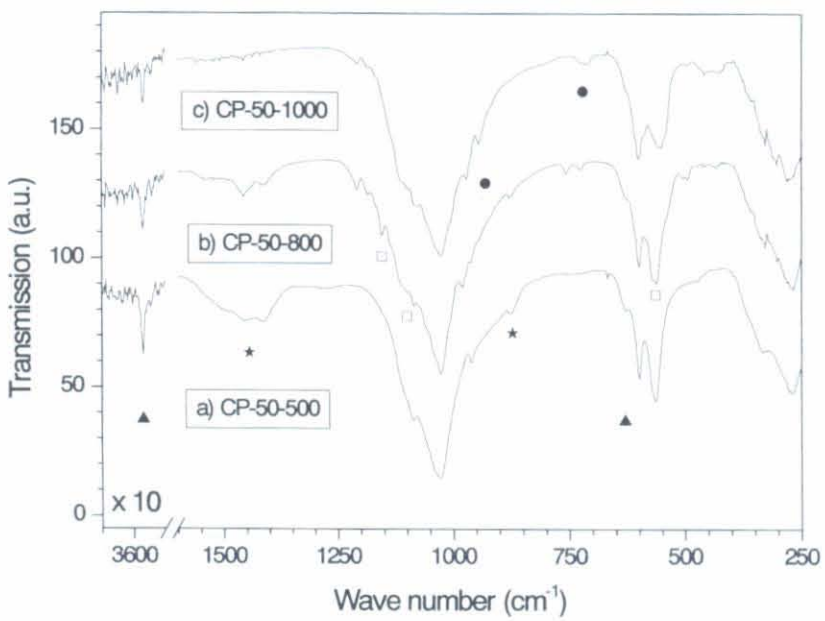

Figure IV.3.3: FTIR spectra of coatings prepared from TEP sols with Ca/P mr= 0.5 after sintering at different temperatures. ▲: OH, ★: CO_3, ●: CaO, □: PO_4 new bands.

For the CP-50-500 coating (figure IV.3.3a), only carbonate bands produce differences with respect to other coatings treated at 500ºC. The diminution of Ca/P mr leads to a lower intensity of carbonate group bands. Figures IV.3.3a and IV.3.2b show that the CP-50-500 coating presents, in terms of carbonate content, a similar composition to that of the CP-80-800 coating. In addition, sintering at 800°C produces substantial modifications in the phosphate absorption region (figure IV.3.3b). Several new bands are observed at 1100 (shoulder) and 1155 cm^{-1}. Partial displacements of the most important HAP bands are also detected (from 1030 to 1025 cm^{-1} for the most intense band) and a double component is formed at 570-560 cm^{-1}. These trends appear again more accentuated after sintering at 1000°C (figure IV.3.3c). The expansion of a

wide band in the 570-560 cm^{-1} region with a critical diminution in absorbance can be also observed.

Wave number (cm^{-1})	Assignment
3570	OH stretching
1455	CO_3 ν_3
1420	CO_3 ν_3
1090, 1070 (sh), 1045, 1030	PO_4 ν_3 antisymmetric stretching
960	PO_4 ν_1 symmetric stretching
940, 720	CaO vibration modes
875	$CO_3^{2}\nu_2$
630	OH librational
605, 570	PO_4 ν_4 Bending mode
470, 462 (sh)	PO_4 ν_2 Bending mode
335, 355 (sh)	Ca-OHν_3 stretching
295	Ca-PO_4
275	Ca-PO_4

Table IV.3.1: Location of the principal FTIR bands (cm^{-1}) observed in the CaP coatings [FOW74, NYQ97, NAK97]. (sh) shoulder.

B) IR bands corresponding to PhAc derived HAP coatings.

As we have already mentioned, in the case of PhAc sols we will only show those experimental results that remain closer to the HAP composition. Again, HAP absorption bands were observed in all the sintered coatings, as shown in figure IV.3.4. Additional bands assigned to CaO and carbonate compounds could also be observed. Several additional shoulders observed in the 900-1100 cm^{-1} region for the highest sintering temperatures are related to the development of a thermal silica layer on the back of the substrate. The most relevant aspects of the bands evolution after sintering at different temperatures are mentioned in the following paragraph.

The carbonate bands observed after sintering at 500°C present moderate intensities (figure IV.3.4a). However, as a comparison with the equivalent coatings from

TEP sols, we can observe that the carbonate content is significantly lower in PhAc derived coatings (see spectra in figure IV.3.2a and figure IV.3.4a). The band at 1420 cm^{-1} is more intense than the one at 1455 cm^{-1}, as it happened after sintering at 500°C for TEP precursors. For coatings sintered at 650ºC or higher temperatures, the aforementioned change in relative absorbances between these two bands can be also observed (figure IV.3.4b). This feature appears again more pronounced after sintering at 800ºC (figure IV.3.4c) and specially at 1000°C (figure IV.3.4d). It is worth mentioning that the hydroxyl bands (especially those at 3570 and 630 cm^{-1}) do not present remarkable changes in transmission when increasing the sintering temperature, as previously observed in the TEP derived coatings.

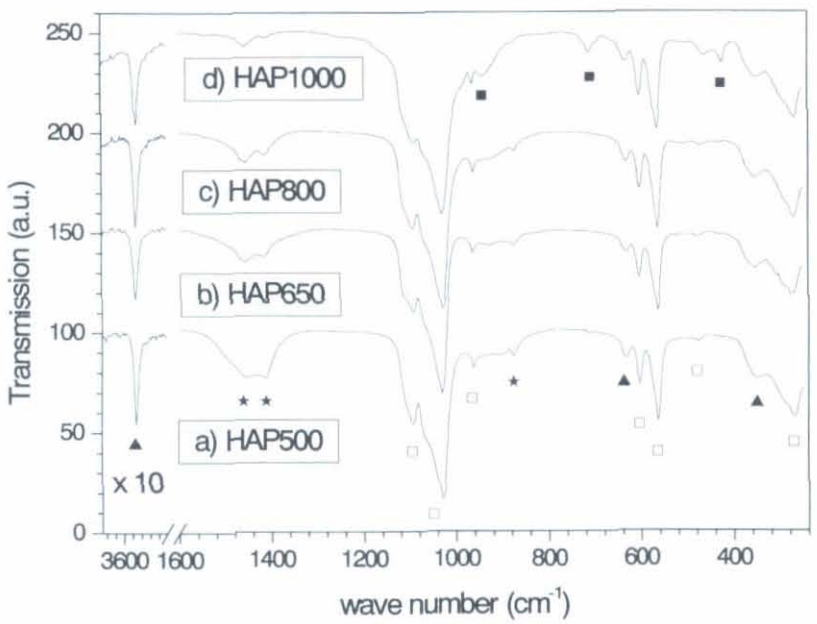

Figure IV.3.4: FTIR spectra of the HAP coatings obtained from PhAc precursors by sintering at different temperatures. ▲: OH, ★: CO_3,: ■ CaO, □: PO_4.

The analysis of the behaviour of the bands associated to carbonate groups, merits a comparison between TEP and PhAc derived HAP coatings. In the case of coatings prepared from TEP precursors, the intensity variations of the main IR bands assigned to carbonate groups (1420 and 1455 cm^{-1}) indicate the presence of two carbonated phases. The evolution of the transmission of the CO_3 bands at 1420 and 1455 cm^{-1} (normalised with respect to the PO_4 band at 1030 cm^{-1}) is plotted as a function of the temperature for

CP-80-T coatings (Figure IV.3.5a). The decay of the carbonate content can be clearly followed, which depicts the carbonate groups decomposition. Furthermore, a change in the most intense band can be detected in the [500 to 800ºC] thermal range. On one side, the remnant band located at 1455 cm^{-1} proves the inclusion of carbonate groups in the apatite structure [ELL94], even after sintering at 800ºC or more. On the other, a CaCb phase, evidenced by the appearance of a band at 1420 cm^{-1} [NAK97] after sintering at 500ºC is observed to vanish more rapidly than the first one after sintering at 800ºC or more, showing the CaCb decomposition.

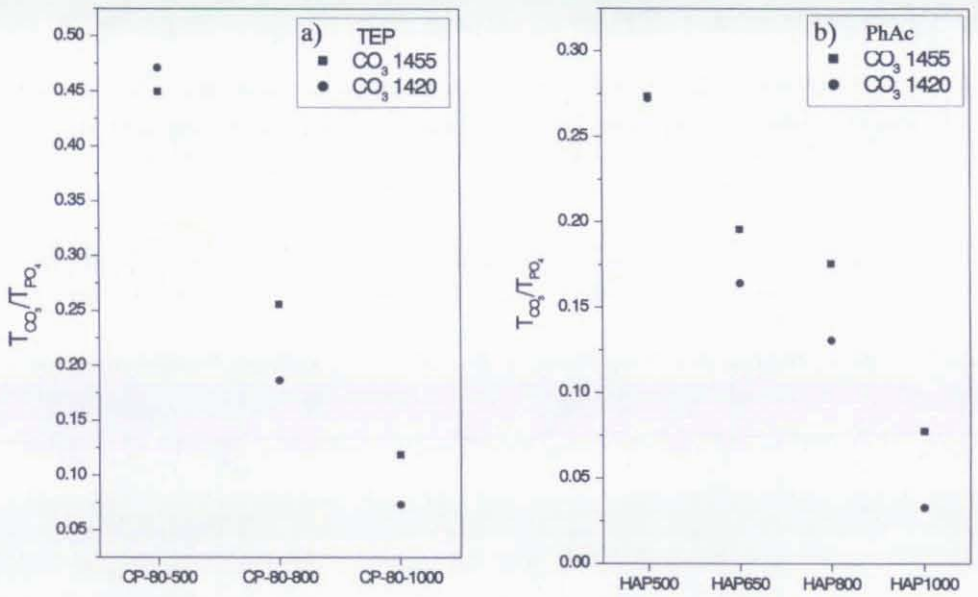

Figure IV.3.5: Evolution of the IR transmission of the CO_3 bands at 1420 and 1455 cm^{-1} plotted as a function of temperature. a) TEP and b) PhAc derived HAP coatings. The have been normalised with respect to the PO_4 band at 1030 cm^{-1}.

In the case of coatings produced from PhAc precursors, the intensity variations of the main IR bands assigned to carbonate groups have been also observed (figure IV.3.5b), indicating the presence of the two carbonated phases.

4.4 STRUCTURE OF AEROSOL-GEL HAP COATINGS.

Structural information obtained by XRD is essential for the interpretation of the mechanisms taking place during coating formation and sintering. In fact, this technique

clarifies the analysis made by FTIR. From a general point of view, all the phases detected by XRD after sintering at 500°C or more appeared polycrystalline and the presence of amorphous phases was negligible, as deduced from the well defined peaks in the diffraction patterns.

A) TEP derived CaP coatings.

CP-167-T coatings: The diffraction patterns show a continuous evolution of the structure with increasing temperatures. The CP-167-500 coating is composed of HAP as dominant phase ($Ca_{10}(PO_4)_6(OH)_2$, PDF 9-0432) and calcium carbonate (calcite, PDF 05-0586) as a secondary component. The diffraction peaks corresponding to both phases are indexed in figure IV.4.1a. Sintering at 800°C drastically changes the diffraction pattern (figure IV.4.1b). New reflections due to CaO (lime, PDF 37-1497) replace the $CaCO_3$ (CaCb) peaks.

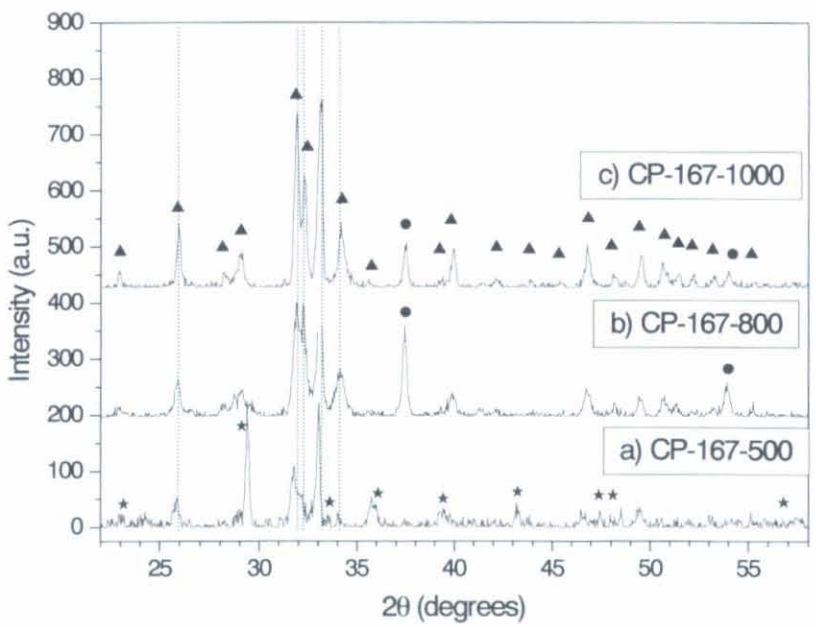

Figure IV.4.1: XRD patterns of coatings prepared from TEP sols with Ca/P mr= 1.67 after sintering at different temperatures. ▲: HAP, ★: CaCb, ●: CaO.

The CP-167-1000 coating pattern (figure IV.4.1c) shows a significant diminution in the intensity of the CaO peaks, which indicates a partial decomposition of this compound in the coating. Another remarkable feature is that the crystalline order in the

HAP structure has notably increased, as deduced from the presence of narrower diffraction peaks.

CP-80-T coatings: The patterns of CP-80-T coatings present similarities with the corresponding CP-167-T patterns. The peaks present in the CP-80-500 pattern (figure IV.4.2a) show that phases detected in the CP-167-500 layers are still present; nevertheless, some major changes are evidenced in terms of HAP film purity. A much lower CaCb contribution is observed after sintering at 500°C (figure IV.4.2a). After sintering at 800°C, the diffraction pattern fits fairly well with HAP standards (figure IV.4.2b). Only a very small reflection from the most intense CaO peak (200) is still observed at 37.3°. This peak, still detectable after sintering at 1000°C (figure IV.4.2c), indicates that CaO is a very stable compound. In addition, the lower value for the full width at half maximum (FWHM) of HAP peaks reveals an increase of the crystallite size.

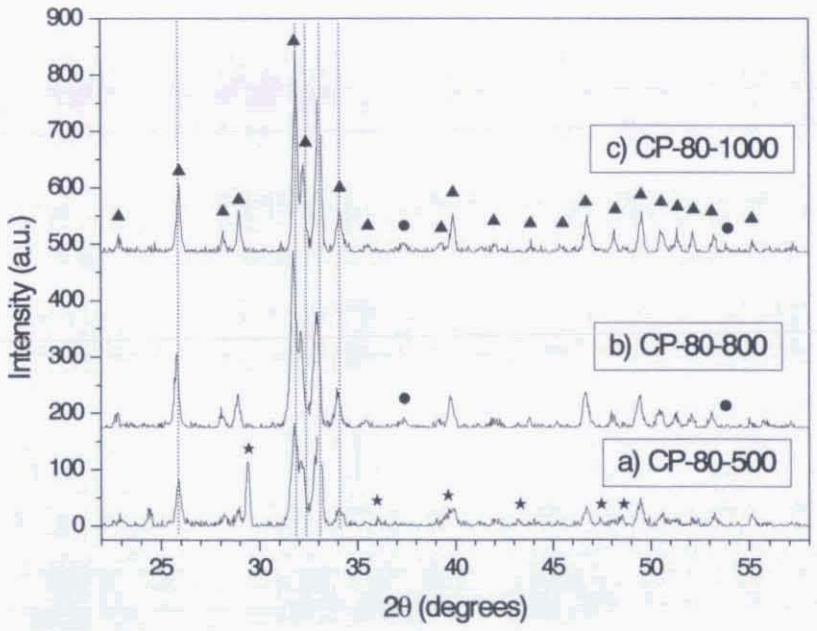

Figure IV.4.2: XRD patterns of coatings prepared from TEP sols with Ca/P mr= 0.8 after sintering at different temperatures. ▲: HAP, ★: CaCb, ●: CaO

CP-50-T coatings: The drastic differences depicted by FTIR spectroscopy for CP-50-T coatings have been confirmed by XRD results. New CaP compounds different from HAP have been evidenced for these coatings (figure IV.4.3). The new components

have not been clearly identified in the case of the CP-50-500 coating. Besides, CaCb peaks are almost not detected (figure IV.4.3a) showing that a higher phosphate concentration leads to a lower CaCb formation in the coatings. New peaks observed for the coating sintered at 800°C (figure IV.4.3b) have been assigned to β-TCP, which suggests that new FTIR features observed for this film (additional bands and band displacement) can be attributed to this phase. As shown in the pattern of the CP-50-1000 coating (figure IV.4.3c), sintering at 1000°C activates the aforementioned structural modifications. The comparison with HAP peaks shows that the β-TCP phase is now dominant. These features confirm that critical changes in the structural composition of sintered CaP coatings are induced when the phosphorus concentration in the solution is increased. An interesting feature, observed in the CP-50-1000 pattern, is the huge intensity of the (300) peak at 29.62°, which reveals a preferential orientation of the β-TCP crystallites.

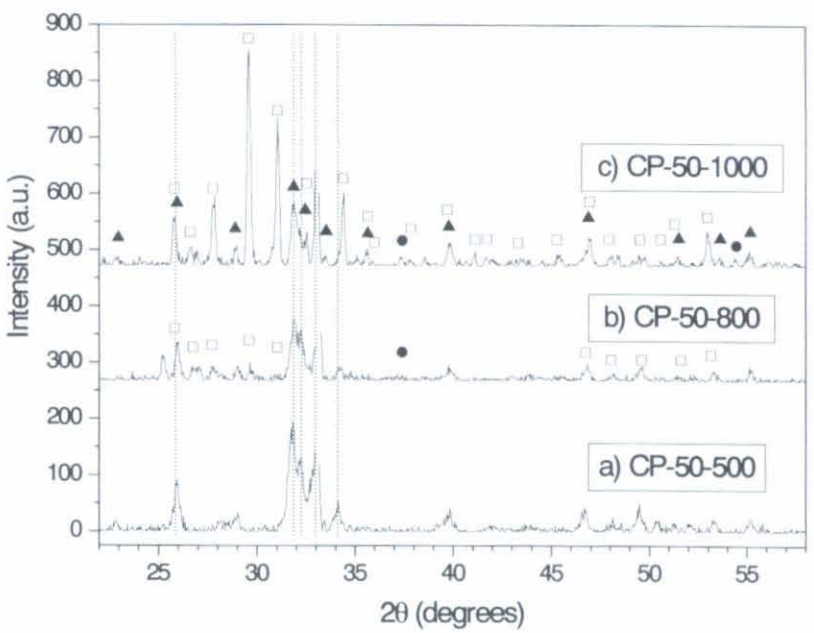

Figure IV.4.3: XRD patterns of coatings prepared from TEP sols with Ca/P mr= 0.5 after sintering at different temperatures. □: β-TCP, ▲: HAP, ●: CaO

B) PhAc derived HAP coatings.

HAP coating diffractograms show again an evolution of several structures for increasing sintering temperatures. The HAP500 coating (figure IV.4.4a) is composed of

a HAP dominant phase with traces of calcium carbonate at 29.3° (calcite). Note that, confirming FTIR results, the formation of carbonate from PhAc precursors is weaker than for TEP precursors (compare figure IV.4.2a and IV.4.4a). Sintering at 650°C or higher temperatures produced noticeable changes in the diffractograms (figure IV.4.4b), which fit fairly well the one of HAP standards. CaCb is pyrolysed and transformed into CaO by sintering at 650°C, as proved by the absence of the $CaCO_3$ XRD peak and the presence of the CaO (200) peak at 37.4°. The pattern of the HAP800 coating (figure IV.4.4c) shows a significant diminution in the intensity of the CaO peak. However, the thermal stability of the CaO component is denoted by the weak 200 reflection, still detectable after sintering at 1000°C (figure IV.4.4d). Again, the thermal activation leads to narrower diffraction peaks (i.e. lower FWHM) denoting an increase in the crystallite size.

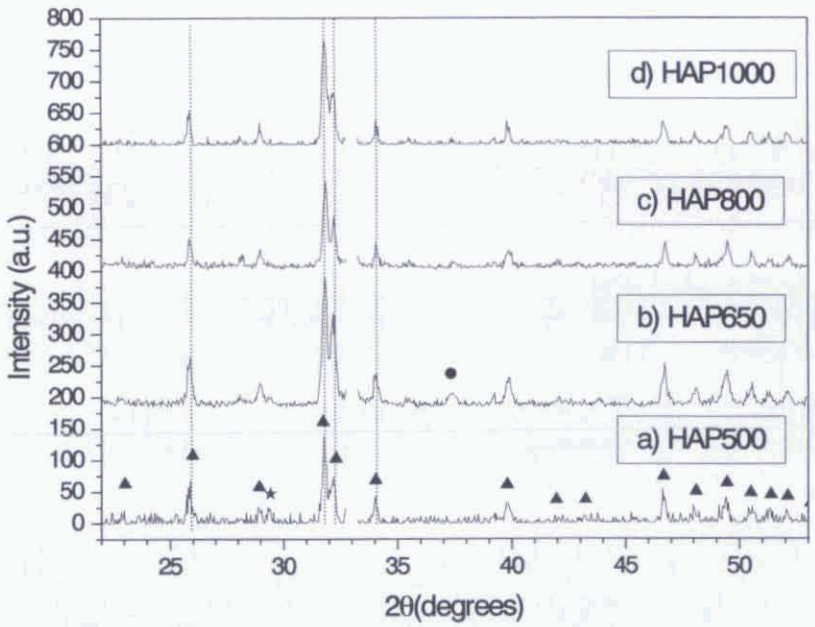

Figure IV.4.4: XRD patterns of coatings prepared from PhAc sols after sintering at different temperatures. ▲: HAP, ★: CaCb, ●: CaO

Concerning microstructural features, we have evaluated the rate of preferential growth of HAP along the <001> direction by normalising the intensity of the (002) XRD peak (at 25.88°) in relation to the most intense (211) peak at 31.84°. Figure IV.4.5 presents the evolution of the $I_{(002)}/I_{(211)}$ ratio as a function of temperature.

This preferential growth direction has been proposed to be responsible of the needle like shape of HAP crystallites [EBR93]. In this work, both TEP (CP-80-T) and PhAc derived HAP coatings showed that the sintering temperature has an influence in changing the relative size of HAP crystals. It can be observed that, for both TEP and PhAc derived HAP coatings, there is a clear diminution of the $I_{(002)}/I_{(211)}$ ratio for increasing sintering temperatures, which implies a relative diminution of the <001> orientation. It is likely that the first steps of crystallisation are dominated by the growth along the c axis. However, once the structure is stabilised, the crystal growth becomes random, rather than preferential along any crystalline direction.

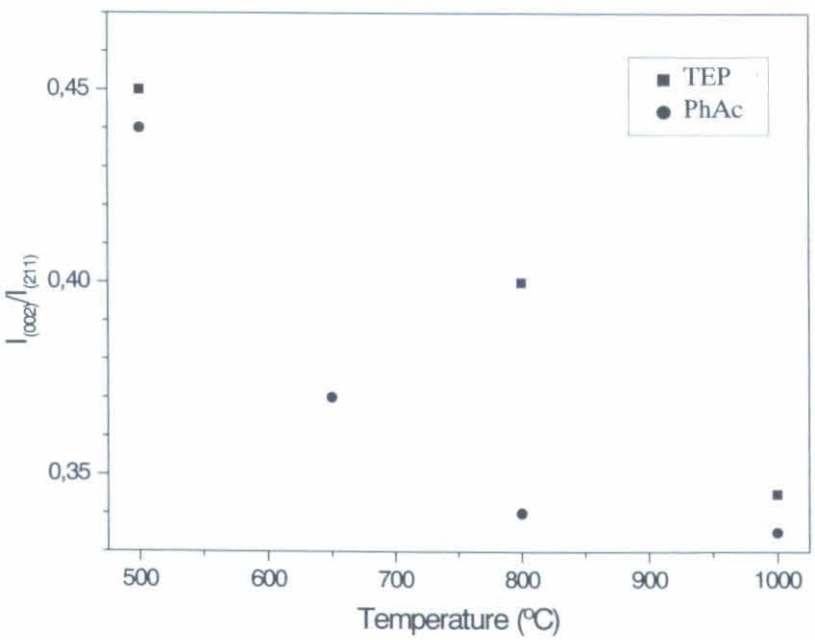

Figure IV.4.5: Evolution of the normalised $I_{(002)}$ intensity as a function of the sintering temperature for both TEP and PhAc derived HAP.

4.5 MORPHOLOGY AND SEMIQUANTITATIVE STOICHIOMETRY ANALYSIS.

The SEM images presented in this section give relevant information concerning the surface morphology of the coatings in the micrometer scale. EDX analysis has been used for a quick exploration of the Ca/P mr evolution for different stoichiometries or sintering temperatures.

A) TEP derived CaP coatings.

The evolution at different sintering temperatures of the coatings prepared from TEP solutions with different Ca/P mr have been studied and are presented in the following paragraphs.

CP-167-T coatings: The coatings formed from solutions containing a Ca/P mr of 1.67 present characteristic morphologies. Figure IV.5.1a, which corresponds to a CP-167-500 coating, shows a rough structure formed of uniformly compacted granules. Sintering at 800°C induces a granule coalescence process, which drastically reduces the surface roughness (figure IV.5.1b). This tendency is confirmed after sintering at 1000°C (figure IV.5.1c).

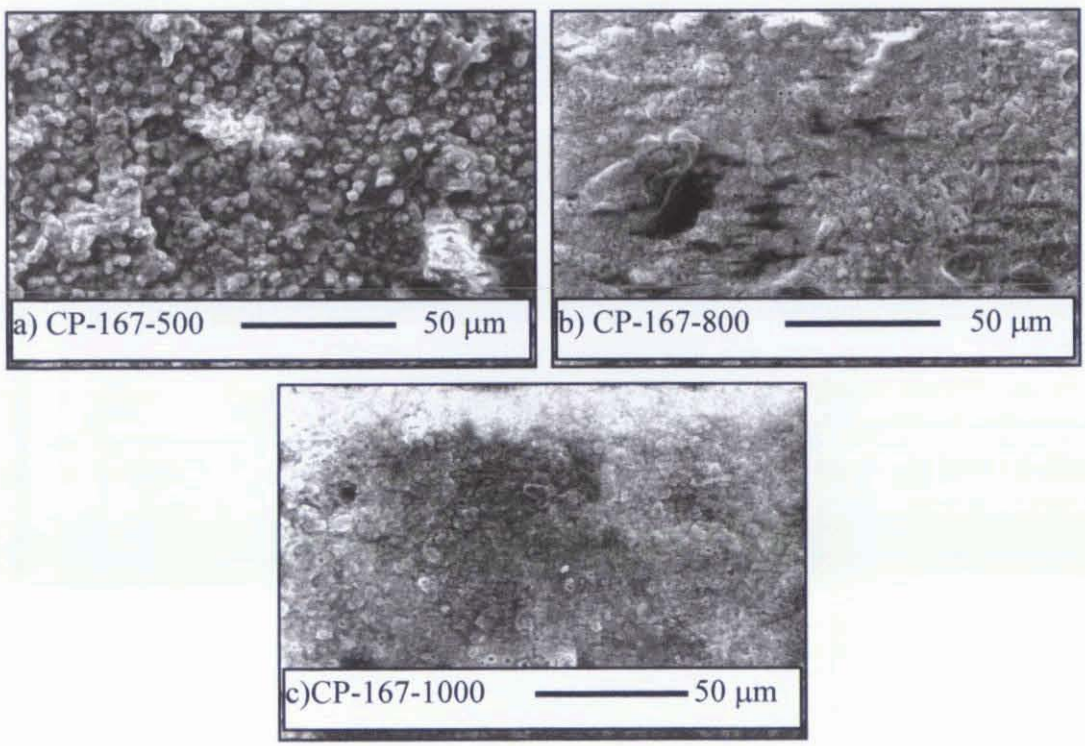

Figure IV.5.1: SEM micrographs of coatings prepared from TEP sols with Ca/P= 1.67 after sintering at different temperatures.

CP-80-T coatings: Remarkable differences in surface morphology are detected in comparison with the previously described coatings. Figure IV.5.2a shows the *extremely high porosity and the large pore size distribution (1 to 10 microns) observed* in the case of CP-08-500 coatings. After sintering at 800°C, the coatings remain highly porous although the size of the pores decreases, leading to a slightly more uniform film (figure IV.5.2b). This trend is confirmed after sintering at 1000°C (figure IV.5.2c). In addition, thermal stresses, induced by the heat treatment at 1000°C, lead to the appearance of cracks at the CP-80-1000 coating surface.

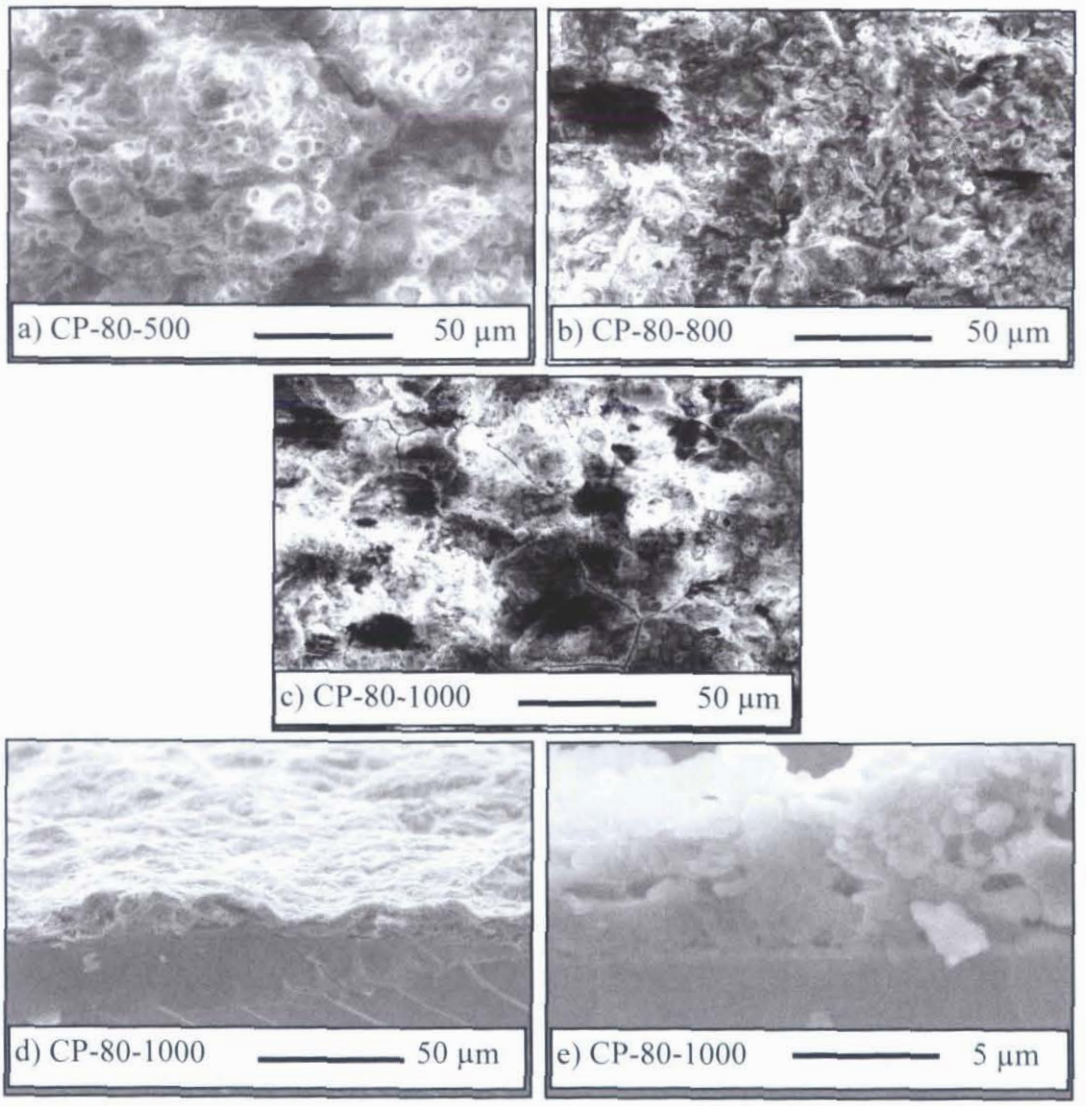

Figure IV.5.2: SEM micrographs of coatings prepared from TEP sols with Ca/P= 0.8 after sintering at different temperatures. a)-c) surface view. d),e) cross section view.

The morphology of a CP-80-1000 coating was also studied by SEM cross section observations. The low magnification perspective view (figure IV.5.2d) shows that even the most compact coatings present a rough surface with important topographic variations. A greater magnification (figure IV.5.2e) shows that the coating is formed of well adhered granules leaving internal spaces that produce a highly porous structure.

CP-50-T coatings: Figure IV.5.3a presents the surface morphology of a CP-50-500 coating. The observations previously made for a CP-80-500 coating are also valid here. The existence of a characteristic porosity and pore shape are common features for both coatings. A decrease in pore size is observed when increasing the sintering temperature (figures IV.5.3b and IV.5.3c). However, for any sintering temperature the CP-50-T coatings appear less compact and homogeneous than the corresponding CP-80-T coatings. Cracks are again observed after sintering at 1000°C.

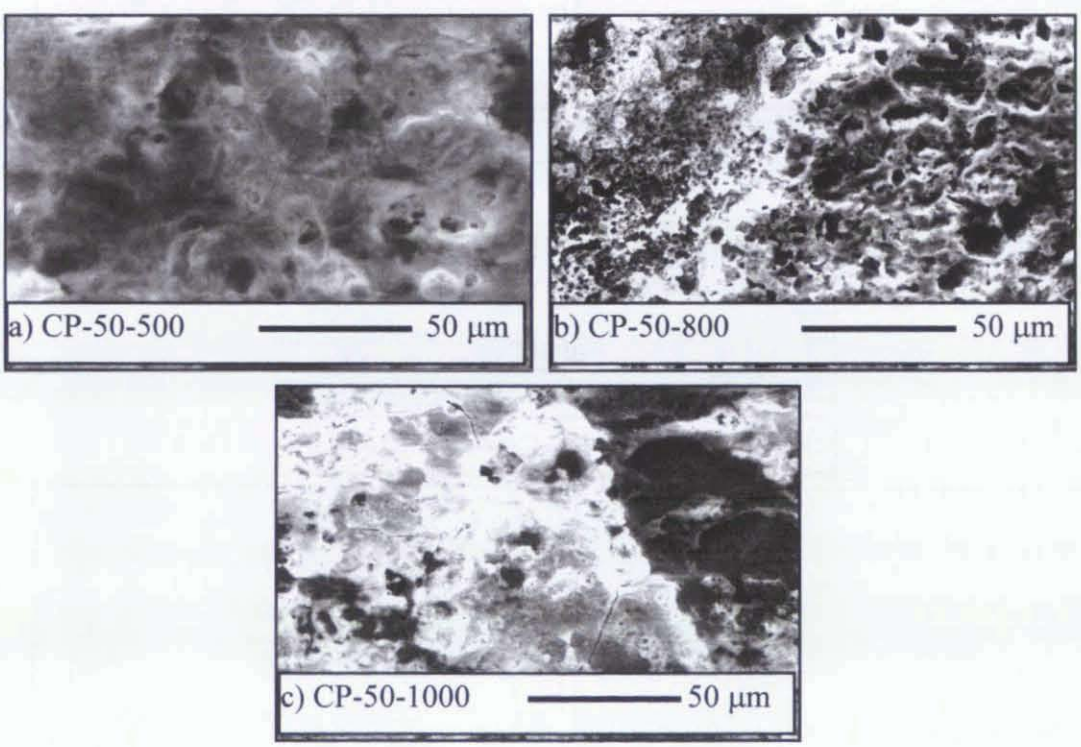

Figure IV.5.3: SEM micrographs of coatings prepared from TEP sols with Ca/P= 0.5 after sintering at different temperatures.

EDX analysis (image IV.5.4) was performed to estimate the Ca/P mr of the CaP coatings. The system was previously calibrated with a HAP standard (Strem chemicals).

The most interesting results, in terms of pure HAP film formation, were obtained for the CP-80-T coatings. The Ca/P mr was found to be 1.82 +/- 0.08. This value is only slightly higher than the stoichiometric HAP value (1.67) and is in agreement with the small amount of CaO detected by XRD. It was also found that coatings formed from stoichiometric solutions (CP-167-T) were highly overstoichiometric in calcium, while coatings obtained from P rich solutions (CP-50-T) presented a notable calcium substoichiometry (table IV.5.1).

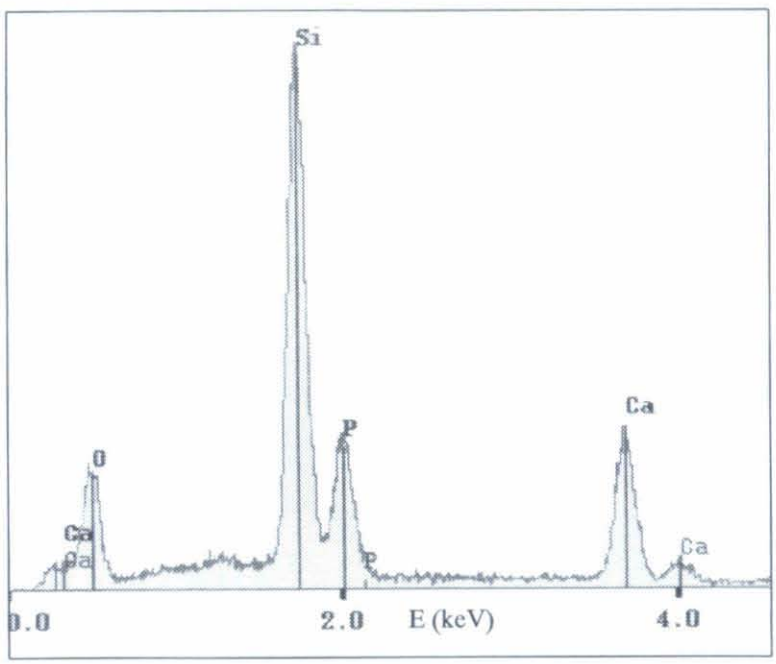

Figure IV.5.4: EDX microanalysis of a CP-50-500 coating.

	CP-50-800	**CP-80-800**	**CP-167-800**
Ca/P mr	1.55 +/- 0.08	1.82 +/- 0.08	1.93 +/- 0.08

Table IV.5.1: Estimations of the Ca/P mr by EDX for different compositions of TEP sols. Coatings were sintered at 800°C.

B) PhAc derived HAP coatings.

The SEM images presented in figure IV.5.5 show the dependence of the surface morphology on sintering temperature. Figure IV.5.5a, which corresponds to a HAP500

coating, shows a rough structure with a high level of porosity. The grain size distribution cannot be studied due to the absence of contrast at the grain boundaries. The morphology of a HAP500 coating was also studied by SEM cross-section observations. The perspective view (figure IV.5.5b) shows that the high porosity of the coating is not only a surface feature. The pores (2 μm mean size) are formed and isolated during the multicoating process. The well-adhered granules leave several internal voids that produce the highly porous structure. This view shows also a rough structure with significant topographic variations which confirm the top view observations.

Sintering at 650 or 800°C induces a coalescence process, which drastically reduces the pore size and gives a more uniform appearance to the film (figure IV.5.5c). This tendency is reversed after sintering at 1000°C since the high temperature induces grain coarsening, which leads to the formation of micro-cracks (figure IV.5.5d).

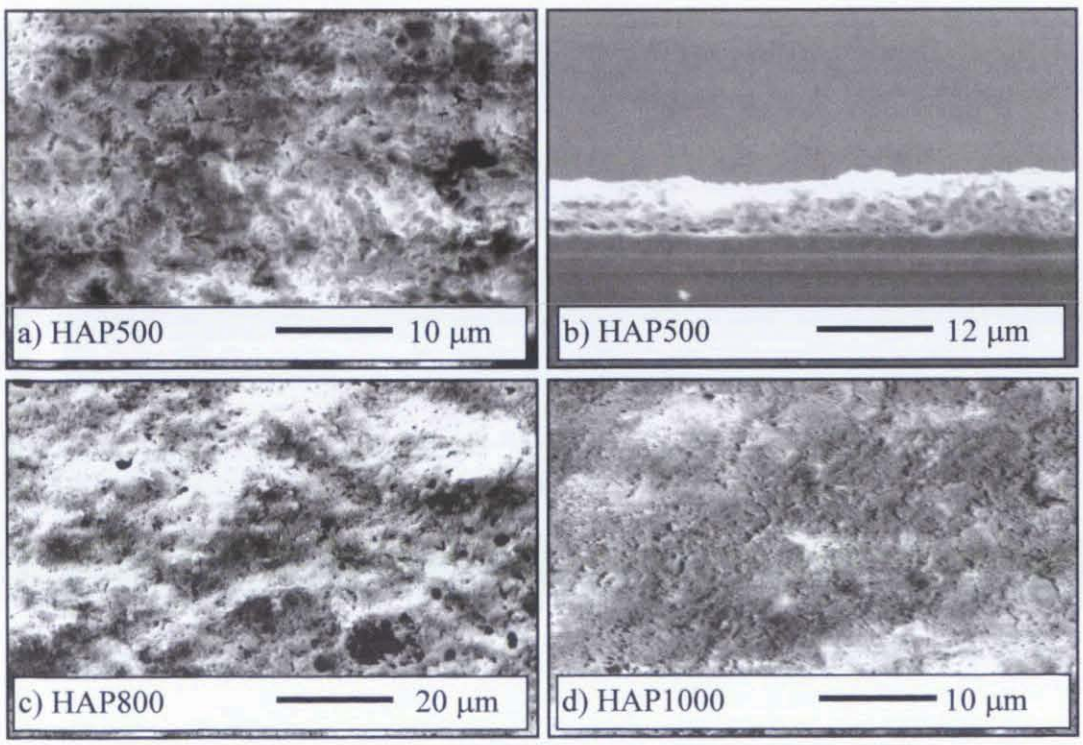

Figure IV.5.5: SEM micrographs of PhAc derived HAP coatings: a) surface image of a HAP500 coating, b) cross section view of a HAP500, c) a HAP800 and d) a HAP1000 coating.

EDX analysis was performed to estimate the Ca/P mr of the coatings and its evolution with sintering temperature (Table IV.5.2). The system was again calibrated with a HAP standard. The results obtained for the HAP500 coating showed that the Ca/P mr was 1.80+/- 0.04. This value is only slightly higher than the stoichiometric HAP value (1.67) and is in agreement with the small amount of $CaCO_3$ detected by XRD. Coatings sintered at higher temperatures presented a similar deviation from the HAP stoichiometric value reaching a Ca/P mr of 1.76+/- 0.04 for the HAP1000 coatings.

	HAP500	**HAP650**	**HAP800**	**HAP1000**
Ca/P mr	1.80 +/- 0.08	1.82 +/- 0.08	1.80 +/- 0.08	1.76 +/- 0.08

Table IV.5.2: Estimations of the Ca/P mr by EDX for the coatings prepared from PhAc and sintered at different temperatures.

4.6 AUGER SPECTROSCOPY.

In order to ascertain the quantitative composition of our coatings, CP-80-T samples were reproduced on TiAlV alloys for Auger characterisation. This substrate allowed a more reliable detection due to a better electric charge conduction. Furthermore, the coatings were chemically etched in order to obtain a thin layer that minimised electron charging effects due to the insulating HAP phase. The Auger spectrum corresponding to the CP-80-800 coating is presented in figure IV.6.1 in comparison with the spectrum of a HAP standard (Strem chemicals), which was studied after uniaxial pressing on a Cu holder. The use of a HAP standard was preferred rather than the use of sensitivity factors due to the drastic variations of these factors with the chemical environment of the P atom [RAE84]. In the form of a phosphide the sensitivity of the P atom is higher than in the form of a phosphate. This is plausibly produced by the presence of $P_{L23}O_{L23}O_{L23}$ cross transitions [WIL85].

The spectra were normalised with respect to the P_{LMM} transition, so that they present identical peak to peak intensities at 120 eV. Both spectra are very similar but it

is worth mentioning that CP-80-800/TiAlV presents slightly higher peak to peak intensities at the Ca_{LMM} transition, which establishes a Ca concentration about 11% higher than the one corresponding to the HAP standard. The O_{KLL} transition presents also a higher intensity in the CP-80-800/TiAlV sample. A chemical shift can be consistently observed in the spectra. This shift, specially accused in the Ca transition, can be assigned to a preferential charging process in the HAP standard. Note that the phosphate transition is clearly split into two components. This splitting may have an influence on the Ca overstoichiometry at the substrate interface of the CP-80-800 coating.

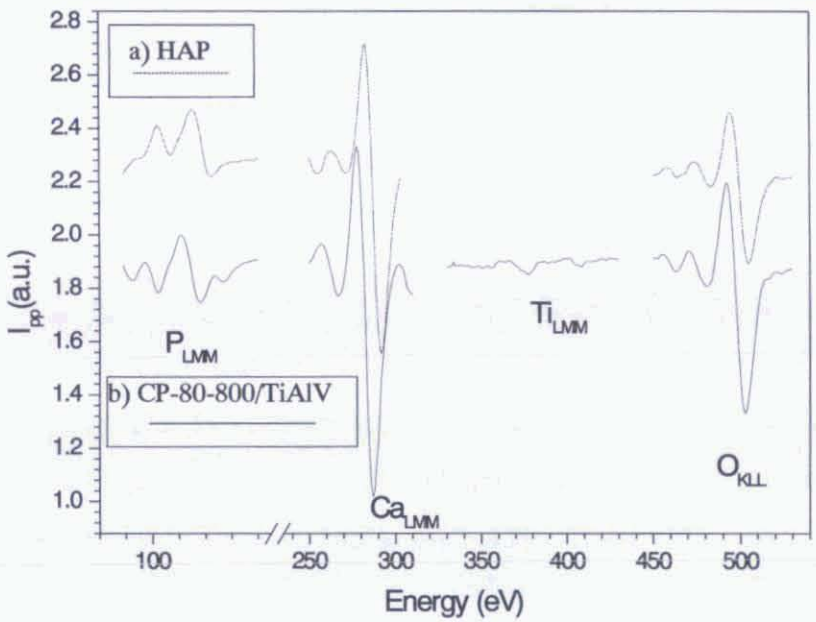

Figure IV.6.1: Auger spectra of a) an HAP standard and b) a CP-80-800/TiAlV coating in the spectral region corresponding to PLMM, CaLMM, TiLMM and OKLL transitions.

4.7 TEM: MICROSTRUCTURE AND MORPHOLOGY.

For this study, two sample preparations were performed, depending on the precursor nature. For TEP derived CP coatings, observation was performed on thin fragments scraped from the coatings. PhAc derived HAP coatings were observed in cross section, following the procedure described in Annex I. A cross section observation

presents several advantages. The main one refers to the possibility of identifying self-organisation in the coating structure (grain and crystalline conformation, substrate influence in coating growth, etc). This information is not obtained for scraped particles, since all relations between neighbour grains or between the coating and the substrate are modified or destroyed.

A) TEP derived CaP coatings

CP-80-500 and CP-80-800 coatings were compared with respect to their morphology and microstructure. Concerning morphologic features, TEM observations show that the coatings porosity is a relevant feature, not only in the μm scale (as depicted by SEM), but also in the nm scale. The evolution of this porosity with sintering temperature is consistent with SEM results, i.e. the HAP grains suffer a coalescence process for increasing temperatures. Figure IV.7.1 shows the distribution of nm structures decorating the CP-80-500 coating (a) and the more homogeneous appearance of a grain scraped from the CP-80-800 coating (b).

Concerning microstructural features, both CP-80-500 (figure IV.7.2a) and CP-80-800 selected area diffraction (SAD) diagrams (figure IV.7.3a) present well defined rings that denote dominant polycrystalline structures, as already derived from XRD. Several crystals that compose the coatings were resolved by means of high resolution images. As an example, crossing (100) and (101) planes with interplanar distances of 3.16 and 5.32 Å, respectively, are observed in figure IV.7.2b that corresponds to a CP-80-500 coating.

High resolution images were also obtained for a CP-80-800 coating (Figure IV.7.3b). In this case, a relevant information concerning grain boundaries was obtained. Figure IV.7.3b shows two neighbouring HAP crystals along the (001) planes, which have grown until the formation of a neat interface. It can be seen that no alternative or amorphous phase is formed in-between the crystals. The absence of an additional interfacial phase is considered to be a clear evidence of the good stoichiometry of the HAP coatings, i.e. a non-stoichiometric HAP coating should yield non-stoichiometric

CP phases between neighbouring HAP crystals. This is also a confirmation of the appropriateness of the 800ºC sintering, i.e. the thermal activation is high enough to provide crystal growth through the whole grains.

B) PhAc derived HAP coatings.

In the case of PhAc derived HAP800 coatings, cross section images enabled us to evidence the crystalline layout of the coating. The SAD diffraction pattern (figure IV.7.4a) proves that nearly hexagonal grains with well defined boundaries observed in figure IV.7.4b are crystalline and present random orientations. The presence of pores in the nanometer scale has also been evidenced in these coatings (clear areas in figure IV.7.4c). It is relevant that the porous structure is still observable after ion etching, since this process usually tends to homogenise the surface, erasing thus any surface decoration. Concerning high resolution observation of HAP1000 coatings, Figure IV.7.5a shows a conformation of several HAP crystals in a similar arrangement to that observed in figure IV.7.4b. In this case, the crystallinity is evidenced by an organisation of the structures along the (100) planes. Furthermore, the same structure has been resolved in two dimensions along the [001] zone axis. $(1\bar{0}0)$, (010) and (110) planes with interplanar distances of 8.14 Å can be observed in the magnified image of figure IV.7.5b, which reveals the hexagonal structural organisation of the HAP crystallites.

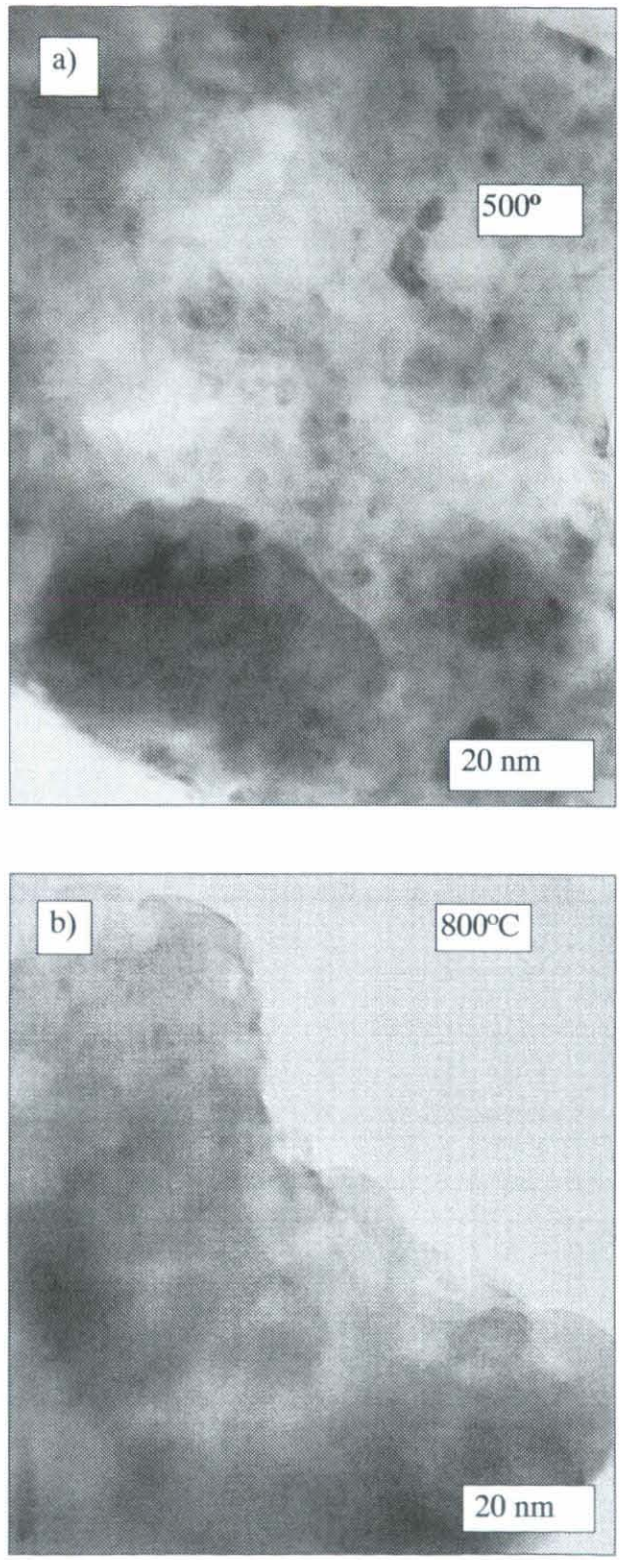

Figure IV.7.1: TEM images of grains scraped from a) a CP-80-500 coating, b) a CP-80-800 coating.

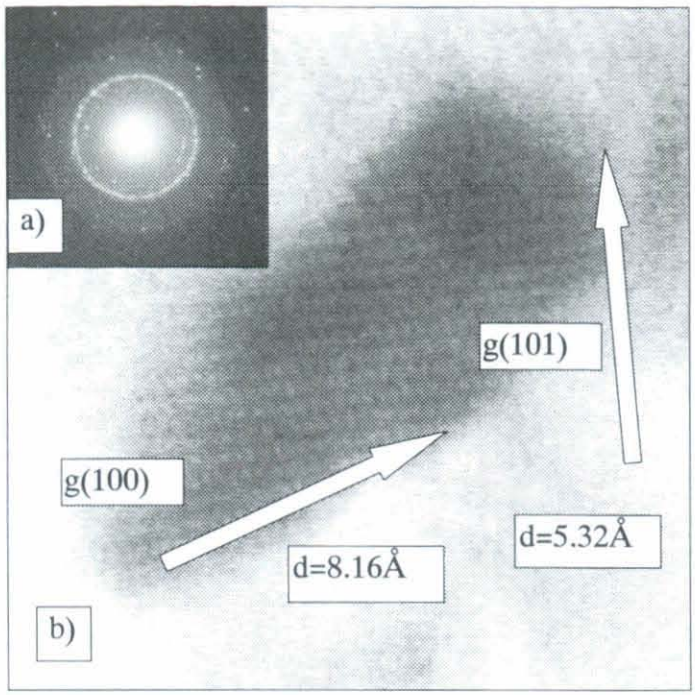

Figure IV.7.2: TEM analysis of a grain scraped from a CP-80-500 coating: a) SAD pattern, b) (100), (101) structure.

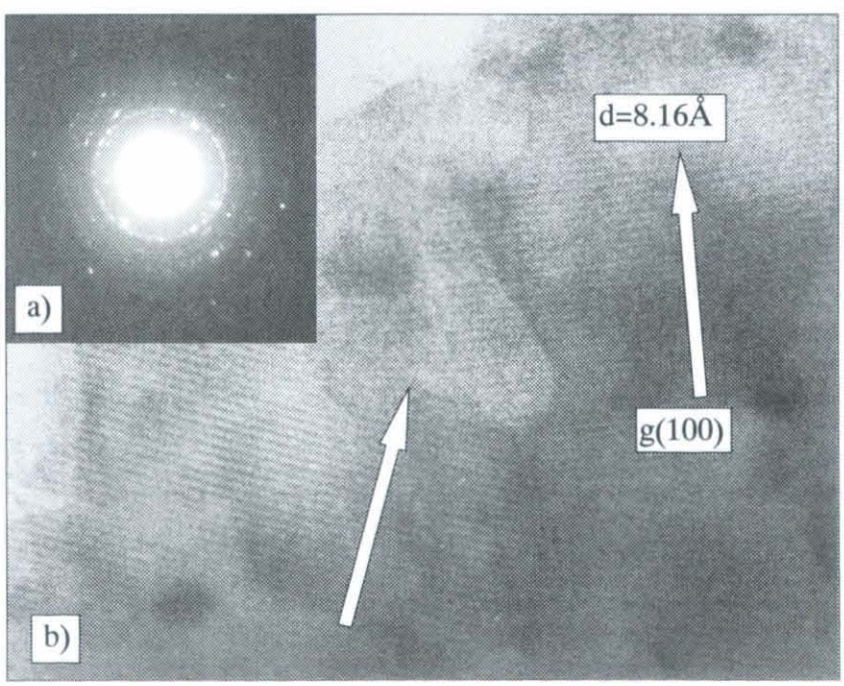

Figure IV.7.3: TEM analysis of a grain scraped from a CP-80-800 coating: a) SAD pattern, b) two neighbour crystals observed along the (100) planes.

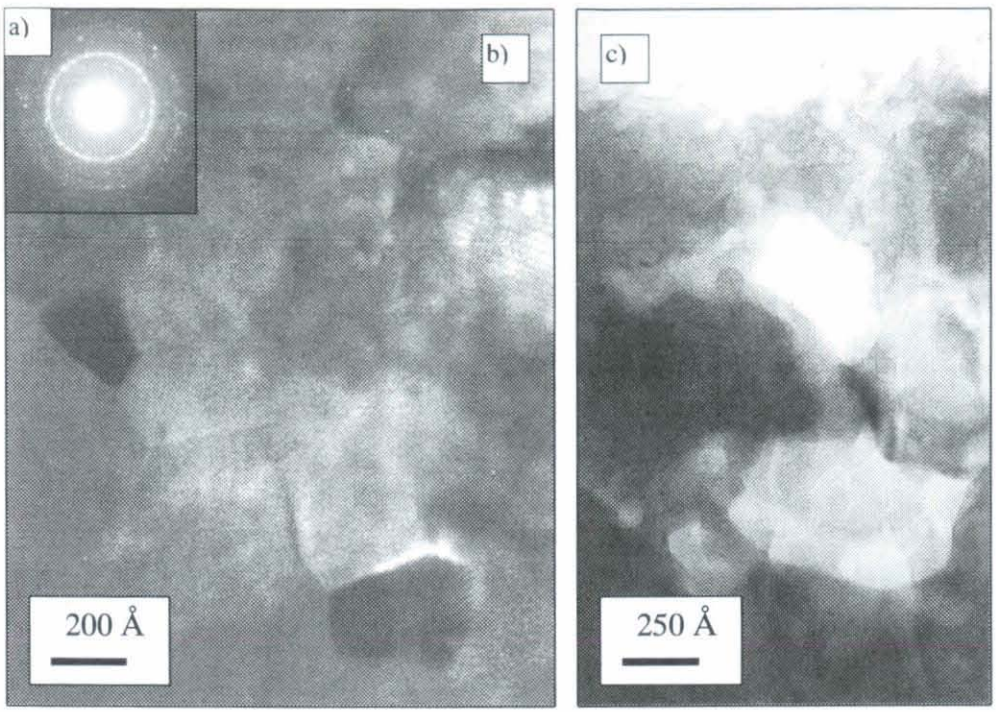

Figure IV.7.4: TEM cross section images from a HAP800 coating. a) SAD pattern, b) grain boundaries, c) porous structures.

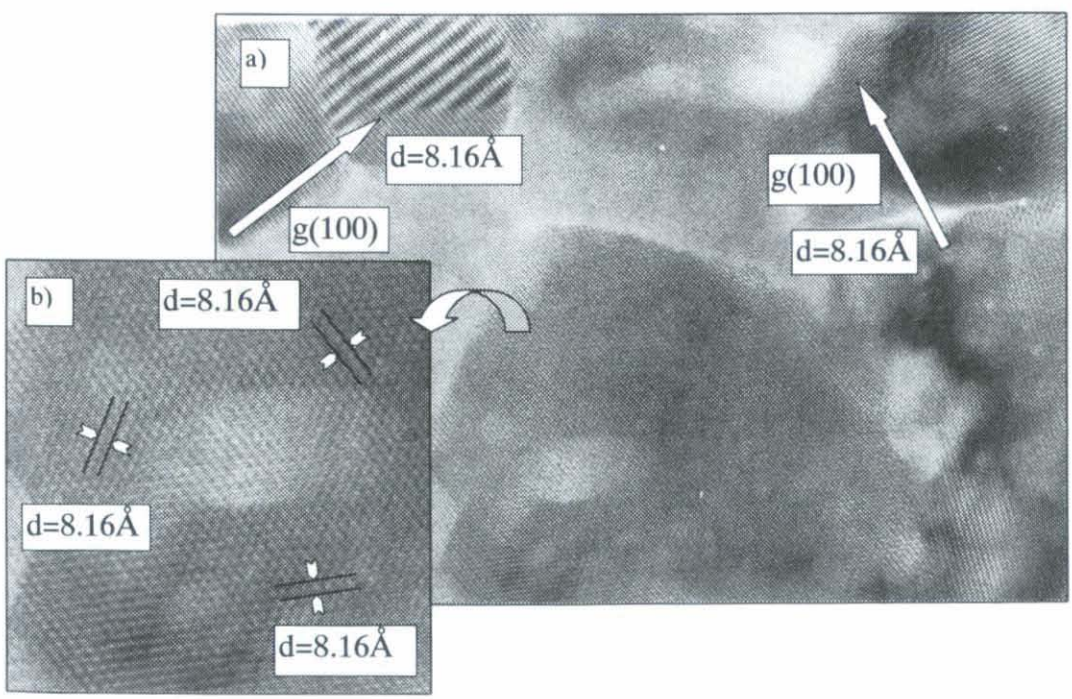

Figure IV.7.5: TEM cross section images from a HAP800 coating: a) crystal conformation, b) magnified area observed along the [001] zone axis, showing (100), (010) and $(1\bar{1}0)$ planes of the HAP crystallites hexagonal structure.

4.8 ADHESION STRENGTH. INDENTATION STUDIES.

Adherence tests were performed on HAP coatings prepared from TEP precursors and grown on TiAlV substrates. Figure IV.8.1 presents a standard loading curve obtained on the CP-80-800/TiAlV coating by using the Berkovich indenter. Special attention was paid to avoid the probe to approach the TiAlV substrate. The testing process can be described as follows. Initially, small instabilities are observed due to friction phenomena, until the probe is stabilised on the coating surface. The load follows then a semi-hyperbolic dependence until depths of approximately 1 μm are reached. From there on, a point of inflexion appears, the slope diminishes and a drastic jump depth is observed, which can be related to a catastrophic failure of the coating. The loading process continues then with several friction instabilities until a maximal load of 30 mN is reached. When the load is decreased, the probe recovers freely, as denoted by the almost vertical unloading process.

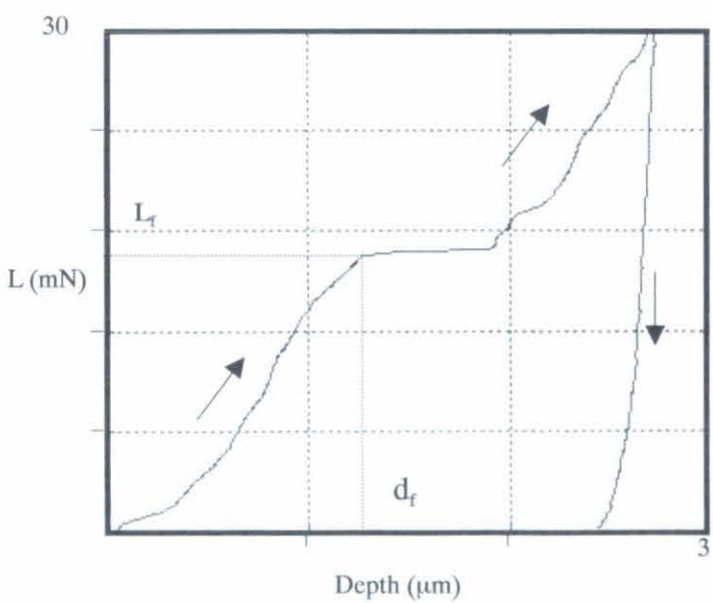

Figure IV.8.1: Adhesive strength tests performed by indentation on the CP-80-800/TiAlV coating with a 30 mN maximal load.

For statistical purposes, the experiment was repeated twenty times. The data obtained from an analysis of the different curves show that the mean failure load L_f is

11.0 mN (minimal L_f 5.60 mN) and the mean failure depth d_f is 1.15 μm (minimal d_f 0.75 μm). These values suggest, via a calculation of the area of contact, that the coating adhesive strength is of the order of 100 MPa. As the substrate was not approached by the probe, it can be concluded that this value corresponds more likely to an adhesive strength between HAP grains in the porous matrix, rather than to the adhesion at the coating /substrate interface.

4.9 hMSCs ONTO AEROSOL-GEL DERIVED HAP.

In the case of HAP surfaces, we observed the evolution of human hMSCs on a coating deposited from PhAc precursors and sintered at 800°C. The visualisation of the cells was performed using the same two-step procedure as for Ti based buffer layers coatings. The induced fluorescence process allowed the evaluation of the adherence of the hMSCs (figure IV.9.1). From the different experiments, it was estimated that about 65% of the seeded cells were adhered to HAP surfaces (figure IV.9.1a). The experimental procedure (thorough washing previous to cell blockage) permitted to neglect the presence of cells stuck by charge interactions. The mean cell distribution, i.e. large inter-cellular distances, suggests in a first observation a lack of cell interaction. However, higher magnification observations seem to indicate that the hMSCs exhibit a tendency to form colonies (figure IV.9.1b). It can also be observed that cell nuclei concentrate a high fluorescent activity, which does not allow the visualisation of the extra cellular matrix components of hMSCs, neither the observation of the cytoskeleton array. However, this high fluorescent activity suggests that these nuclei showed no apoptotic sign. Apoptotic cells usually present a lack of adherence and darken gradually during apoptosys. Furthermore, hMSCs on HAP surfaces showed proliferation signals since cell nuclei were systematically observed to form pairs. The arrows on figure IV.9.1b show clearly these coupled nuclei. This observation is interpreted as a final stage of the cellular division cycle confirming that the hMSCs presented intense activity while seeded on HAP. In fact, the adherence and density of hMSCs on HAP was very similar to that observed on *in-vitro* generated osteoclasts on whale dentin by using staining techniques [MCH00].

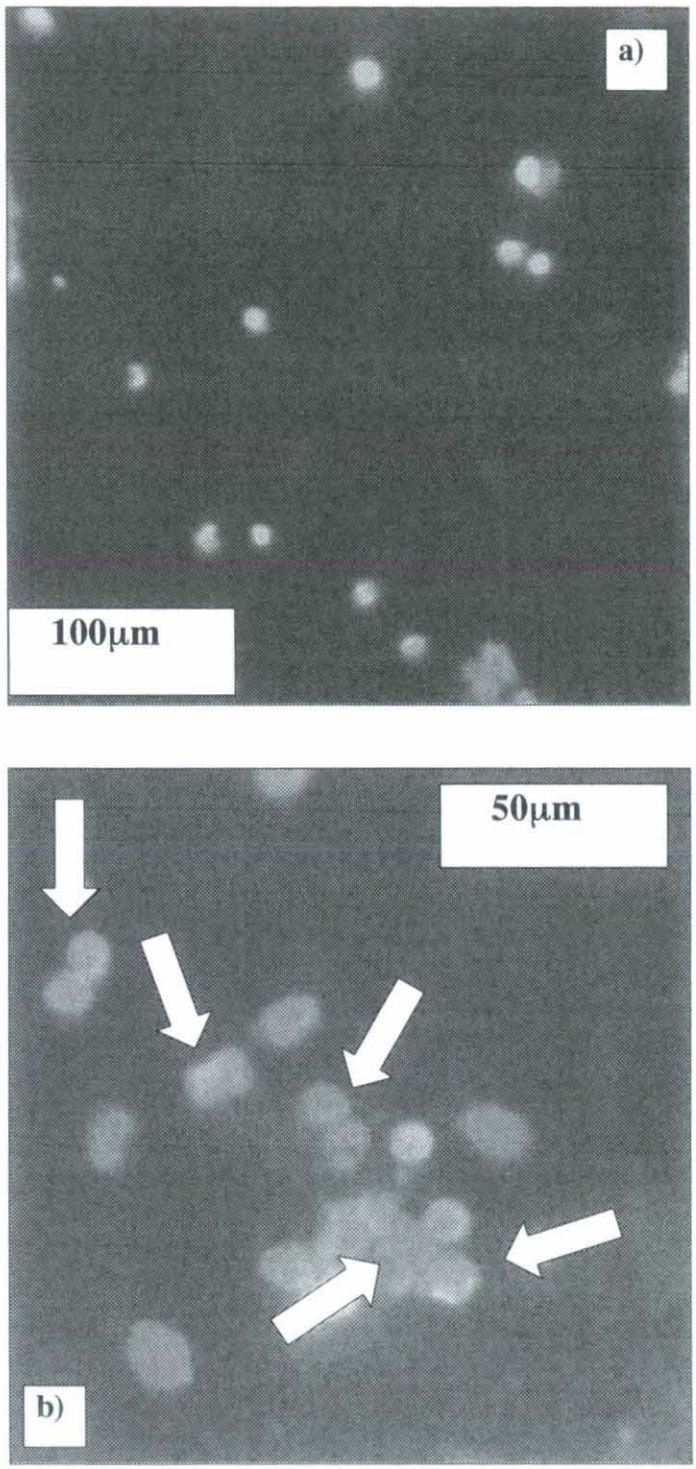

Figure IV.9.1: Fluorescence micrograph showing the behaviour of human MSCs seeded on HAP800 coatings. a) general distribution. b) proliferation evidences.

4.10 DISCUSSION: COMPARED INFLUENCE OF THE TEP AND PhAc PRECURSORS.

The calcium phosphate coatings formed by the aerosol-gel process from $Ca(NO_3)_2$ and TEP precursors have been found to present a polycrystalline structure with variable composition. CaP coatings appeared noticeably phosphorus deficient, as compared to the corresponding precursor solutions. This behaviour has been attributed to the poor sol-gel reactivity of the precursors used for this study [LIV92], associated with the very high volatility of the TEP precursor. However, we have shown that it is possible to overcome the low sol-gel reactivity of the precursors, by applying a stabilisation heat treatment at 500°C immediately after liquid deposition. The stabilisation at lower temperatures leads to an increased P deficiency rather than to a HAP structure. The system is insensitive to variations of pH or H_2O content.

The main reaction taking place during stabilisation at 500°C of the TEP precursor liquid films involves the pyrolysis of calcium and phosphorus precursors and the subsequent combustion of post-reaction species:

$$6PO_4(C_2H_5)_3 + 10Ca(NO_3)_2 + 2C_2H_5OH + 55O_2 \rightarrow$$
$$Ca_{10}(PO_4)_6(OH)_2 + 20\ NO_2 + 50H_2O + 40CO_2$$

Besides, for phosphorus rich solutions, a reaction leading to the formation of TCP becomes dominant after sintering at 800°C or higher temperatures:

$$4PO_4(C_2H_5)_3 + 6Ca(NO_3)_2 + 33O_2 \rightarrow 2Ca_3(PO_4)_2 + 12NO_2 + 30H_2O + 24CO_2$$

For the preparation of pure HAP films, the Ca/P mr of the solution can be optimised around 0.8.

We have shown that a more accurate control of the HAP stoichiometry can be achieved when using a PhAc precursor. In that case, aerosol-gel deposited

microcrystalline HAP coatings were formed, which consisted of randomly oriented crystals distributed in a porous network with a very wide pore size distribution (10 nm to 2 μm). We have established that there are three dominant parameters controlling the transformation of the precursors: the Ca/P mr, the pH and the temperature of stabilisation. Combined studies performed by FTIR and XRD allowed to fix optimal parameters: precursor sols with a Ca/P mr of 10/7, pH= 1.8, stabilisation at 500°C. The temperature increase observed during dilution of H_3PO_4 in ethanol gave evidence of the partial complexation of the phosphate groups, leading to an ethyl phosphate with 3-n free radicals which are occupied by protons in acid conditions ($(C_2H_5)_nPO_4^{-(3-n)}$, n= 1,2,3). This complex presents a higher sol-gel reactivity and a reduced volatility compared to the totally substituted TEP precursor [LIV92]. The complexation of the phosphate groups implies a nucleophile reaction of the following kind:

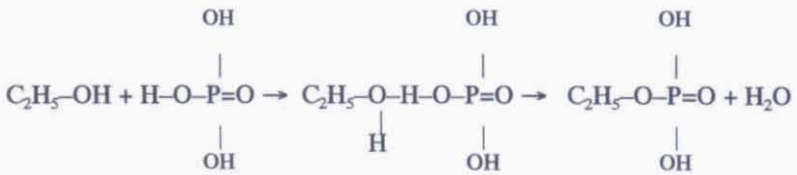

A low pH during the preparation of the precursors allows several protons to remain active during the charge exchange required for the complexation. In this conditions, OH ions were more prone to enter the HAP structure, as proved by FTIR.

The FTIR and XRD results help to understand the sequence of processes taking place during sintering at different temperatures. One of the most relevant features is the cycle of carbonate compounds produced during stabilisation. Focusing on TEP derived coatings, our study shows that, for liquid films with a calcium excess, we have to take into account the formation of CaCb according to:

$$2Ca(NO_3)_2 + 2C_2H_5OH + 5O_2 \rightarrow 2CaCO_3 + 4NO_2 + 2CO_2 + 6H_2O$$

XRD measurements confirmed that the CaCb phase is nearly extinguished for coatings sintered at 800°C and 1000°C. The location of the carbonate bands assigned to apatite and the increase in hydroxyl content with the sintering temperature are in agreement with the formation of an A type carbonated HAP [ELL94], where the

hydroxyl ions are partially replaced by carbonate ones. However, the carbonate band positions are also compatible with the formation of a B type apatite, where carbonate groups replace phosphate ones in the structure.

Furthermore, it has been established from FTIR and XRD results that, the lower the Ca/P mr of the precursor solution, the weaker the carbonate stabilisation in the coating, and the weaker the CaO content after calcination at 800°C.

Besides, the remaining presence of the carbonate IR band at 1455 cm^{-1} proves again the inclusion of carbonate in the apatite structure, which proves that an A and B type carbonated HAP is also formed from PhAc precursors [ELL94]. However, the presence of carbonate ions integrated in HAP structure was observed to diminish for increasing sintering temperature.

In the case of PhAc precursors, the formation of CaCb is due to the presence of ethyl radicals and to a slight excess of calcium in the liquid films. Thus the CaCb formation can be accounted for by the following reaction:

$$Ca(NO_3)_2 + (C_2H_5)_nPO_4^{n-3} + O_2 \rightarrow nCaCO_3 + NO_2 + nCO_2 + H_2O + PO_4^{n-3}$$

This reaction implies that the use of H_3PO_4 precursors reduces the formation of carbonate in comparison with $(C_2H_5)_3PO_4$ precursors at equivalent Ca/P mr. A comparison of the FTIR experimental results between TEP and PhAc coatings confirms this feature. In the case of TEP precursors, we could observe an increase in intensity of the OH bands for raising temperatures due to a rehydroxylation of the structure. This phenomenon was not observed for PhAc derived HAP coatings maybe due to the lower integration of CO_3 in the HAP structure occupying OH sites.

4.10 SUMMARY AND CONCLUSIONS.

It has been established that the aerosol-gel formation of calcium phosphate coatings with tailored composition is controlled by the precursor solution composition

and depends strongly on the processing temperature. It was found that, irrespectively of the precursor used, the solution must be rich in P precursor to compensate its low sol-gel reactivity during the processing of the coating. Only PhAc precursors showed a tendency to nucleophile substitution reactions during sol preparation. It has been shown that, after sintering at 500ºC, the coatings present a polycrystalline structure irrespective of the precursor used in the solution. A HAP phase is always obtained with the frequent presence of satellite phases. The nature and amount of the satellite phases are strongly influenced by the Ca/P mr of the solution, by the sintering temperature and by the precursor used. Both, TEP and PhAc precursors lead to adherent and reasonably pure HAP coatings.

Auger spectra measured for TEP derived CaP coatings deposited on TiAlV alloys confirmed a reasonable agreement with the composition of the HAP standard. Only slight deviations were detected, which implies a weak Ca overstoichiometry. This slight Ca enrichment, accompanied by an increase in oxygen content, is compatible with the presence of a CaO phase as detected in the XRD diagrams for a high temperature sintering. It is not excluded as well that the intensity of the O_{KLL} transition is influenced by the carbonate presence (revealed by FTIR).

Concerning morphologic features, it has been shown that the coatings present high specific surface areas independently of the precursors used. Besides, SEM observations showed that the sintering temperature should not exceed 800°C, as thermal stresses, induced by the different expansion coefficients at the film-substrate interface, provoke intense cracking of the coatings.

The adhesive strength of CP-80-800 coatings deposited on TiAlV was measured by means of indentation techniques. The adhesive strength was found to be in the order of 100 MPa, which is significantly higher than the value obtained for equivalent HAP coatings deposited on TiAlV alloys by dip-coating [WEN99, MAV00]. This difference may however be partially influenced by the local effects due to our indentation measurement method, which is not totally comparable with glue adhesive strength tests used in the previously referenced reports. In fact, our values correspond strictly to an

adhesive strength between compact HAP grains rather than to the coating substrate interface.

It is worth emphasising that PhAc presents a double advantage with respect to TEP precursors. On one hand, the higher reactivity of PhAc allows a better control of the coating composition and on the other, it reduces the formation of CaCb and subsequent CaO satellite phases. Polycrystalline films of high purity could be obtained after sintering PhAc derived films at 650ºC. Thus, the whole preparation process was carried out at temperatures lower than the temperature applied for the recrystallization of plasma sprayed HAP coatings [HUA92]. This treatment ensures that no detrimental transformation affects the metallic substrate. This is specially attractive for the processing of HAP coatings onto TiAlV alloys, since the mechanical response of TiAlV can easily be affected at high temperatures [LON98].

Finally, pluripotent hMSCs seeded onto HAP surfaces were demonstrated to show adherence and activity, which not only supports the notion of biocompatibility but also demonstrates the enhanced *in-vitro* bioactivity of aerosol-gel HAP coatings. This behaviour is of great significance since it simulates a surface-induced multi-step cell cycle occurring in the tissue environment.

To conclude, an important advantage derived from the aerosol-gel processing is that the system lends itself to the deposition on large and three-dimensional substrates [LAN91], which is essential for the processing of plates, screws and elements of complex design such as hip-joint prostheses.

CHAPTER V: *BIOCOMPATIBLE STRUCTURES.*

CHAPTER V: *BIOCOMPATIBLE STRUCTURES.*

5.1 INTRODUCTION.

In this chapter we analyse several physicochemical aspects of multilayer coatings prepared as functional biocompatible structures. On one side, the HAP/TiO_2 or HAP/TiN configuration exploits the advantages of an outer bioactive ceramic and on the other the stability of an intermediate Ti based coating over the metallic alloy implant (see chapter I). This analysis includes microstructural features at the interface between the two coatings analysed by TEM, the composition along the interface studied by AES and RBS and a presentation of the surface morphology of the HAP coatings. The coatings have been preferentially prepared on Si wafers to exploit the advantages of this substrate for the preparation of TEM cross section samples (see Annex I) and the RBS analysis (lighter substrate element). In the case of AES, the structures have been prepared onto TiAlV substrates, thus reducing possible chemical shifts due to a poorly conducting substrate. The advantages of preparing HAP coatings from PhAc precursors, rather than by using TEP precursors, have been outlined in the previous chapter. Accordingly, the HAP coatings presented herein have been prepared from PhAc precursors.

5.2 HAP/TiO_2 AND HAP/TiN STRUCTURES.

5.2.1 Microstructure of HAP/TiN and HAP/TiO_2 multilayers.

HAP coatings prepared from PhAc precursors were reproduced onto TiN/Si(100) and TiO_2/Si(100) substrates. Figure V.2.1 shows the XRD diagrams corresponding to the HAP coatings annealed at 800ºC. This diagrams show the same features than HAP800 coatings described in the previous chapter. Basically, a polycrystalline coating mainly formed of HAP is obtained. A CaO phase could also be detected, specially in the HAP coating grown onto TiO_2 (figure V.2.1a). This diagram shows also a slight TiO_2 peak at 25.3º (anatase), produced by the interlayer material. Conversely, the HAP/TiN diagram does not show the peaks of the TiN osbornite phase but the anatase TiO_2 phase

appeared clearly in the diagram (figure V.2.1b). This indicates that HAP sintering at 800°C in air drastically induces the TiN oxidation. Besides, these results confirm the already mentioned reproducibility in the formation of HAP coatings from PhAc precursors.

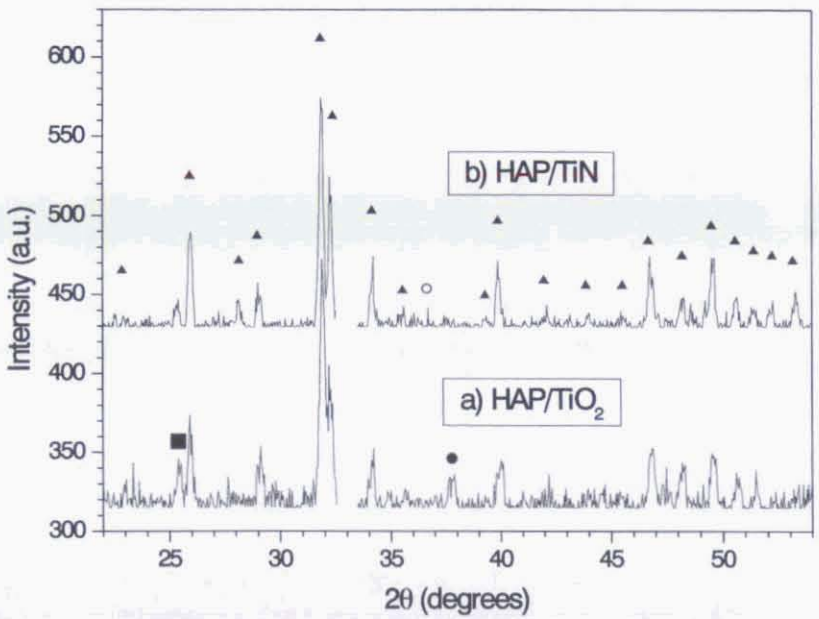

Figure V.2.1: XRD patterns of a) a HAP/TiO_2/Si structure and b) a HAP/TiN/Si structure after sintering at 800°C. ▲: HAP, O: TiN, ■: TiO_2, ●: CaO. The (100) Si wafer contribution around 33° has been removed

Cross section observations performed by TEM for an HAP/TiN coating allowed to study relevant aspects concerning the microstructure at the HAP/TiN interface. Figure V.2.2 shows the general view of a HAP/TiN/Si structure obtained after sintering at 800°C in air. The interface between HAP and TiN is clearly determined by denser structures that produce a higher contrast region. Furthermore, these structures do not present random shapes and orientations, but well defined rectangular forms mainly assembled with their largest facet over the HAP/TiN interface. It is also remarkable that no crack can be observed in the high contrast region.

The observation at higher magnifications (Figure V.2.3) revealed the structure of these interfacial crystals. The high resolution image in figure V.2.3a shows one of these structures with the crystalline planes clearly piled on one single-direction.

The interplanar distance (3.44 Å) allowed to identify the (002) planes corresponding to the HAP structure and are coincident with half the **c** parameter of the hexagonal HAP lattice. However, several arrangement faults were also detected in this crystalline assembling, as shown in the high resolution image presented in figure V.2.3b. In this figure, (002) planes showing a different orientation with respect to the substrate can be observed.

This observation of different orientations is an indication of a growth mechanism activated during sintering since we have shown that the stabilisation of the coating induces a rapid crystallization on random directions. We have not been able to relate the nature of the substrate with this preferential growth, at least in terms of epitaxial relations. The initial TiN interlayer was reported to present a preferential growth along the (111) direction (Chapter III). However, we have shown that this structure is oxidised during sintering. Thus, the formation of a textured TiO_2 anatase phase is the most plausible transformation of the TiN buffer layer as deduced from the XRD diagrams of figure V.2.1. As a confirmation of this interpretation, the potentiality of atmospheric O for replacing N in the TiN structure (and generally for metal nitrides) is a well documented phenomenon. It has been previously reported that oxygen substitution into TiN leads to anatase at similar temperatures to those used in this work [MIT98]. Moreover, textured (001) anatase films are obtained by replacing N_2 by O_2 during pulsed laser deposition of TiN [MAJ99]. This oxidation is strengthened when an oxide layer is deposited over the TiN coating. Accordingly, the study of our HAP/TiN coating showed that the oxidation of the TiN layer was favoured by the presence of the HAP coating, due to diffusion of oxygen through the HAP/TiN interface.

In any case, the nearest neighbour distances for these (001) oriented tetragonal TiO_2 crystals is much smaller than the nearest neighbour distance for (002) oriented

HAP crystals. This behaviour suggested that the growth orientation might be induced by interdiffusion mechanisms.

Concerning the presence of crystal faults, it is also plausible that crystals, initially out of the interface domain, impose their orientation during sintering to other structures placed at the interface.

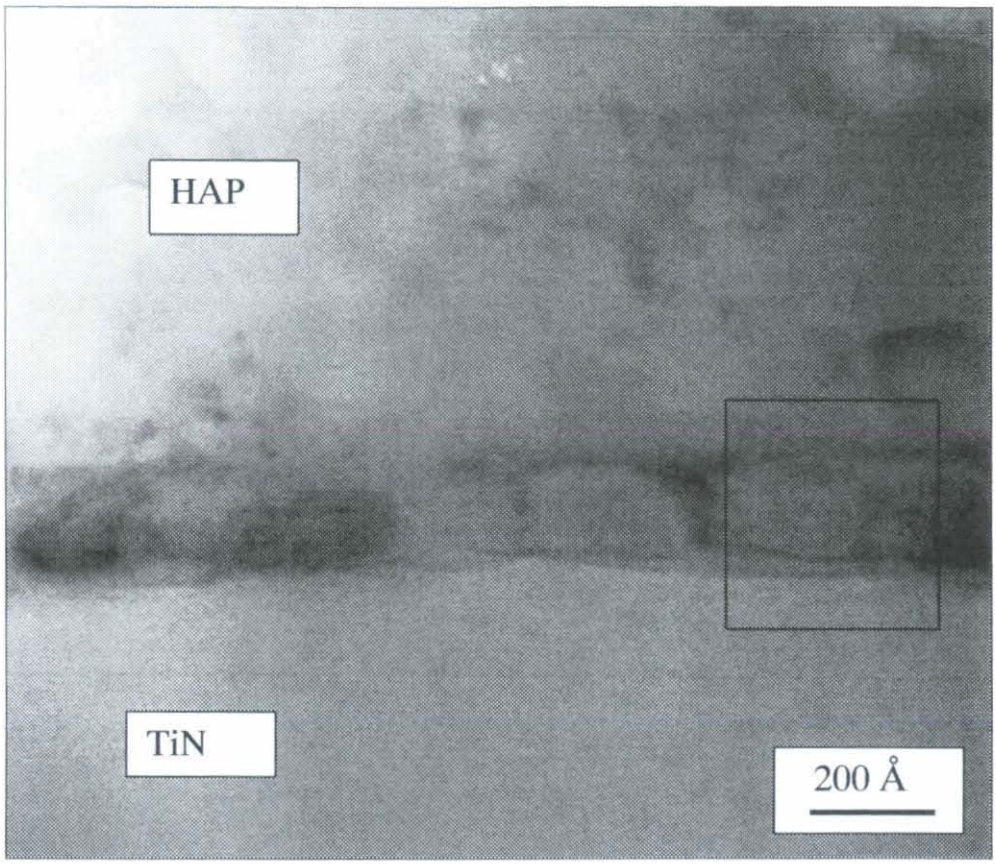

Figure V.2.2: General view of a HAP/TiN/Si structure obtained after sintering in air at 800°C.

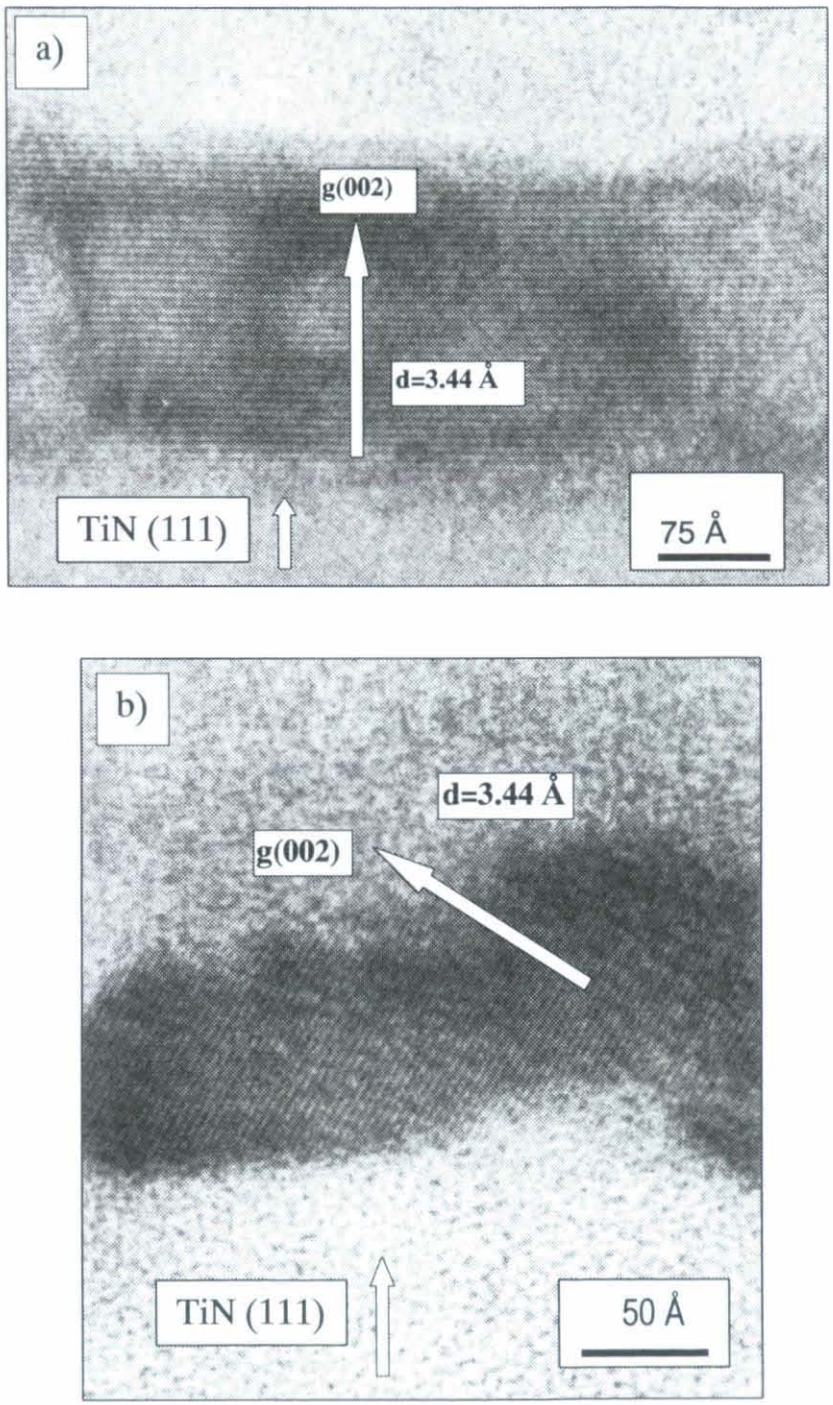

Figure V.2.3: High resolution images of the HAP crystals observed at the HAP/TiN interface. a) conventional arrangement along (002) planes and b) arrangement fault.

5.2.2 Surface and interface composition.

The RBS spectrum of a HAP650 coating deposited onto TiO_2/Si and its corresponding simulation by means of the Rump program [DOO85] are presented in figure IV.2.4 (dotted and continuous lines, respectively). The simulation of RBS spectra was performed by assuming that the coating is composed of adjacent single layers of limited thickness, taking into account the scattering factor of each element. The composition of the layer was varied from the surface material to the substrate in order to correctly reproduce the backscattering spectrum. The analysis of the experimental data (dotted line in figure IV.2.4) could be simulated by using a single-layer model (continuous line), i.e. a model which accounted for a homogeneous HAP layer.

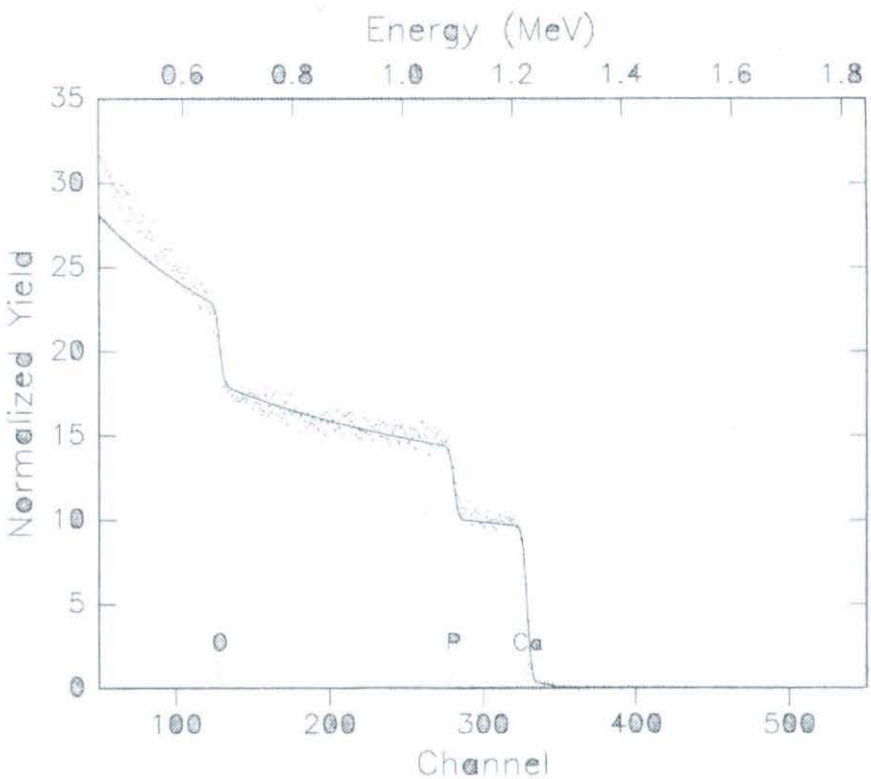

Figure V.2.4: RBS spectrum of an HAP/TiO_2 coating after sintering at 650°C (dotted line) and its simulation (straight line): HAP layer thickness: 10000.10^{15} at/cm^2 and apparent stoichiometry: $Ca_9P_7O_{26}H_2$.

However, the composition of the modelised HAP layer was found to be calcium deficient (Ca/P mr= 1.3) with respect to stoichiometric HAP, which contradicts RBS

and EDX results presented in chapter IV. In order to explain this discrepancy, we must state that RBS analysis introduces higher errors in the stoichiometry estimation of light elements. We outline that the roughness of the films can also affect the measurement and cause arbitrary compositional gradients. Thus, the analysis of the surface by SFM must be taken into account. In order to illustrate this possible influence, Figure IV.2.5a shows the relevant surface roughness of an HAP layer scanned over areas of 200x200 nm^2. The $^4He^+$ beam interacting with such a surface is inhomogeneously scattered. The scheme presented in figure IV.2.5b shows that $^4He^+$ particles will travel different real paths along rough surfaces (top), but almost the same paths for flat surfaces. In this way, particles backscattered at identical depths will be detected with different energies. Thus, the spectra obtained for very homogeneous films exhibit well defined vertical components. The surface roughness produces instead a branch of energies that induces softer gradients in the spectra.

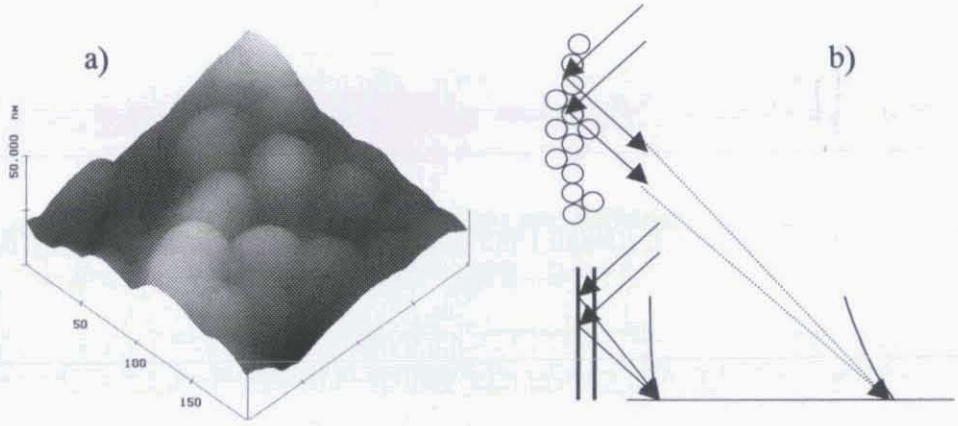

Figure V.2.5: a) SFM image of a HAP coating grown onto TiO_2 at 500ºC. b) Schematic representation of the effect of the surface topography on the RBS spectra.

It appears thus more realistic to rely on XRD and EDX results, supporting that the whole stoichiometry of the coating should be only slightly Ca rich (Ca/P mr≥ 1.67). In spite of the discrepancies in the stoichiometry determination, RBS spectra have been also obtained from HAP coatings deposited onto TiN and Si allowing a comparison of the relative stoichiometry of the three different interfaces. It allows also an inspection of the stoichiometry of chemically etched samples relative to non etched samples.

In order to check the composition in the HAP coating at the HAP/TiN or HAP/TiO_2 interface, we intended to compare the spectrum of figure V.2.4. with the one of the same coating after chemically etching the HAP outer layer with HAc. However, it was consistently observed that the Ca and P signals (after chemically etching the HAP coatings stabilised at 500ºC or sintered at higher temperatures) remained too intense to extract any information from the interface region. This is considered as a new evidence of the high adhesion strength in the HAP/TiN interfacial region. In order to reach the interface, coatings produced by stabilization at only 300ºC without further sintering were also etched. The RBS spectrum from the HAP300 coating and the corresponding simulation are both depicted in figure V.2.6.

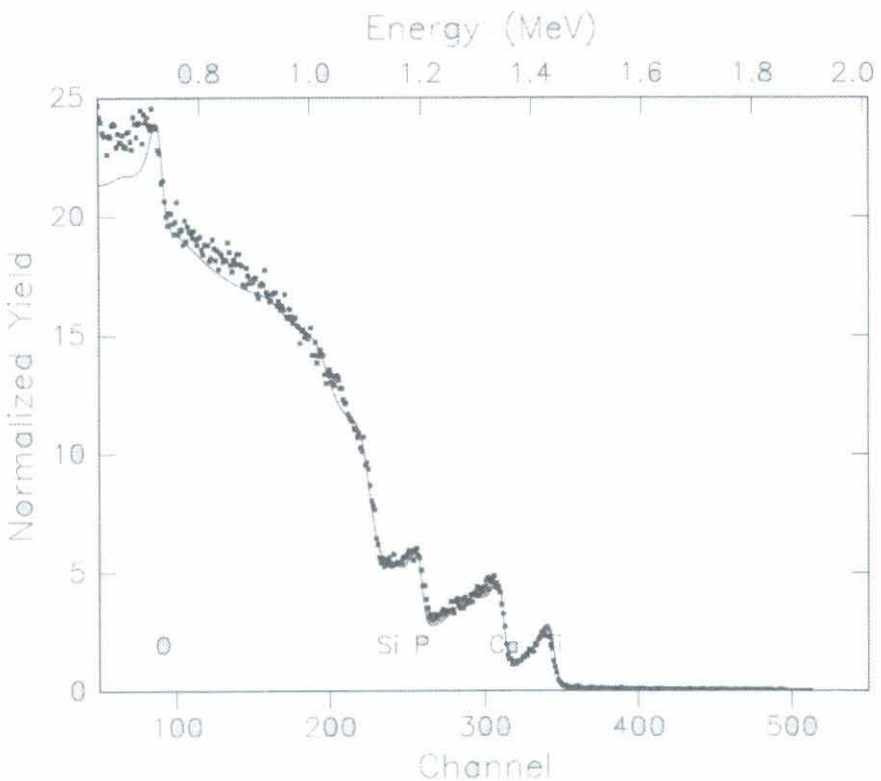

Figure V.2.6: RBS spectrum of an HAP/TiO_2 stabilised at 300ºC and chemically etched in HAc (dotted line) and its corresponding simulation (straight line): the layer thickness and apparent stoichiometry from the outer layer (L1) to the substrate (L6) are: L1 400.10^{15} at/cm^2 $Ca_5P_8O_{36}H_2Si_{0.5}Ti_{3.5}$. L2 800.10^{15} at/cm^2 $Ca_{4.5}P_7O_{16}H_2Si_{20}Ti_{1.2}$. L3 800.10^{15} at/cm^2 $Ca_9P_{12}O_{14}H_2Si_{100}Ti_1$. L4 800.10^{15} at/cm^2 $Ca_{10}P_{13}O_5H_2Si_{200}Ti_1$. L5 800.10^{15} at/cm^2 $Ca_8P_{10}O_5H_2Si_{250}Ti_1$. L6 5000.10^{15} at/cm^2 Si.

It is concluded that, at a temperature as low as 300°C, a HAP structure intimately grows over the TiO_2 surface and remains at the interface even after chemical etching. The simulation, based on a 5 layers configuration, shows that the composition of the etched coating is also calcium deficient with respect to HAP. The effect of the surface roughness is in this case even more pronounced, inducing quite soft composition gradients in the spectrum.

These features were confirmed by the analysis of analogous HAP/TiN coatings and those HAP coatings deposited onto bare Si (100) substrates. The stoichiometry of the bulk HAP coating deposited onto TiN and sintered at 650°C was found to be 1.2, a value close to the Ca/P mr deduced for HAP/TiO_2 structures before etching. This spectrum and its corresponding simulation are presented in figure V.2.7. The thickness of the outer HAP layer was high enough as to avoid the detection of the underlying TiN buffer layer.

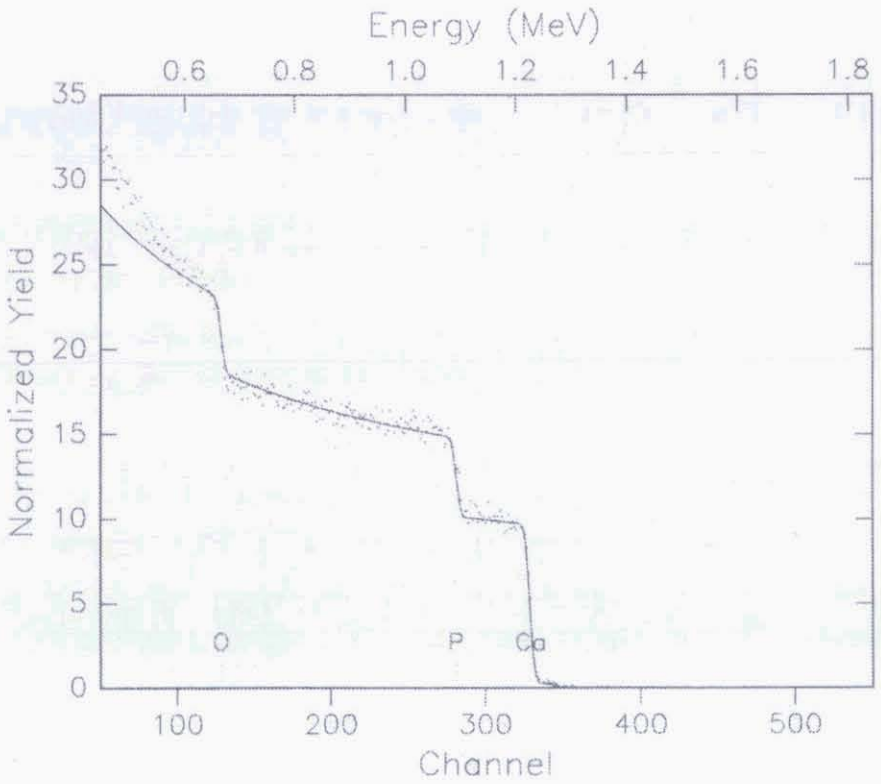

Figure V.2.7: RBS spectrum of a HAP/TiN structure stabilised at 500°C and sintered at 650°C (dotted line) and its corresponding simulation (straight line): the layer thickness and apparent stoichiometry from the HAP layer are: 10000.10^{15} at/cm^2, $Ca_{9.5}P_8O_{26}H_2$.

The TiN interlayer contribution was drastically increased after etching. The TiN buffer layer was somehow thicker than the equivalent TiO_2 film of the HAP/TiO_2 structure. This can be deduced from the higher intensity of the Ca and P signals in the spectra presented in figure V.2.8, which is artificially produced by a background associated to the thicker TiN layer. The spectrum corresponding to a chemically etched film deposited on Si is also presented in figure V.2.8 to provide a reference of a spectrum without Ti contribution.

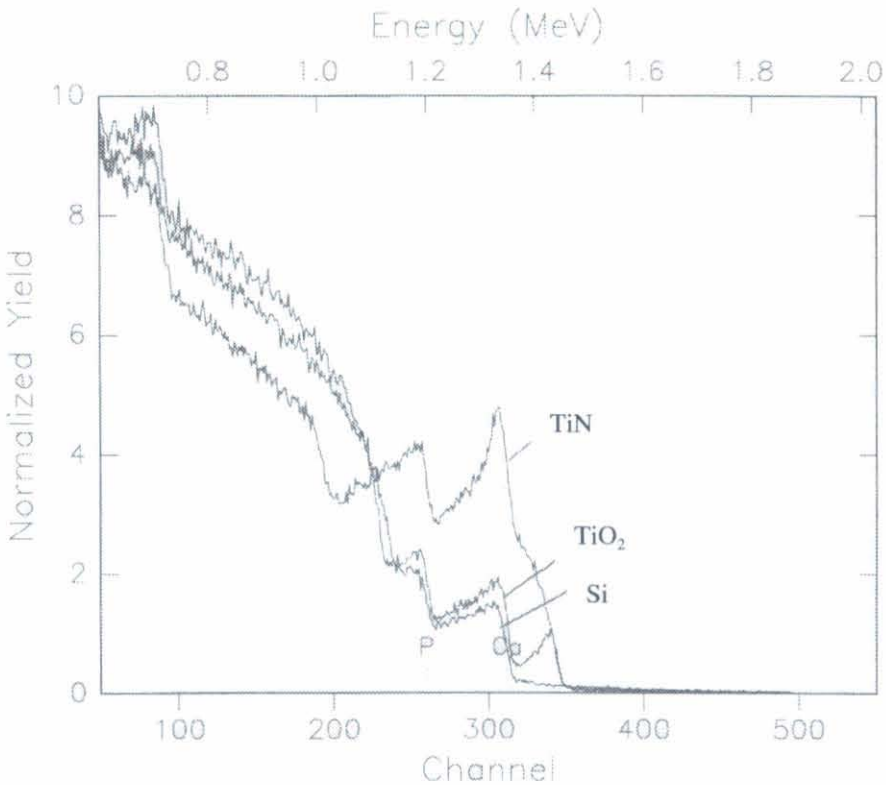

Figure V.2.8: RBS spectra of an HAP/TiN structure stabilised at 300ºC and chemically etched in HAc compared with those of etched HAP/TiO_2 and HAP/Si coatings.

Finally, we have to outline that the appearance and properties of the aerosol-gel deposited HAP structures were, in a first approximation, independent of the substrate used. In other words, aerosol-gel deposition and sintering parameters are dominant over the nature of the substrate. The Ca/P mr of the HAP structures remaining over the Si substrate after chemical etching (100 nm thick interfacial layer from a 5 layer

configuration) was found to be very similar to the value obtained for both HAP/TiO_2 and HAP/TiN structures (figure V.2.9).

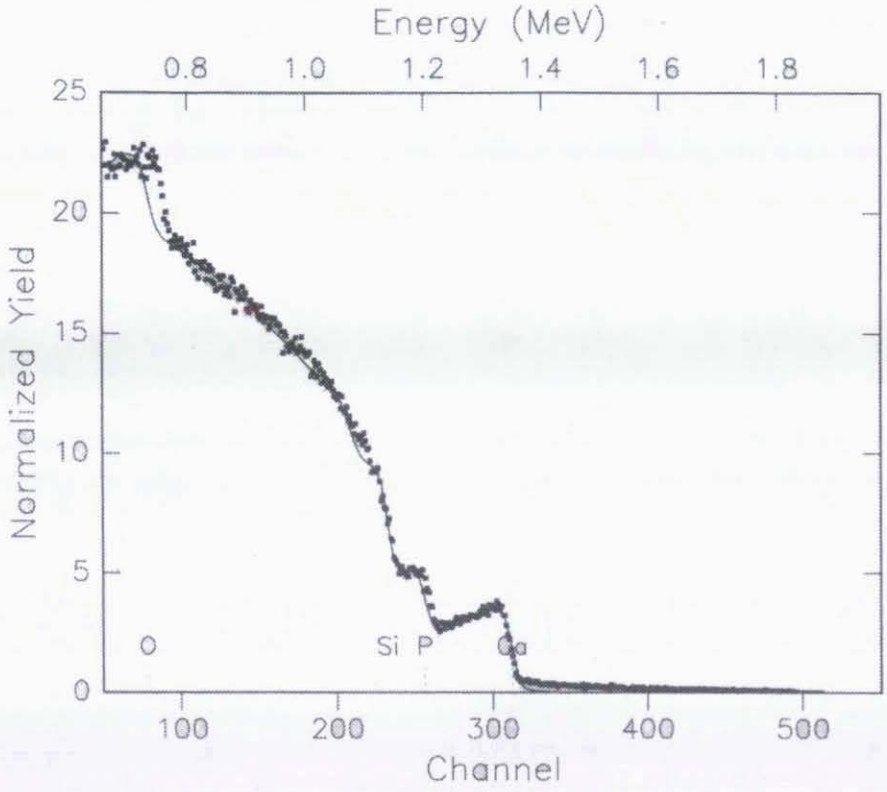

Figure V.2.9: RBS spectra from an HAP/Si coating stabilised at 300°C and chemically etched in HAc (dotted line) and its corresponding simulation (straight line): the layer thickness and apparent stoichiometry from the outer layer (L1) to the substrate (L6) are: L1 800. 10^{15} at/cm^2 $Ca_{3.2}P_{5.2}O_{16}H_2Si_{11}$. L2 800. 10^{15} at/cm^2 $Ca_{3.5}P_4O_{10}H_2Si_{26}$. L3 800. 10^{15} at/cm^2 $Ca_{3.5}P_4O_{10}H_2Si_{52}$. L4 800. 10^{15} at/cm^2 $Ca_{3.5}P_4O_{14}H_2Si_{85}$. L5 800. 10^{15} at/cm^2 $Ca_{3.5}P_4O_{14}H_2Si_{200}$. L6 5000. 10^{15} at/cm^2 Si.

5.2.3 AES depth profiling.

In order to complete the in-depth study of our HAP/TiN and HAP/TiO_2 coatings, we took advantage of the in-depth profiling capability of AES. Spectra were periodically recorded during Ar^+ ion etching. As already mentioned in chapter IV, in order to avoid too long etching times, HAP/TiO_2 and HAP/TiN coatings deposited onto TiAlV alloys and sintered at 500°C were previously etched with acetic acid prior to AES analysis.

A) HAP/TiN structures.

The AES spectra of a HAP/TiN structure, after Ar^+ etching for 10, 20, 30 and 40 min, are presented in figure V.2.10. As already reported in chapter IV for HAP/TiAlV coatings, the presence of split bands in the P_{LMM} transition is evident. These split bands have been previously described for HAP preparations [ONG98] but are not reported for GaP semiconductor structures [DAV76].

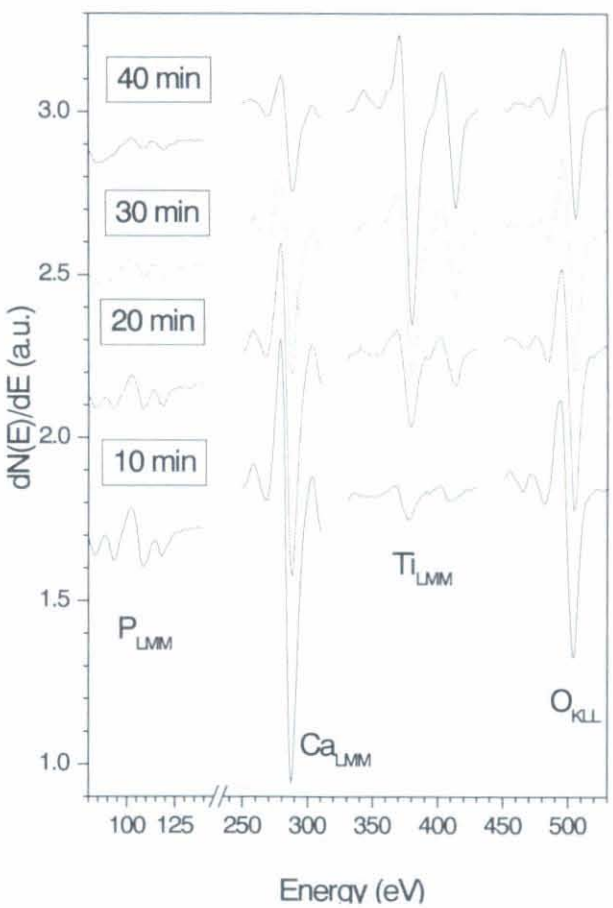

Figure V.2.10: Auger spectra of a HAP/TiN structure after sintering at 500ºC chemical etching and Ar^+ sputtering during 10, 20, 30 and 40 min.

For our samples, the pronounced surface morphology of the coatings caused several difficulties in the analysis of the spectra (i.e. rough structures produce mixed signals with different depth origins), which caused a loss in the depth resolution.

However, the presence of two relevant minima at 109 and 119 eV in the P_{LMM} transition are clearly observed in the different spectra of figure V.2.10. These transitions are accompanied by several weaker ones. The P split contributions derive from a nominal band at 120 eV [DAV76]. The one at higher energies was observed to diminish only slightly in intensity for increasing sputtering times, while the one at lower energies presents a remarkable decay. The similarity between these split bands and the one observed for an HAP/TiAlV coating (chapter IV) suggests that the splitting originates from a same mechanism for both samples.

Two minima at 379 and 414 eV in the Ti_{LMM} transition of our sample evidence also a chemical shift from the nominal values of 387 and 418 eV measured for pure Ti [DAV76]. This is partly attributed to the oxidation of the originally nitrided Ti interlayer. This feature is outlined by the presence of a transition point at 395 eV, which forms a minimum at short etching times (10 and 20 min) but only a deflection after longer ion etching times (30 and 40 min). The AES spectra evolution can be interpreted in terms of Ti atoms in a different chemical state. For longer etching times, electrons from a Ti-N (non oxidised TiN still remaining in deeper layers) or a Ti-Ti environment (TiAlV alloy substrate) are responsible for producing wider transitions that hide the intermediate Ti-O transition at 395 eV.

These general features were explored through in-depth profiles determination. The in-depth concentration profiles were obtained by recording AES spectra every 5 minutes for a total etching time of 360 min. Figure V.2.11 shows the compositional profiles of the elements detected in the sample. For each curve, the depth increment is about 40Å, i.e. in good agreement with the estimated in-depth resolution. The initial increase in the signal from the Ca_{LMM} and P_{LMM} transitions can be ascribed to artifacts related to a passivating carbon layer due to the atmospheric exposure. In this figure the evolution of the intensity from the Ti_{LMM} (Ti1= 379 eV, Ti2= 414 eV) and the split P_{LMM} (P1= 109 eV, P2= 119 eV) lines are presented independently.

Concerning Ti transitions, both the Ti1 and Ti2 peaks were observed to increase in intensity for increasing etching times. As previously mentioned, this is consistent

with a progressive exposure of the underlying TiN/TiAlV substrate. The evolution of the concentration in deeper locations shows that both contributions almost reach a plateau. This proves that, for the longest etching times, the outlying HAP coating was almost removed as well as the major part of the oxidised surface layer of the TiN coating, which produced an almost steady state signal.

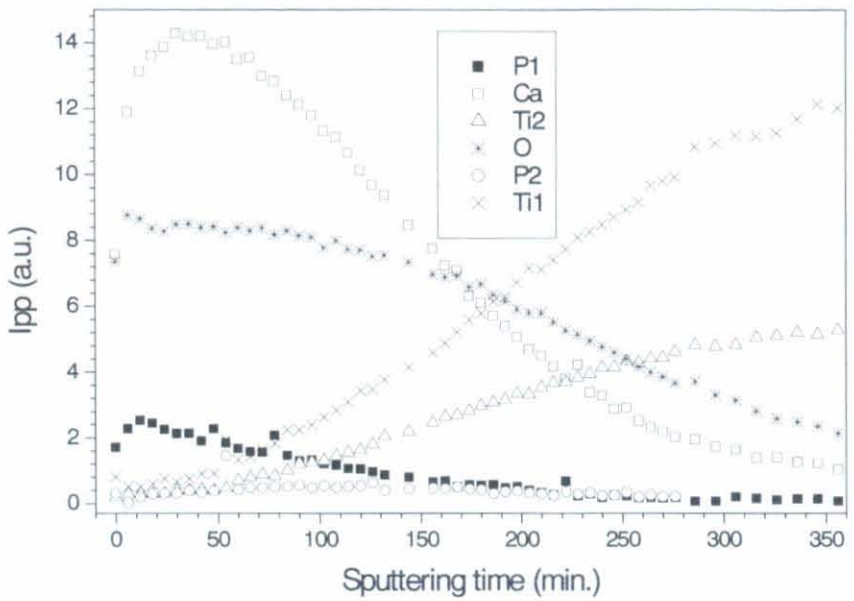

Figure V.2.11: AES In-depth compositional profiles of a HAP/TiN structure sintered at 500ºC and chemically etched with acetic acid. For each point, the depth increment is about 40Å.

The in-depth evolution of the P1 and P2 peaks can be interpreted in terms of Ar^+ beam modification. The AES analysis of ion beam sputtered HAP coatings has been previously reported to reveal the presence of a double chemical environment, i.e. a phosphide and a lower energy phosphate environment [RAE84, ONG98]. A chemical shift, from a reduced to an oxidised state, has been also reported for the high energy P transition, from 1863 eV to 1849 eV, respectively. The P1 and P2 in-depth profiles of our sample are magnified in figure V.2.12. The P1 peak might be attributed to P atoms in the HAP structure, since it corresponds to a lower energy component. This is in accordance with the energy interpretation of the AES spectra for the PO_4 tetrahedra in HAP [RAE84]. When Ar^+ etching proceeds, the intensity of this peak is observed to

continuously diminish until a nearly zero intensity is reached. The remnant signal is plausibly due to the rough surface morphology. Note that this behaviour is consistent with the detection of a remnant Ca component for longer sputtering times. Alternatively, these remnant signals could arise from the presence of diffused Ca and P atoms in the TiN layer. The temperature dependence of such a diffusion process has been previously studied for HAP coatings deposited by pulsed laser deposition on Ti substrates. The AES depth profiles evidenced the activation of the diffusion at increasing temperatures [TOR93].

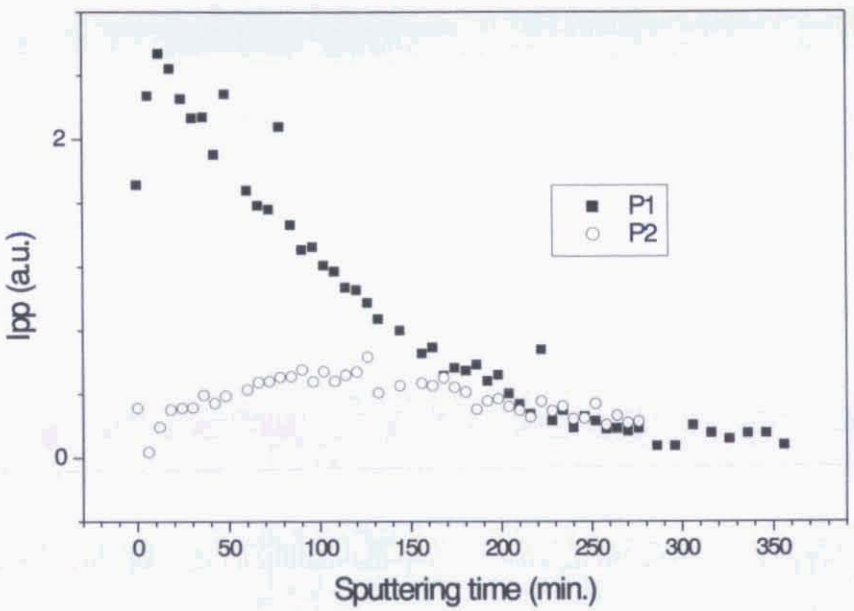

Figure V.2.12: AES in-depth compositional profiles. Magnification of the P1 and P2 peaks.

Concerning the P2 peak behaviour, it slightly increases during the first 100 min of sputtering, does not vary significantly for the subsequent 60 min, and finally decreases in intensity for longer sputtering times. This profile is consistent with the reduction of P atoms due to electron beam modifications. Additionally, the Ar^+ beam interaction induces a preferential sputtering of O resulting in the presence of free P. The intensity initially raises as a consequence of the increasing exposure of the HAP crystals to the Ar^+ beam. Then, the signal is stabilised when the thickness of the layer becomes comparable to the penetration depth of Ar^+ damage. Finally, when the interface with the

TiN interlayer is reached, the signal diminishes, due to the progressive elimination of the HAP layer.

The aforementioned possibility of P (or Ca) diffusion in the TiN interlayer might be supported by the in-depth oxygen composition. An oxygen diffusion process is evidenced since the intensity decay of the O peak is not related to the behaviour of the Ca and P peaks (figure V.2.11). This would be the expected behaviour if the O signal could be only ascribed to the presence of oxygen in the HAP coating, i.e. no oxygen diffusion in the TiN interlayer. Actually, the oxygen peak follows a much slower decay than the P1 and Ca peaks and remains clearly detectable for longer sputtering times, which evidences a diffusion process. Oxygen diffusion is of course responsible for the TiN to anatase partial transformation, as depicted by XRD, and could in turn favour the diffusion of other atoms, i.e. P or Ca.

In order to numerically illustrate these features, the concentration profile of the O component has been fitted in figure V.2.13 to a complementary error function (erfc). This analytical curve is solution to the Fick's diffusion equation in the one dimensional approximation:

$$\frac{dN(x,t)}{dt} = D(T)\frac{d^2N(x,t)}{dx^2}$$

where N is the concentration of the diffusion element and D is the temperature dependent diffusion coefficient (indicator of the ability of an atom to diffuse in a certain system). We have estimated a constant interface composition (N_o) between the two adjacent materials since the presence of a HAP coating over the HAP/TiN interface can be considered as an infinite source of atoms. If we consider a time t_o, the complementary error function gives the following solution to the concentration profile [GLA79]:

$$N(x,t_o) = N_o\left(1 - \frac{2}{\sqrt{\pi}}\int_0^{x/2\sqrt{Dt_o}} e^{-\alpha^2} d\alpha\right)$$

It is evident from figure V.2.13 that the experimental oxygen profile can be satisfactorily fitted to this equation. This fit shows that an estimation of the oxygen diffusion coefficient (D) could be deduced if similar analysis were repeated for lower temperatures. However, the experimental limitations in the preparation of the HAP coatings (i.e. the coating dependence with temperature of stabilisation) have limited this possibility.

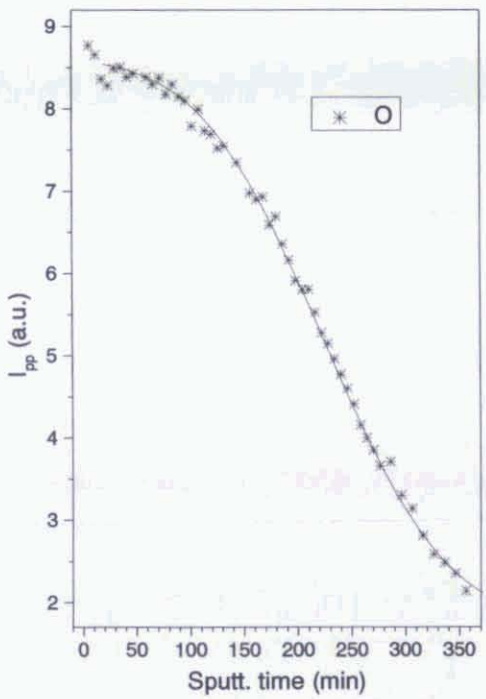

Figure V.2.13: Concentration profiles of O and its corresponding erfc fit.

B) HAP/TiO_2 structures.

The AES depth profiles performed on a HAP/TiO_2 coating (figure V.2.14) show that the thickness of the HAP coating, after chemical etching in acetic acic, is smaller than the etched HAP thickness corresponding to the previously studied HAP/TiN coating. In figure V.2.14, the overall contribution of the P1 and P2 components has been plotted. After 20 min of Ar^+ sputtering, the behaviour of the Ti and O signals show that the TiO_2 interface is intensively exposed to the electron beam with a low signal from the HAP outer layer. The concentration profile of oxygen shows that the stoichiometry of the TiO_2 interlayer remained stable during the preparation of the HAP coating. This is

deduced from the concentration plateau observed for the subsequent 80 min of sputtering (150 nm depth approximately). However, the slow decay and remnant detection of the O peak for longer etching times suggest that oxygen diffusion affects the TiAlV substrate.

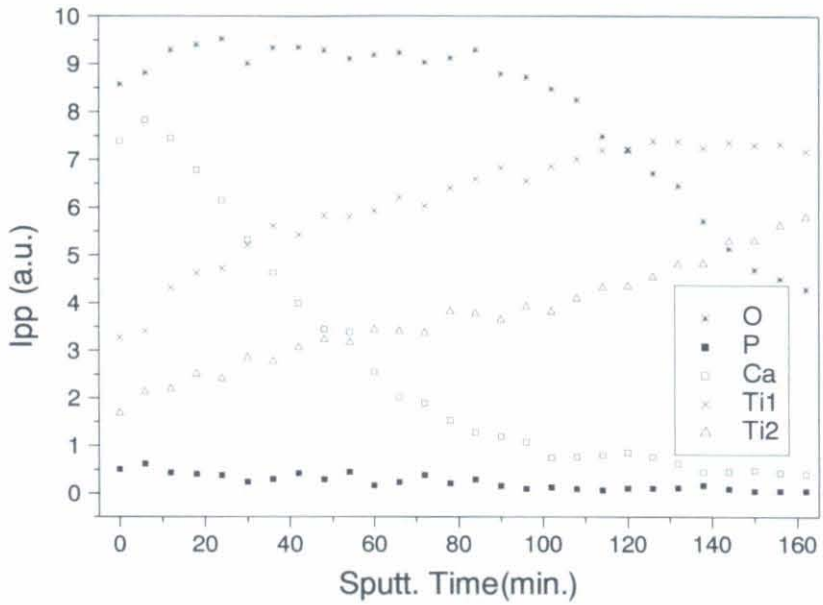

Figure V.2.14: AES in-depth profiles of a HAP/TiO_2 structure after sintering the HAP layer at 500ºC and chemical etching in acetic acid.

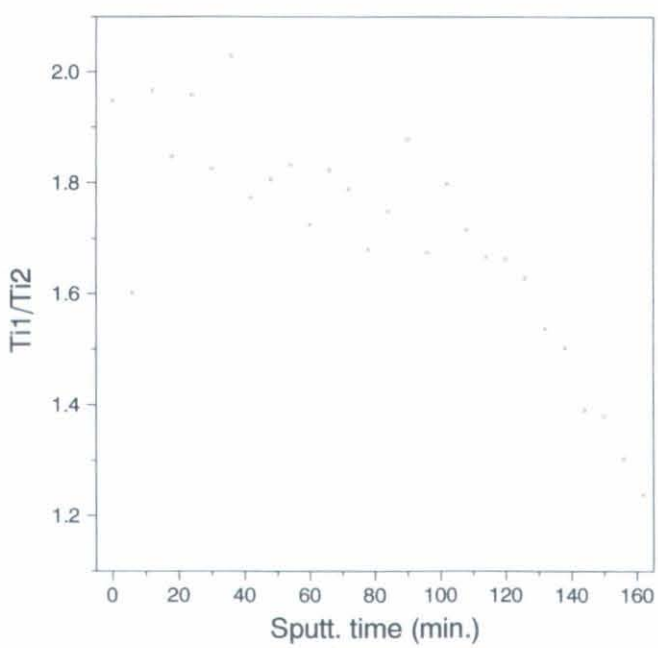

Figure V.2.15: AES evolution of the Ti1/Ti2 ratio corresponding to the depth profiles of an HAP/TiO_2 structure.

The behaviour of the Ti1 and Ti2 transitions further illustrate this feature. The evolution of the T1/T2 intensity ratio, illustrated in figure V.2.15, is particularly helpful to study the changes in the chemical environment of the Ti atoms. The ratio is approximately 1.4 for a TiO_2 structure and 0.7 for a Ti metallic surface [MAT77]. This ratio has also been reported to follow a similar evolution from 1.2 for $Ti_{0.75}O_{0.25}$ to 0.95 for a nearly pure Ti (O<5%) [FER01]. This suggests that the slow continuous decay of the Ti1/Ti2 ratio illustrated in figure V.2.15 (not completed after 160 min etching) is influenced by the in-depth distribution of oxygen into the TiAlV substrate.

5.2.4 Morphology of the HAP outlayer.

The SFM study of HAP/TiN and HAP/TiO_2 coatings has allowed a comparison with the morphology of HAP coatings grown on Si substrates. Furthermore, it has allowed to make a morphological interpretation of the surface effects produced by chemical etching.

First of all, this exploration provided a new evidence of the surface roughness of the HAP coatings. However, due to roughness effects, the tip of the microscope suffered too strong interactions with the surface, producing thus a continuous saturation and sharp shifts (arrows, figure V.2.16).

Figure V.2.16a shows the relevant variations in the surface topography recorded on a 20 x 20 μm^2 image. The presence of several plateaux at different heights allowed us to scan smaller areas with lower variations in the z axis. However, the presence of artifacts due to the abrupt changes of height can be still observed over areas of 2.75 x 2.75 μm^2 (figure V.2.16b). When the surface steps are almost vertical, the lateral facets of the SFM tip (~60º) determine the movement of the lever over the same place of the surface so that, the image corresponds to the tip profile rather than to the surface itself.

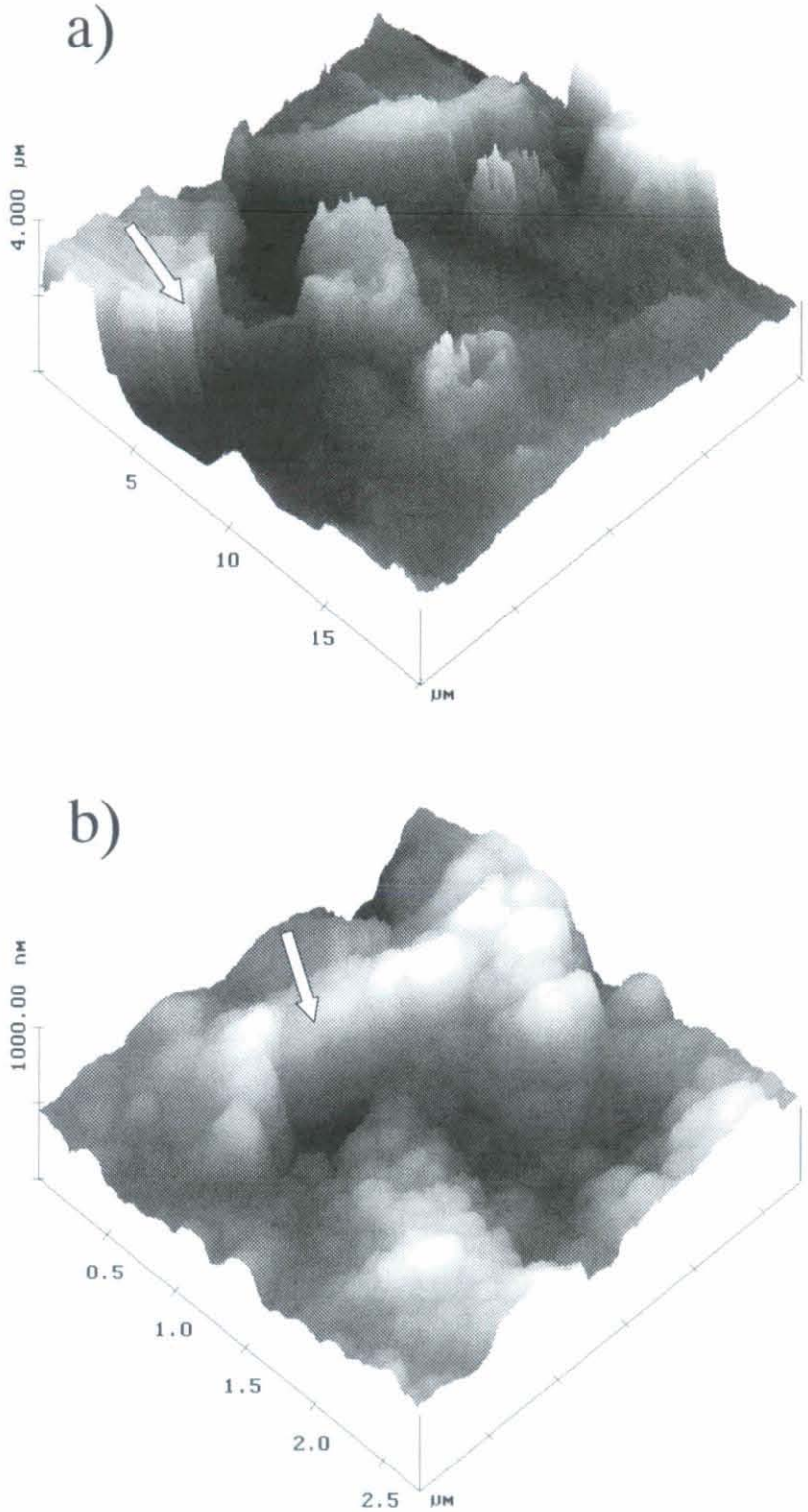

Figure V.2.16: SFM images of the aerosol-gel HAP coatings deposited onto TiO_2 at 500ºC before the etching treatment. a) 20 x 20 μm^2 b) 2.75 x 2.75 μm^2 area.

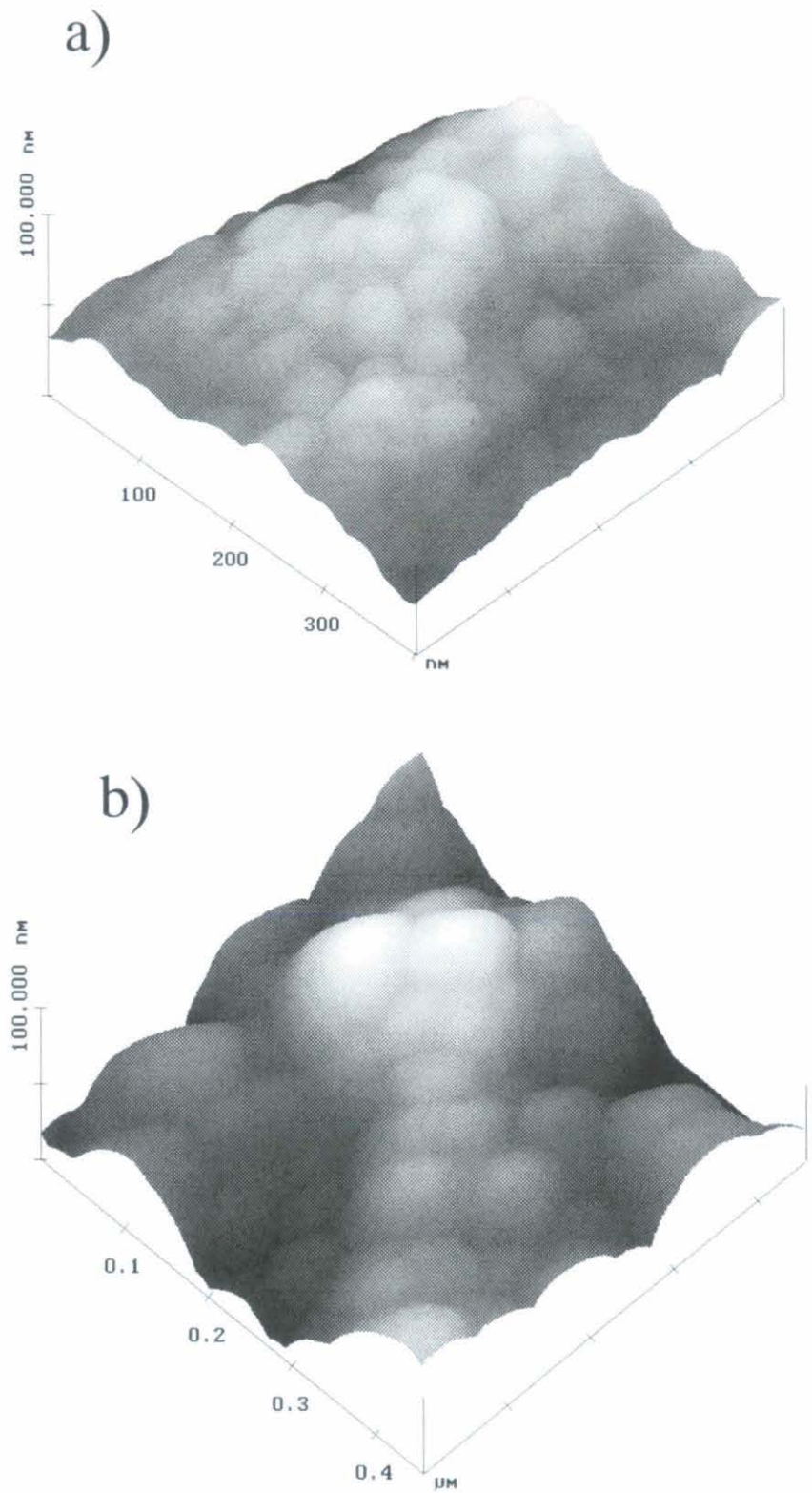

Figure V.2.17: SFM images of the aerosol-gel HAP coatings deposited at 500ºC before etching. a) 400x 400 nm^2 SFM image of HAP deposited over Si, b) 500x 500 nm^2 SFM image of HAP/TiO_2.

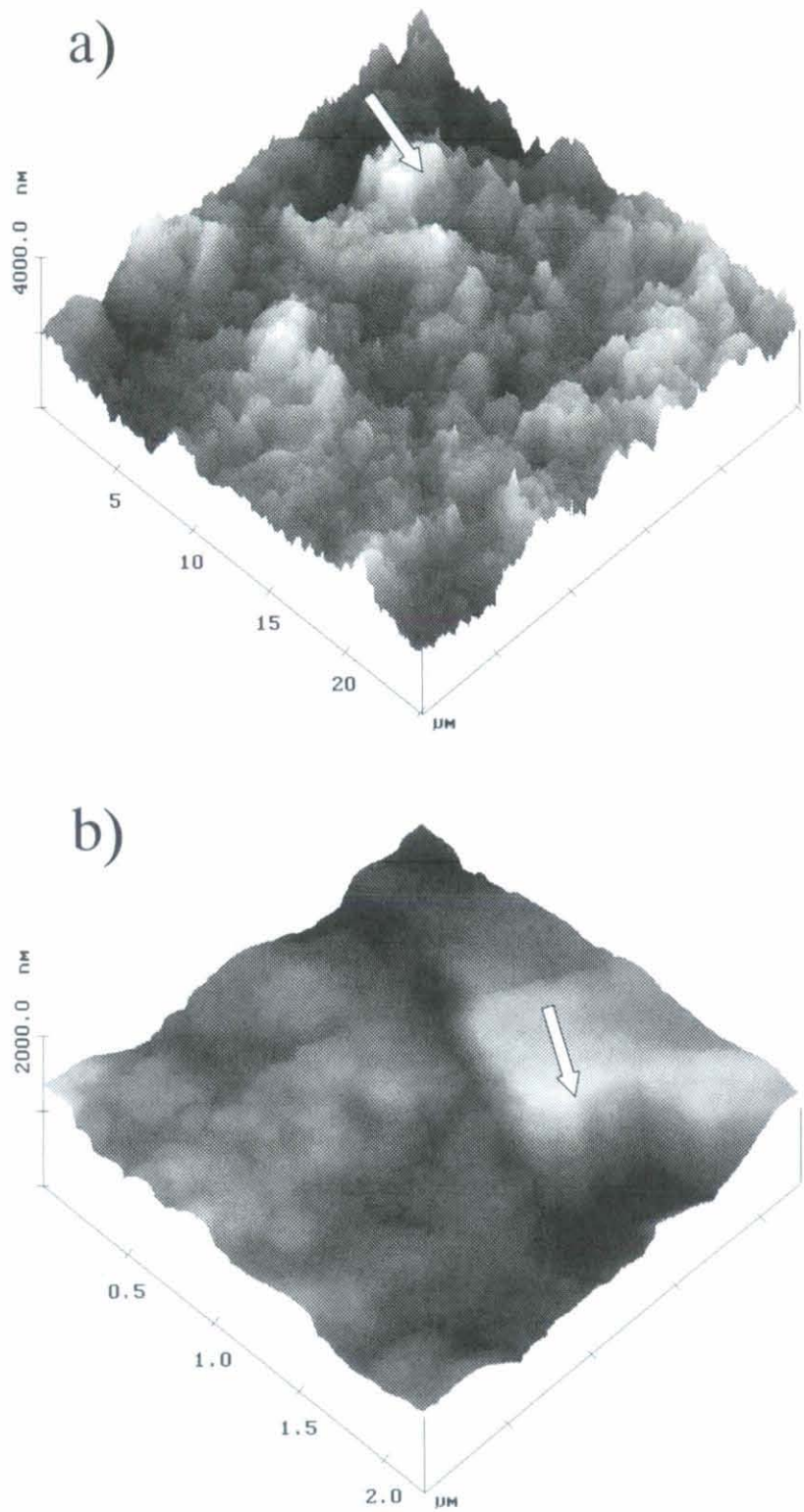

Figure V.2.18: SFM images of a chemically etched HAP coating deposited on TiO_2 at 500ºC after chemical etching. a) 25 x 25 μm^2 and b) 2.25 x 2.25 μm^2 area.

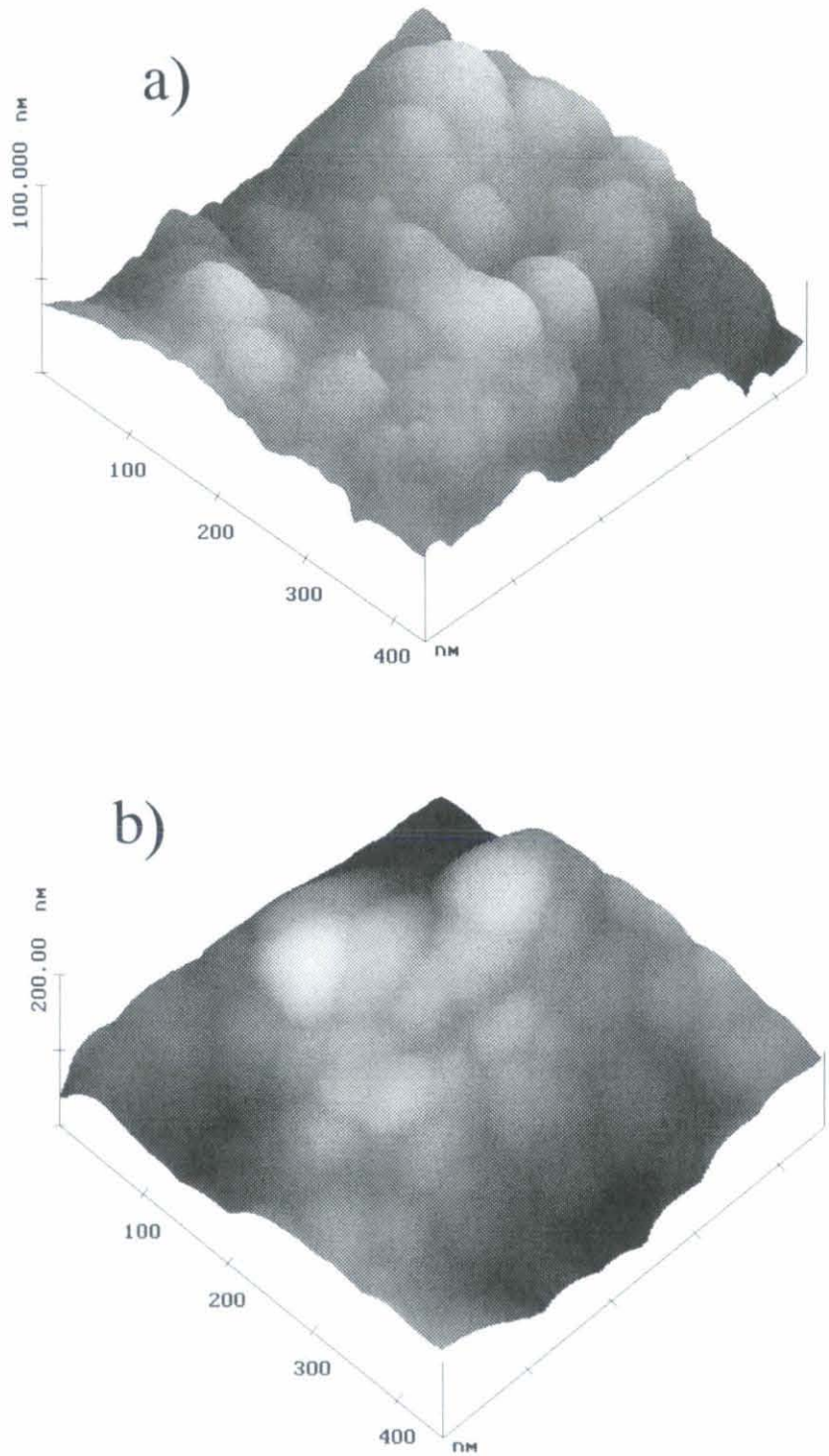

Figure V.2.19: SFM images of aerosol-gel HAP coatings deposited at 500ºC and chemically etched in HAc. a) HAP/Si and b) HAP/TiO_2.

When reducing again the scanning areas (500x500 nm^2), the films deposited on both Si and TiO_2 substrates were observed to present a similar granular structure displaying well-defined grain boundaries (figure V.2.17). The high contrast obtained in that case allowed to estimate the mean grain size to be about 55 and 45 nm for the Si and TiO_2 substrates, respectively (note the different scales of figures V.2.17a and b). Although the grain boundaries are mostly rounded, pseudo-hexagonal borders could be observed in many cases. This is considered as a new indication of the crystalline character of these grains. This pseudo-hexagonal shape, which is clearly observed in figure V.2.17b, are attributed to the presence of randomly conformed HAP structures.

The SFM study of the coatings after chemical etching led to the same technical limitations as non chemically etched films. Again, the surface topography could not be neatly resolved over areas larger than 500x 500 nm^2. Figure V.2.18a shows the relevant changes in surface topography over areas of 25 x 25 μm^2. Although the height variations at the surface are similar to those corresponding to non etched films, the overall thickness appears somehow more homogeneous after chemical etching. Again, the boundaries of flatter regions forming plateaux were observed to be affected by artifacts (figure V.2.18b). The study of 500x500 nm^2 areas proved that the coatings are principally etched at the grain boundaries. Rather than promoting grain dissolution, the acetic acid dissociates neighbour grains producing an etching process dominated by particle release. This is confirmed by the almost unaltered granular shape of the HAP crystals, both for Si and TiO_2 substrates (figure V.2.19a and b, respectively). Again, the mean grain size of the HAP particles grown on both Si and TiO_2 was observed to remain near 50 nm.

The estimation of the root mean square (rms) roughness and the maximal height between surface points (h_M) (Table V.2.1) further confirmed that the surface topography was relatively independent of the substrate used. Both HAP/TiO_2 and HAP/Si coatings presented rms roughness values of about 0.3 μm for scanning areas of 10x10 μm^2. They also exhibited similar h_M values of approximately 3 μm. Furthermore, the chemically etched HAP structures followed similar trends independently of the substrate used. The

values of h_M illustrate the difficulties for the SFM analysis since they almost reach the maximal amplitude of the cantilever.

	HAP/TiO_2	**HAP/Si**	**HAP/TiO_2 etched**	**HAP/Si etched**
rms roughness (μm)	0.4	0.3	0.4	0.5
h_M (μm)	3	2	3	3

Table V.2.1: rms roughness and h_M values measured by SFM on HAP samples deposited at 500ºC and analysed before and after chemical etching.

It is remarkable that our study presents a perfect correlation between the HAP crystallite sizes observed by TEM cross section (in the bulk) and SFM surface studies. This suggests the non-dependence of the HAP grain growth mechanism with respect to the depth (except special structural features depicted by TEM at the HAP/TiN interface). This statement is confirmed by the similarity of the surface morphology observed before and after chemical etching.

5.3 DISCUSSION AND CONCLUSIONS.

In this chapter we have shown that HAP/TiN and HAP/TiO_2 coatings grown by the aerosol-gel technique produce a polycrystalline HAP coating. In the case of HAP/TIN/TiAlV coatings, the preparation conditions produce unavoidably an oxidation of the TiN interlayer. The AES spectra clearly show a diffusion of the oxygen into the TiN interlayer after sintering. Furthermore, XRD diffractograms prove that at 800ºC, the N substitution by O leads to the anatase TiO_2 phase. This behaviour is similar to the one observed for $SrTiO_3$/TiN/$YBa_2Cu_3O_7$ superconducting multilayer structures, which were found to fit better a $SrTiO_3$/TiO_2/$YBa_2Cu_3O_7$ composition, as deduced from chemical analysis [LIN01]. Concerning HAP/TiN/TiAlV structures, the oxygen diffusion has been also evidenced at the TiO_2/TiAlV interface. In any case, this diffusion did not alter the stability of the TiO_2 layer.

We have observed that a dense and adherent HAP coating is formed at the HAP/TiN and HAP/TiO_2 interface. The HAP crystals forming the HAP/TiN interface layer present a predominant (002) orientation with respect to the TiN/Si substrate. However, structural arrangement faults were also observed. In any case, the observation of an intimately grown HAP interface layer is considered as a sign of the good adherence of the HAP coatings. HAP crystals have been shown to be the most stable CaP phase in biological media [EBR93]. Furthermore, the presence of satellite phases in the coatings has been pointed out as responsible of the lack of adhesion of HAP coatings [HUA92]. Thus, the observation of the highly oriented HAP crystals at the interface suggests the good adherence of our coatings even after application in biological media. This confirms the overall mechanical quality of our HAP coatings.

The spectroscopic (RBS and AES) and morphologic analysis (SFM) of the HAP/TiO_2, HAP/TiN and HAP/Si coatings have shown that the substrate plays no relevant role in determining the coating properties. Moreover, the remnant presence of HAP structures after chemical etching in HAc confirms the in-depth homogeneity of our HAP layers. This behaviour can be extrapolated to simulated body fluids (pH= 7.25), which have a greater pH than HAc (pH = 3), since it is well known that the rate of dissolution of HAP decreases for increasing pH. We have thus tested our coatings in a more aggressive medium than the attended for applications.

A comparison with HAP/Ti films grown in a previous work by electrodeposition (see Chapter I) shows that aerosol-gel derived HAP coatings are noticeably rougher and present a very different grain structure. Parallel orientations between needle-like crystals have been observed in electrodeposited HAP coatings. On the contrary, aerosol-gel derived HAP coatings exhibit random crystal orientations. Besides, aerosol-gel processing presents a powerful advantage, since contrary to electrodeposited HAP, the final HAP coating is not limited in thickness, i.e. the thickness can be flexibly adjusted by using a multilayer deposition procedure.

Finally, we consider that both TiN and TiO_2 coatings are suitable buffer layers for prosthetic applications. They have shown to be appropriate coatings for the

formation of an adherent HAP layers avoiding a drastic diffusion of Ca or P atoms. Their stability (case of TiO_2) or transformation into a stable phase (case of TiN), ensures also a good isolation of the biosystem from the atoms present in the prosthetic alloy.

CHAPTER VI: *SURFACE FUNCTIONALISATION BY THE SOL-GEL FIXATION OF AMINE GROUPS.*

CHAPTER VI: *SURFACE FUNCTIONALISATION BY THE SOL-GEL FIXATION OF AMINE GROUPS.*

6.1 INTRODUCTION.

As it was pointed out in the general introduction of Chapter I, one of the most required solutions for tissue regeneration, and in general for the fixation of biomolecules on surfaces, is the functionalisation of surfaces by physico-chemical processes that yield high concentrations of biologically active molecular groups. For instance, these principles are applied in the development of bio-chips and bio-arrays used for sequencing DNA. Amines are forming parts of peptides and have direct implication in controlling protein absorption. In this work, we have thus taken advantage of the activity of the amines, or more specifically NH_2 groups, to test the preparation of functional surfaces for the specific binding of biomolecules.

The interest in amine groups has been recently increased since they can be applied to the development of biosensors with high biological specific sensitivity. However, the interest for amine-based surfaces has been traditionally wide. The applications of these coatings range from chemical aspects (i.e. corrosion inhibition [SOK86] or biological modelling and sensing [TAL98]) to those derived from the physical properties of these coatings (i.e. generation of second order optical effect [WHI94], friction and wear resistance [KON97])

The processes that lead to surfaces with high density of amine groups are multiple. Both liquid to solid and gas to solid transformations have been described. Concerning the former methods, adsorbed amines have been obtained on SiO_2, γ-Al_2O_3 and CaO by strong interaction via H bonding [SOK86]. This method also allowed the interaction of octadecenylamine with sodium nitrate particles [GAN89]. The formation of Langmuir-Blodget monolayers has been intensively studied for the processing of this kind of coatings [WHI94, PUG94, KON97]. The stabilisation of the monolayers was ensured by the affinity of thiol groups [WHI94], stearic acid [PUG94, KON97] or by the presence of soluble substrates that allow the formation of H bonds [TAL98]. The

gas to solid transformations have been studied for the chemisorption of α amine acid vapours [BAS90] as well as for the construction of dendritic organic films [ZHA98].

These former studies support that the gas methods induce a covalent bonding, which should be more stable than electrostatic bonding (for instance hydrogen bonds). However, the development of a sol-gel procedure can make compatible the advantages of both, the technical facilities of a liquid to solid transformation and the formation of covalent bonding. Accordingly, a previous work reports on the formation of amine active surfaces by the hydrolysis and polycondensation of diethylamine-propyl-triethoxysilane [VAS95].

In this thesis, preliminary studies have been initiated to produce titania thin films doped with amine groups via the sol-gel route. Both propylamine (PA, C_3H_9N) and aminopropyl-triethoxysilane (APTS, $(C_3H_8N)Si(CH_3)_3$) have been tested as sources of amine groups and the influence of molar concentrations has been analysed. Due to its high sol-gel reactivity, tetraisopropyl-orthotitanate (TIPT) has been used to induce the fixation of amine groups. The thermal evolution of the amine bonds as well as the formation of a Ti-O-Si poly-oxide network has been studied for different sintering temperatures. From a general point of view, these studies aim to demonstrate the possibility of producing coatings with a high surface density of amine groups that allow the covalent fixation of biological or organic species to the inorganic material.

6.2 EXPERIMENTAL.

The precursor solution was prepared in a two step process from TIPT and one of the following reagents: APTS or PA. First, a 0.4 M TIPT solution diluted in ethanol with a TIPT/water ratio r_w= 0.82 and a pH= 1.27 was prepared. Secondly, volumes of APTS or PA were added in order to obtain a N/Ti mr of: 1 or 2. TIPT/APTS, TIPT/PA and pure TIPT solutions were deposited by spin-coating at 3000 rpm during 45 s. (100) Si wafers and silica plates were used as substrates. Before deposition, the Si wafers (specially chosen for FTIR analysis) were treated in air at 500°C for 2h to eliminate adsorbed impurities and to form a thermally stable SiO_2 surface film. In this study, we focused on as-deposited (AS) films or films heat-treated at 150, 300 or 500°C. In the

text that follows, the film nomenclature refers to the characteristic amine precursor, the amine to TIPT molar ratio and the sintering temperature (e.g. PA2-150, APTS1-300, TIPT-AS). The characterisation of the coatings has been mainly carried out using Fourier transform infrared spectroscopy (FTIR). X-ray diffraction (XRD) was used to study the influence of mixed precursors in the structure of the coating after sintering at 500ºC. Scanning electron microscopy (SEM) was used to test the influence of the amine precursors on the surface morphology. Coatings deposited with a micropipette on Si and SiO_2 were also studied to test the specific binding of DNA and RNA.

6.3 PHYSICOCHEMICAL CHARACTERISATION.

A detailed analysis was performed by FTIR spectroscopy to qualify the presence of amine groups in the films formed from the APTS and PA precursors. The spectra presented in figures VI.1.1 and VI.1.2 show the characteristic absorption regions of the amine groups (1500-1700 cm^{-1} and 3100-3600 cm^{-1} for stretching and bending modes, respectively). The wide band detected between 3200 and 3400 cm^{-1} for an APTS2-AS film denote the presence of NH_2 symmetric and asymmetric stretching modes (figure VI.1.1a). These bands are not detected in the spectra corresponding to APTS1-AS and appear only weakly in PA2-AS and PA1-AS films at 3225 and 3340 cm^{-1} (figure VI.1.1b, c and d).

In particular, the APTS1-AS spectrum appears very similar to the pure TIPT-AS spectrum (figure VI.1.1e). Only a wide band can be observed between 3200-3600 cm^{-1}, which is attributed to adsorbed OH groups. These latter samples do not present another wide amine band at approximately 3450 cm^{-1}, which is weakly detected in APTS2-AS, PA2-AS and PA1-AS xerogel films. However, the presence of bands located at 1620 and 1580 cm^{-1}, assigned to NH_2 bending modes, confirm that all the APTS derived samples contain NH_2 groups. These bands appear more intense for the APTS2-AS sample, which confirms a greater content of amine group in this film. Equivalent bands are observed in PA samples at 1610 and 1585 cm^{-1}. Contrary to APTS samples, in the case of PA samples the band intensity did not depend on the amine to TIPT molar ratio. All the differences between PA and APTS spectra suggest a different incorporation of the amine groups in the corresponding films.

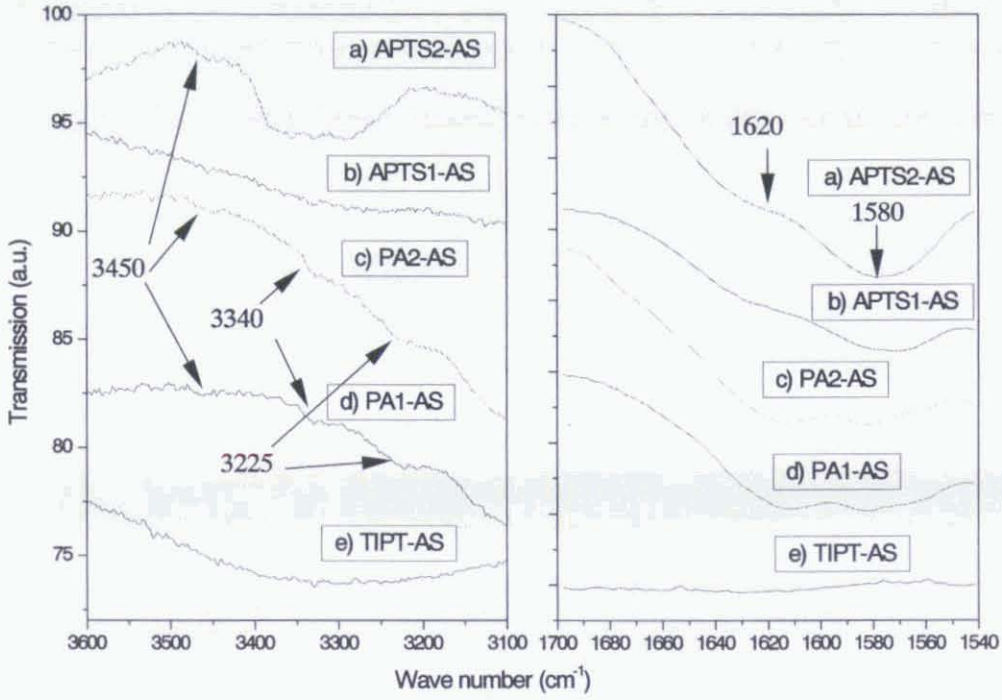

Figure VI.1.1: FTIR spectra of as-deposited coatings: a) APTS2-AS, b) APTS1-AS, c) PA2-AS, d) PA1-AS and e) TIPT-AS.

The spectra presented in figure VI.1.2 illustrate the thermal evolution of the amine bands for the APTS2 and PA2 samples. The APTS2 spectrum shows that, although with a certain absorption reduction, the amine stretching bands remain clearly detectable after sintering at 150°C (figure VI.1.2b) and disappear only after sintering at 300°C (figure VI.1.2c). The bending bands of APTS-150 in the 1500-1700 cm^{-1} range appear however shifted with respect to the previous assignments for APTS-AS. No amine bands could be detected in the case of PA2 samples sintered at 150°C or more (figures VI.1.2e-f). These features confirm the previously mentioned differences and demonstrate that the incorporation of amine groups in APTS films provides a better amine stabilisation compared to PA films.

The equivalent PA2-150 xerogel (figure VI.1.2e) presents a wide band between 3100-3200 cm^{-1} that can not be directly related to the presence of amine groups. However, the amine related band at about 3450 cm^{-1} can no longer be detected on either APTS nor PA xerogel films. After sintering at 300ºC no amine related bands were present in the xerogel films (figure VI.1.2c and f).

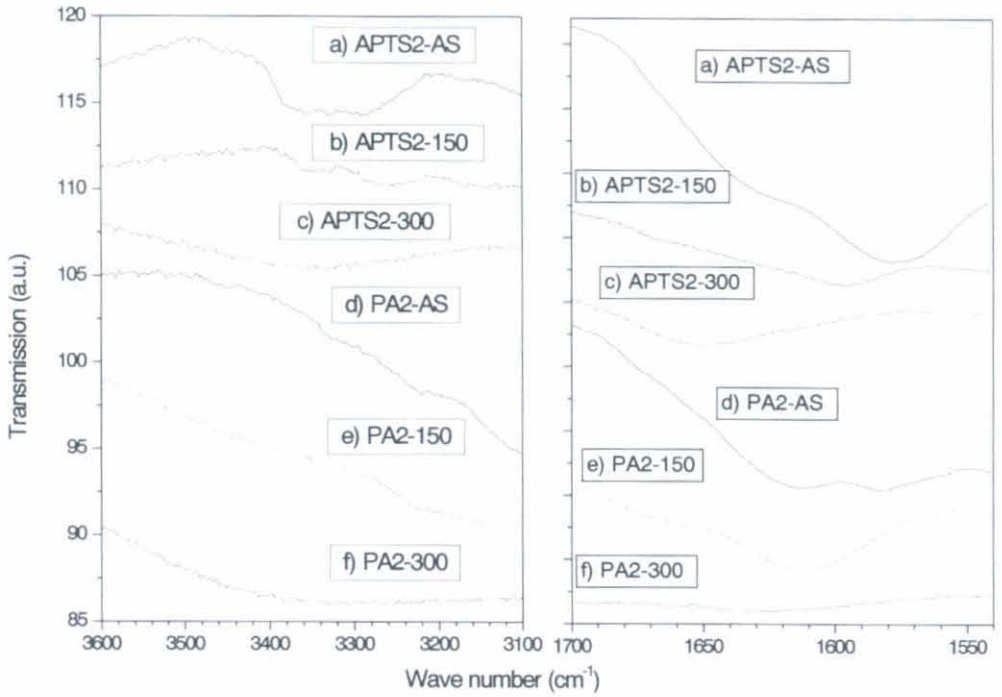

Figure VI.1.2: FTIR spectra of films heat treated at various temperatures: a) APTS2-AS, b) APTS2-150, c) APTS2-300, d) PA2-AS, e) PA2-150 and f) PA2-300.

The films were studied by XRD after annealing at 500°C in order to analyse the effect of precursor composition on the structure of the coating. The phases detected were observed to depend on the nature of the precursors. The APTS2-500 diagram does not show any diffraction peaks (figure VI.1.3a). In that case, it is believed that the formation of a mixed Si-O-Ti network inhibits the crystallization process. This is generally the case for mixed SiO_2-TiO_2 sol-gel films, provided that the sintering temperature and the Ti amount are not too high, i.e. no SiO_2-TiO_2 phase separation occurs [MAR92].

On the contrary, the formation of a single titanium oxide network favoured the formation of polycrystalline coatings. This was the case for both the PA2-500 and the non doped TIPT-500 coatings (figures VI.1.3b and c). These polycrystalline coatings presented a clearly defined anatase phase (PDF 84-1286). It must be noted that, for the PA2-500 film, the presence of PA seems to influence the coating crystallisation. The

diffraction peaks in figure VI.1.3b are somehow broader than those present in figure VI.1.3c, which suggests that PA reduced the crystallisation degree.

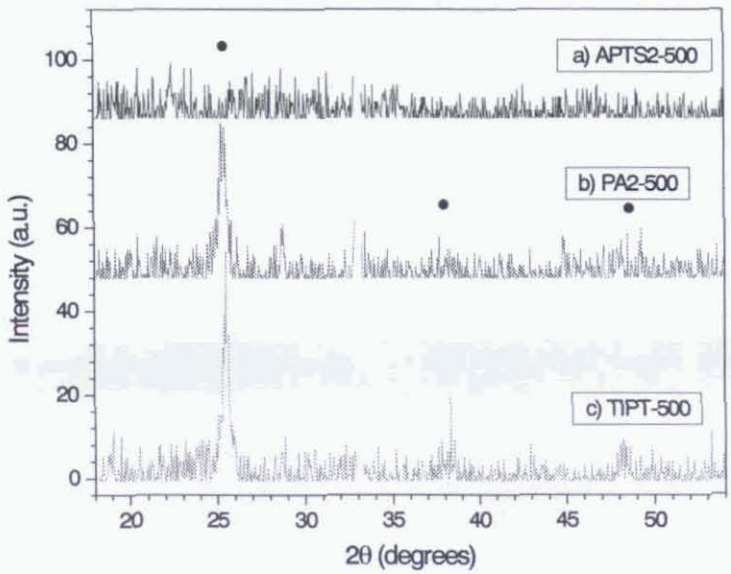

Figure VI.1.3: XRD diagrams of the xerogel films sintered at 500°C, a) APTS2-500, b) PA2-500, c) TIPT-500.●: TiO_2, anatase.

SEM images show that the surface morphology of the coatings was also influenced by the amine precursor nature (figure VI.1.4). Films formed from APTS/TIPT precursors exhibited a very homogeneous surface at the micron scale (figure VI.1.4a). This trend was not observed for the coatings formed from PA/TIPT precursors (figure VI.1.4b). In that case, granular structures of heterogeneous sizes are observed to cover the substrate, configuring thus a rough surface. The amine-free TIPT films exhibited also homogeneous surfaces, as those observed for APTS/TIPT precursors (figure VI.1.4c).

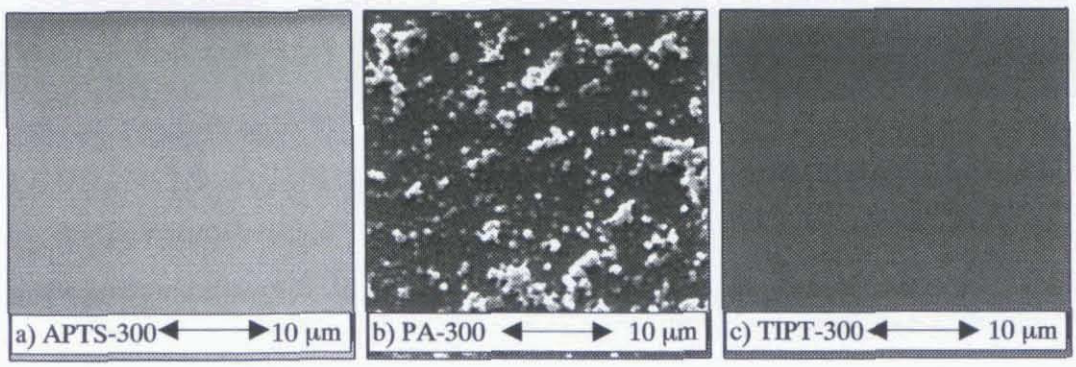

Figure VI.1.4: SEM micrographs of the xerogel coatings sintered at 300°C a) APTS-300, b) PA-300 and c) TIPT-300.

6.4 BIOLOGICAL CHARACTERISATION.

According to the better behaviour of APTS/TIPT films, i.e. the greater incorporation and the better stabilisation of amine groups, we anticipated that such amine enriched surfaces could be suitable for the specific binding of RNA and DNA. In order to test this functionality, (100) Si and SiO_2 substrates were partially coated with an APTS/TIPT (N/Ti = 2) microdroplet. After xerogel formation (solvent evaporation and sol-gel transformation) the samples were incubated in RNA and DNA, which were subsequently hydrolysed in order to substitute a radioactive P^{32} chain that allows a detection of the molecular density through the isotopic decay (i.e. the samples with the radioactive isotope were faced to a photographic film for two hours).

The set of images presented in figure VI.1.5 shows that, for both the Si and SiO_2 substrates, areas coated with the APTS/TIPT xerogels induced an intense signal. No signal could be detected for the uncoated surrounding part of the substrates. This result was the same irrespective of the nucleic acid considered, i.e. both DNA and RNA were specifically bound to the substrate by means of the APTS/TIPT xerogel scaffolds.

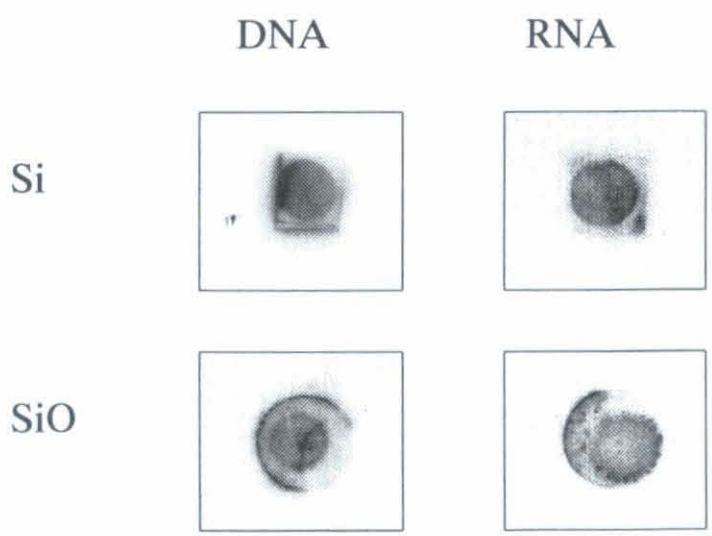

Figure VI.1.5: Preferential activity of the P^{32} isotopes on coated substrate. a) DNA/(APTS-TIPT)/Si, b) DNA/(APTS-TIPT)/SiO_2, c) RNA/ (APTS-TIPT)/Si, d) RNA/ (APTS-TIPT)/SiO_2.

6.5 SUMMARY AND CONCLUSIONS.

Xerogel films have been prepared by the spin-coating technique from pure TIPT, mixed APTS/TIPT and mixed PA/APTS precursors in order to study the surface fixation of amine groups. FTIR results prove that both APTS and PA are effective for the fixation of those groups. However, the amine content of the PA doped xerogels was observed to be relatively independent of the molar concentration of PA. On the contrary, the higher the molar concentration of APTS, the higher was the amine content of the derived films. Amine groups have been shown to decompose with temperature. However, in the case of APTS precursors some amine groups remained on the surface after sintering at 150ºC, while no group could be detected after sintering PA/TIPT films at 150°C. At 300ºC neither the APTS, nor the PA doped films show evidence of amine content.

It has also been observed by XRD that sintering at 500ºC produces a predominantly amorphous network in the case of the APTS amine precursor, while polycrystalline coatings are obtained when a PA precursor is used. Such differences were also observed from a morphological point of view. While APTS precursors form homogeneous surfaces at the micron scale, PA precursors lead to very rough structures. This morphological feature is determined by the kinetic mechanism involved during the drying and polycondensation process of the xerogel films. As we have introduced in Chapter II, homogeneous SiO_2 films can be formed under acidic influence, which can explain the good homogeneity of APTS derived films. On the contrary, TiO_2 films produced from PA precursors underwent a base catalysis mechanism (pH= 9) which is known to cause the Ti precursor precipitation and to favour the formation of granulated surfaces in the case of titania at pH> 3 [BUR01].

Our experimental results show that two different mechanisms of amine group adsorption occur, depending on the amine precursor nature. The presence of the absorption band at 3450 cm^{-1}, which desorbs at temperatures lower than 150ºC suggest the formation of H bonds [SOK86]. Van der Waals interactions have been proposed to explain the adsorption of amine alkyl chains at levels higher than those expected from pure H bonding [GAN89]. However, the remnant presence of amine bands in APTS

films heated at 150ºC suggests that a more stable chemical bonding is preferentially involved for these films, i.e. a covalent bonding.

We have to emphasise that, for potential applications involving amine enriched surfaces, APTS xerogel films present two main advantages. The first one concerns the surface homogeneity of these films against PA derived xerogels, which allows a higher performance for the microscopic and spectroscopic detection of species linked to the adsorbed amine groups. The second, and most important one, is that, as the APTS precursors provides a higher content of stable amine groups, a better detection sensitivity of the activated surface can be ensured.

Finally, concerning the biological applications of APTS/TIPT xerogels, we have shown that both DNA and RNA can be specifically bound to a substrate by means of the APTS/TIPT xerogel scaffolds. It is important to remark that the potential of this approach is all the more important as it is compatible with any kind of substrate. This opens new branches of applications such as those derived from the use of semiconductors, metals, polymers or glasses.

CHAPTER VII: *GENERAL CONCLUSIONS AND PERSPECTIVES.*

CHAPTER VII: *GENERAL CONCLUSIONS AND PERSPECTIVES.*

7.1 GENERAL CONCLUSIONS.

In this thesis, we have described in a step by step manner experimental procedures devoted to the preparation of biologically functional HAP/TiO_2 and HAP/TiN structures on both Si (100) and TiAlV substrates. The intermediate Ti based layer and the HAP outlayer have been characterised independently and after association. We have described their structure, composition, morphology and also their mechanical response. Finally, we have evaluated the biological behaviour of the materials by seeding human derived cells. In addition, we have shown preliminary results concerning the deposition of an amino based bioscaffold, which could be applied to the specific binding of biomolecular species.

Concerning the preparation of intermediate Ti based layers, we have shown that the physico-chemical properties of aerosol-gel derived TiO_2 coatings are directly related to the conditions of sintering treatment applied to induce the condensation, crystallisation and densification of the films. In this way, coatings annealed at temperatures of 500ºC or more were found to be composed of a polycrystalline anatase phase. On the opposite, coatings thermally treated below that temperature presented an amorphous character. Furthermore, the mechanical properties of the different TiO_2 coatings were satisfactorily related to their physico-chemical properties. Amorphous coatings presented higher plastic deformations and higher values of the mean indentation creep. They were not as hard as the crystalline coatings and presented as well lower values of the Young's modulus. Aerosol-gel derived TiO_2 multilayers with a graduated Young's modulus could be beneficially used to reduce the mechanical mismatch between bone and a metallic alloy based implant. This would reduce the degradation of the bone tissue that surrounds the tougher metallic prosthesis.

TiN interlayers have been also successfully processed by plasma magnetron sputtering. In this case, the physico-chemical properties of the TiN coatings were found to be relatively independent of the annealing treatments performed in N_2 atmosphere at

temperatures below 600ºC. For biological applications involving a passivation coating, TiN films present the advantage face to TiO_2 coatings of higher values of hardness and Young's modulus.

We have shown that it is possible to deposit HAP coatings by the aerosol-gel route. Both triethyl-phosphate and phosphoric acid based sols led to the optimisation of nearly stoichiometric and well adhered polycrystalline HAP coatings. Only phosphoric acid precursors showed a certain sol-gel reactivity during sol preparation in ethanol, leading to a partially substituted ethyl phosphate. However, in any case the sol-gel transformation was insufficient, and a satisfactory liquid to solid transformation could be only achieved through the use of a stabilisation thermal treatment at 500°C. Multilayer coatings were then finally sintered at temperatures of 650 up to 1000ºC. The high specific area was a common feature for the HAP coatings prepared from both precursors. Very rough surfaces were formed with pore sizes ranging from 5 nm to10 μm. The coatings are formed by adjacent crystals nucleating with random orientations and leaving internal voids that produce the highly porous structure. Finally, we have determined that the chemistry of phosphoric acid derived sols leads to a noticeable advantage with respect to triethyl-phosphate sols, since the amount of satellite phases stabilised with the former precursor is lower at any sintering temperature.

The behaviour of the Ti based interlayers and HAP outer layer in biological media was assayed by seeding human derived cells. A comparison of the behaviour of the cells with respect to a bare TiAlV standard alloy allowed to establish that human chondrosarcome cells present a preferential activity while adhered onto aerosol-gel derived TiO_2 coatings. In the case of human mesenchymal stem cells, it has been evidenced that they adhere to magnetron sputtered TiN surfaces to degrees not reached by the bare surfaces of TiAlV alloys. This is a significant result since the good electrical conductivity of TiN can be used to study the differentiation processes of these cells exposed to electrical stimuli. Finally, the cells cultured on aerosol-gel derived HAP coatings have shown proliferation signals and a tendency to form colonies. HAP coatings are thus of potential interest as support for the differentiation of these cells and their ulterior implantation.

Special attention has been paid to the surface and interface characterisation of HAP/TiO_2 and HAP/TiN structures. We have shown that both morphologic and compositional analysis, performed on the structures before or after etching, confirm the in-depth homogeneity of the HAP outlayer. Furthermore, the characterisation of these structures deposited on different substrates confirms that the properties of the HAP coating are determined by the aerosol-gel deposition and sintering parameters rather than by the nature of the substrate. It has been shown that the HAP crystals form a dense interfacial layer that intimately bound with the interlayer and ensure a high adhesive strength. However, this intimate contact produces also diffusion processes involving preferentially the O atoms, which are responsible of a drastic oxidation of the TiN interlayer. In the case of HAP/TiO_2 structures, the O diffusion from the interlayer affects the TiAlV substrate. It has also been shown that a certain diffusion of Ca and P atoms might be present for both kinds of interlayers.

At the end of this manuscript, we have shown that the composition of aminopropyl-triethoxysilane/tetraisopropyl-orthotitanate (APTS/TIPT) sols can be optimised in order to produce thin film bioscaffolds by the sol-gel route. Covalently bonded amino groups have proved to be useful for the biological functionalisation of materials allowing the specific linking of ribonucleic acids on different surfaces. A compromise between the condensation and amine content has been found so that the coatings are active and *in-vitro* resistant at the same time. These coatings are not only interesting for orthopaedic applications but also for biomolecular detection and bioelectronic circuitry.

Concerning the deposition processes, we have proved that the aerosol-gel method is particularly suited for biomaterial processing when compared with the traditional spin or dip-coating methods. The system lends itself to the deposition on large and three-dimensional substrates and is suited for the processing of microsystems. This is specially attractive for the development of coatings onto prosthetic materials and molecular bioarrays. The plasma sputtering technique is an ideal complementary tool,

which can be used for the deposition of conductive materials in electrodes for biomedical devices as well as dense nitride diffusion barriers.

From a general point of view, biological assays prove that the materials processed in this work present a good biological behaviour and can thus be considered for the development of prostheses with a better bone –implant matching or even for biosensing or bioelectronic devices. Furthermore, these materials may be useful for tissue engineers. The development of techniques for the handling of human cells from culture dishes adapted to a selected functional environment could be used to accelerate the implantation of prostheses and the regeneration of tissues.

7.2 PERSPECTIVES.

Nowadays, the quest of materials showing novel or improved properties in biological media is a research field in continuous expansion. According to the promising results obtained in this work using the sol-gel procedure, we can envisage the study of new materials for the two configurations presented in this work. That is, materials for orthopaedic structures deposited over metallic alloys with a first interlayer of good mechanical and passivating properties and a bioactive outlayer providing a better bone contacting interface with bone tissue. Secondly, hybrid thin films acting as bioscaffolds allowing the specific binding of biomolecular species.

Concerning the former structures, we have recently obtained preliminary results concerning the sol-gel processing of $CaTiO_3$ thin films. These coatings present the advantage of intermediate physico-chemical properties between the Ti based interlayers described in this work and the HAP outlayers. They are highly stable due to their perovskite crystalline structure and they show very rough morphologies. These are promising results for their application on orthopaedic alloys as a substitute of the HAP/Ti(O_2-N) structure or as a part of a more complex structure HAP/$CaTiO_3$/ Ti(O_2-N). However, one of the most relevant investigations, concerning the biological assays, has not been carried out yet.

The research, initiated in this thesis for the development of sol-gel derived hybrid bioscaffolds, will be continued in two directions. On one hand, we envisage to adapt the composition of APTS/TIPT sols to make them compatible with the aerosol-gel process. Besides its previously mentioned advantages, this technique is compatible with a micro-masking process (deposition of individual microdroplets), which is favourable for the development of biosensing micro devices. On the other hand, we are interested in the study of sols based on other aminosilanes, such as trimethoxysilyl-propyl-diethileneamine, which is specially attractive for bioelectronic applications due to its good interaction with neuron axons.

ANNEXES.

ANNEX I: *SAMPLE PREPARATION FOR TEM CROSS SECTION OBSERVATIONS.*

In chapters IV and V, several TEM images of HAP thin film cross sections have been presented. This kind of images give relevant information concerning the grain distribution in a coating, orientation of structures with respect to the substrate, or even information concerning the interface between the coating and the substrate. The advantages of cross section observations are thus evident compared to the observation of scratched samples. For instance, this has allowed to study the growth mechanisms of TiSi structures at the interface with the substrate [PER95] or to describe porous silicon multilayers induced by AC electrochemistry [MAR00]. However, the preparation of samples for the TEM observation of TiN film cross sections is a delicate process. Basically, it consists in subsequent mechanic and ionic etching treatments, which are necessary to obtain a thin sample (about 100 Å in thickness) transparent to the electron beam [BAR96]. The intermediate preparation steps are presented in the following paragraphs and summarised in figure A.I.1.

a) Two slices of approximately 0.500 mm thickness x 2 mm length must be cut from the original coating by using a diamond disc or a diamond filament. This equipment minimises the damage to the coating (foiling, etc) that can be produced if wide edge elements are used (figure A.I.1a).

b) Two of these slices are inserted, with the coated sides face to face, in a Ti based structure that acts as protective frame during mechanical etching. The slices can be fixed by pressing the two outer fringes of the Ti frame (figure A.I.1b, c and d).

c) To ensure the mechanical stability of the coupled structure, a mixture of SiC and araldit is melted at 130ºC and used to fill the voids. The sample with the composite is left to polymerise during one hour at 180ºC.

d) The mechanical etching is carried out by pasting the structure to a metallic support with a protective mechanism based on a back screw that allows a control of the

thickness exposed to friction with the SiC grit. Three different abrasive SiC papers are used, in order to progressively reduce the particle size until a roughness of about 0.6 μm is reached. This polishing must be applied to both sides of the sample. A binocular is used to more precisely control the thickness. The final thickness must be about 50 μm (figure A.I.1e).

e) Ion beam milling is then carried out in a Gatan PIPS system with a double Ar^+ beam regulated at 5 KeV and an incidence angle below 10°. The working pressure of 5.10^{-6} mbar ensures a correct evacuation of the particles sputtered from the sample ensuring a continuous efficiency of the milling process. The sample is under continuous modulated rotation in order to obtain a selective perforation (figure A.I.1f). For the last 5 min of ion beam milling, the incidence angle is reduced down to 6° to obtain a wide terrace with a thickness between 0-100 Å.

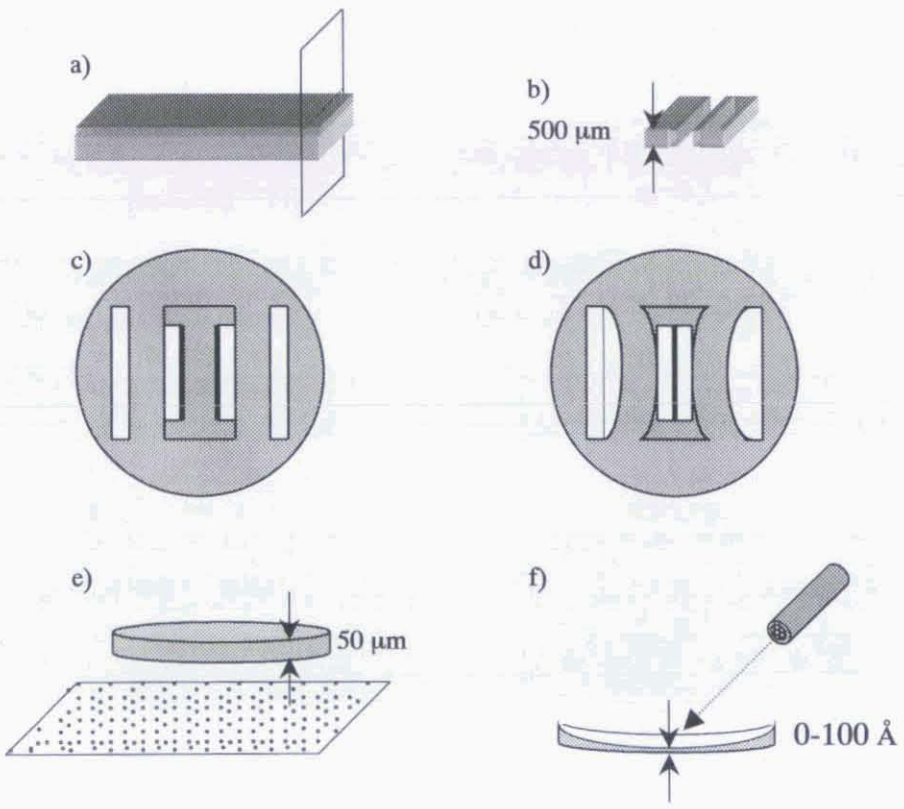

Figure A.I.1 Sample preparation for TEM cross section observations. Cutting (a and b), arrangement of the thin film stripes in the titanium structure (c and d), mechanical etching (e) and beam milling (f).

ANNEX II: *ULTRAMICROINDENTATION OF THIN FILMS.*

In chapter III, we have studied the mechanical response of TiN and TiO_2 thin films deposited over Si substrates. The evaluation of this mechanical response is based on the determination of several parameters, which are obtained from the indentation curves or from the indentor fingerprint. These parameters are directly deduced from the experimental data in the case of the plastic energy of deformation (PED) or the mean indentation creep (MIC). However, the determination of the hardness (H) and Young's modulus (E) requires a more sophisticated approach based on the interpretation of the elastic and plastic deformations occurring during the indentation. In this frame, we have applied the model of Oliver and Pharr [OLI92] in order to calculate the depth of indentation, which allows the determination of H and E. The method has already been successfully applied in our laboratory to characterise ion implantation in TiN and Si oxinitride thin films prepared by plasma enhanced chemical vapour deposition [ROD96].

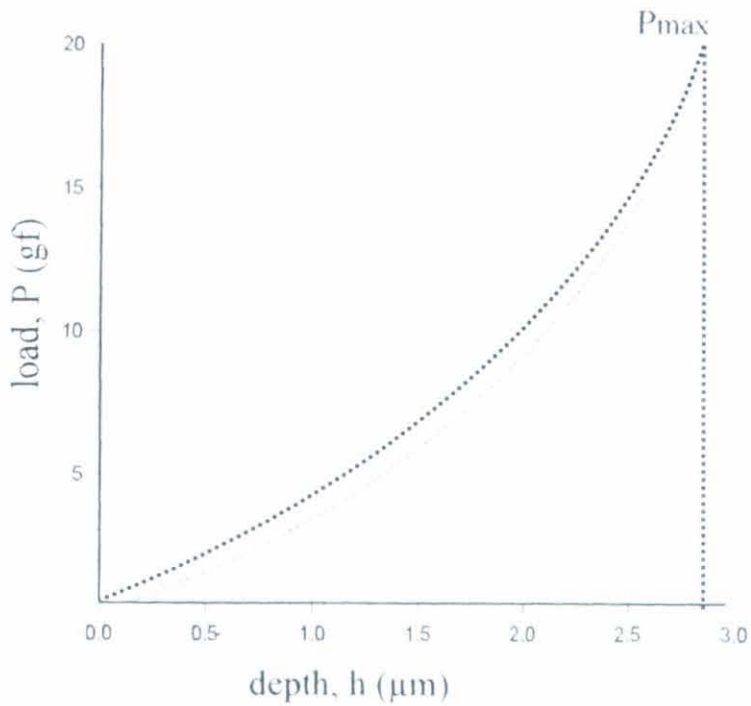

Figure A.II.1 Ideal response to indentation of a totally elastic (green) and a brittle (red) thin film.

The PED of a thin film can be deduced by determination of the area contained between the unloading curve (work performed by the coating to retrieve the indentor tip) and the loading curve (work performed by the indentor to penetrate the coating). A brittle material with low elastic limit will fail to give any energy back and will present an almost vertical unloading curve. On the opposite, a very elastic material will give almost all of the energy of deformation back so that the loading and unloading curves are almost overlapped. These features can be observed in figure A.II.1. The MIC is deduced from the slope of the depth of indentation as a function of time while the sample is probed at constant load. Depending on the load and loading time, a series of processes can be identified according to slope changes [POL86]. In any case, we consider in our description that the curves are dominated by a linear behaviour as shown in figure III.3.4 of chapter III for a TiN coating.

The most relevant parameters for the determination of H and E are presented in figure A.II.2. The indentation profile shows the intermediate state, produced at the moment of maximal indentation (identified by the maximal depth h_{max}), and the final state after the elastic recovery (h_f). The profile takes into account the non linear recovery with respect to the centre of indentation, so that the profile of the surface does not exactly reproduce the indentor shape, due to the non homogeneous distribution of the plastic deformation. During the loading process, the profile will match the indentor shape only above a certain depth threshold (h_s).

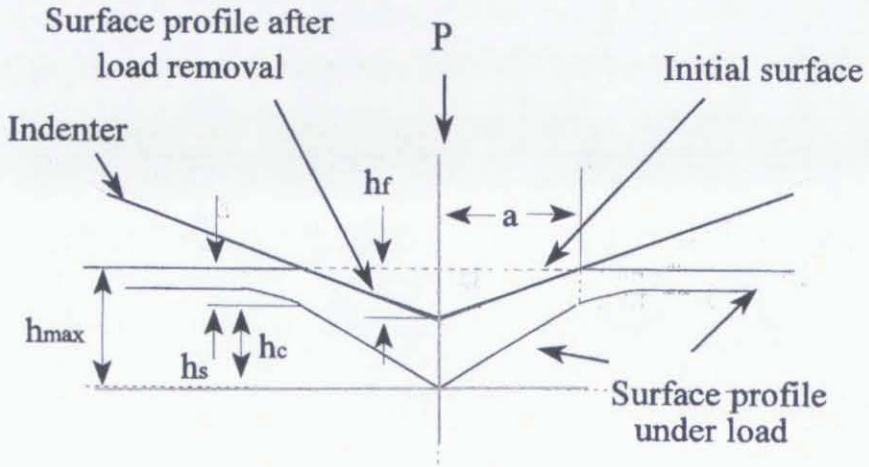

Figure A.II.2 Surface profiles during indentation and after load removal.

From the different parameters, we can calculate the so-called depth of contact (h_c) that gives a reliable estimation of the area of contact (A). In the model of Pharr and Oliver, the stiffness (slope of the unloading curve at the early stages of recovery) is used to estimate h_s. This step is illustrated in figure A.II.3.

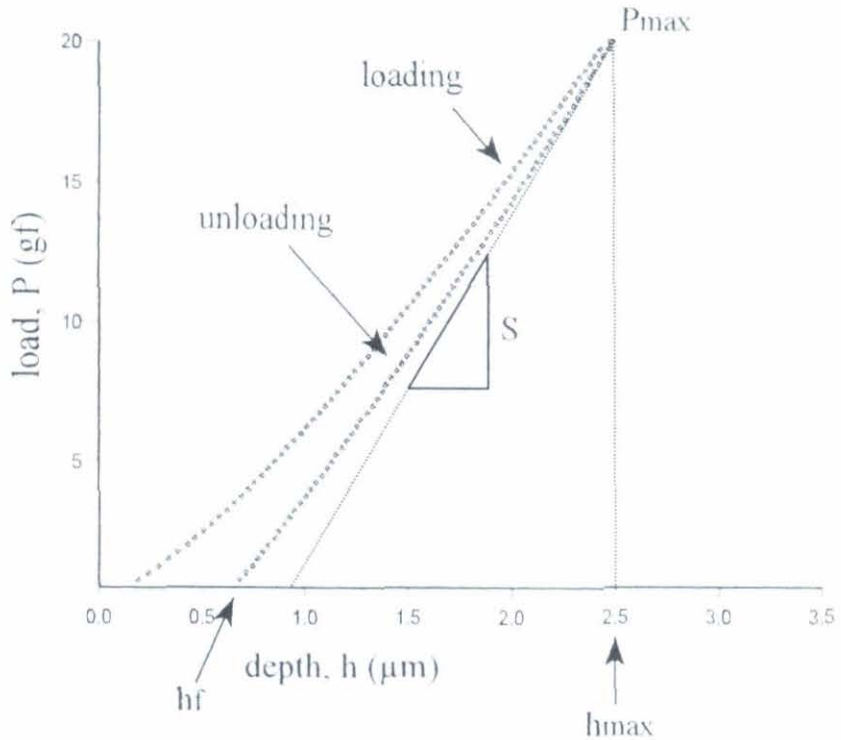

Figure A.II.3 Determination of the stiffness S from the unloading curve.

According to the model, h_s presents a linear dependence with respect to the ratio between the maximal load (P_{max}) and the stiffness, so that:

$$h_s = 0.75\frac{P_{\max}}{S} \qquad h_c = h_{\max} - h_s$$

We are interested now in determining the area of contact, which in a first approximation follows a quadratic dependence with respect to h_c. However, the refinement of this calculation requires the contribution of different order elements of h_c:

$$A = 24.5h_c^2 + \alpha h_c + \beta h_c^{1/2}$$

Where 24.5 is a specific geometrical constant for the Berkovich indenter and α and β are experimental constants. The calibration of our system by using quartz and

aluminium references leads to the values α=-1.408 and β=1.347. The hardness can be then determined by using the well known relation:

$$H = \frac{P}{A}$$

So that a value of H can be obtained for every applied load. The determination of the Young's modulus is more complicated since it requires measurements at different loads. In fact, the contribution from the Young's modulus of the indentor has usually to be accounted for, so that a reduced Young's modulus is obtained (E_r). However, the contribution of a diamond tip for the loads studied in this work can be neglected. In general, E_r presents a linear dependence with S and an inverse dependence with the square root of A, so that a study at different loads can be used to obtain an accurate value of E_r.

$$E_r = \frac{\sqrt{\pi}}{2}\frac{S}{\sqrt{A}}$$

Thus, all the relevant mechanical characteristics of a thin film can be directly related to the indentation parameters obtained from the loading-unloading indentation curves.

ANNEX III: *DIFFRACTION DATA FILES.*

84-1286 Wavelength= 1.54056 C

TiO2

Titanium Oxide

Anatase, syn

Rad.: CuKa1 λ: 1.54060 Filter: d-sp: Calculated

Cut off: 17.7 Int.: Calculated I/Icor.: 5.05

Ref: Calculated from ICSD using POWD-12++, (1997)

Ref: Burdett, J.K et al., J. Am. Chem. Soc., 109, 3639 (1987)

Sys.: Tetragonal S.G.: $I4_1/amd$ (141)

a: 3.7822(3) b: c: 9.5023(12) A: C: 2.5124

α: β: γ: Z: 4 mp:

Ref: Ibid.

Dx: 3.904 Dm: ICSD #: 202243

d(A)	Int	h	k	l
3.5140	999	1	0	1
2.4283	62	1	0	3
2.3755	190	0	0	4
2.3305	72	1	1	2
1.8911	249	2	0	0
1.6981	158	1	0	5
1.6652	155	2	1	1
1.4920	27	2	1	3
1.4795	118	2	0	4
1.3627	51	1	1	6
1.3372	55	2	2	0
1.2776	5	1	0	7
1.2635	85	2	1	5
1.2497	23	3	0	1
1.2141	1	2	0	6
1.1877	4	0	0	8
1.1713	6	3	0	3
1.1652	43	2	2	4
1.1598	18	3	1	2

Peak height intensity. R-factor: 0.000. 02 Ti type. PSC: tI12. Mwt: 79.90. Volume[CD]: 135.93.

38-1420 Wavelength= 1.54056

TiN

Titanium Nitride

Osbornite, syn

Rad.: CuKa1 λ: 1.540598 Filter: Graph Mono d-sp: Diff

Cut off: 17.7 Int.: Diffract I/Icor.:

Ref: Wong-Ng, W., McMurdie, H., Paretzkin, B., Hubbard, C., Dragoo, A., NBS, Gaithersburg, MD, USA, ICDD Grant-in-Aid, (1987)

Sys.: Cubic S.G.: Fm3m (225)

a: 4.24173(12) b: c: A: C:

α: β: γ: Z: 4 mp:

Ref: Wong-Ng, W et al., Powder Diffraction, 2, 200 (1987)

Dx: 5.388 Dm: SS/FOM: F_{10} = 176(.0057 , 10)

Color: Dark greenish brown
Peak height intensity. The mean temperature of data collection was 26.2 C. The sample was obtained from City Chemical Corporation, NY, USA. CAS #: 12033-66-8. No impurity found by SEM with Energy Dispersive Spectrometer (EDS). The structure was determined by Christensen (1). Cl Na type. Halite group. periclase subgroup. Silicon used as an internal stand. PSC: cF8. To replace 6-642 (2). Mwt: 61.91. Volume[CD]: 76.32.

d(A)	Int	h	k	l
2.4491	72	1	1	1
2.1207	100	2	0	0
1.4996	45	2	2	0
1.2789	19	3	1	1
1.2244	12	2	2	2
1.0604	5	4	0	0
.9730	6	3	3	1
.9485	14	4	2	0
.8658	12	4	2	2
.8164	7	5	1	1

84-1998 Wavelength= 1.54056 C

Ca5(PO4)3(OH)

Calcium Phosphate Hydroxide

Hydroxylapatite - from Holly Springs, Georgia, USA

Rad.: CuKa1 λ: 1.54060 Filter: d-sp: Calculated

Cut off: 17.7 Int.: Calculated I/Icor.: 1.05
Ref: Calculated from ICSD using POWD-12++, (1997)
Ref: Hughes, J.M., Cameron, M., Crowley, K.D., Am. Mineral., 74, 870 (1989)

Sys.: Hexagonal S.G.: $P6_3/m$ (176)

a: 9.4166 b: c: 6.8745 A: C: 0.7300

α: β: γ: Z: 2 mp:

Ref: Ibid.

Dx: 3.160 Dm: ICSD # : 203027

Peak height intensity. R-factor: 0.016. PSC: hP44. Mwt: 502.32. Volume[CD]: 527.91.

2θ	Int	h	k	l	2θ	Int	h	k	l
10.840	171	1	0	0	45.361	35	2	0	
16.854	47	1	0	1	46.418	8	4	0	
18.832	24	1	1	0	46.730	283	2	2	
21.778	63	2	0	0	48.118	131	3	1	
22.874	63	1	1	1	48.626	41	3	2	
25.376	26	2	0	1	49.526	311	1	2	
25.900	360	0	0	2	50.516	161	3	2	
28.150	91	1	0	2	51.297	125	4	1	
28.944	174	1	2	0	52.116	125	4	0	
31.790	999*	1	2	1	52.116	125	3	0	
32.218	532	1	1	2	53.256	137	0	0	
32.922	614	3	0	0	54.521	10	1	0	
34.087	209	2	0	2	55.907	56	2	3	
35.482	42	3	0	1	55.907	56	2	2	
38.198	2	2	2	0	56.364	1	5	0	
39.226	57	1	2	2	57.177	38	1	3	
39.822	215	3	1	0	58.075	19	5	0	
40.468	16	2	2	1	58.206	13	2	0	
40.873	3	1	0	3	58.342	14	1	4	
42.019	63	3	1	1	58.787	7	3	3	
42.356	11	3	0	2	59.975	42	4	2	
43.906	45	1	1	3	60.454	34	3	3	
44.397	10	4	0	0	61.623	32	4	2	

2θ	Int	h	k	l	2θ	Int	h	k	l
61.749	46	2	1	4	87.415	24	1	5	4
63.033	82	5	0	2	87.564	38	4	4	2
63.458	18	1	5	0	87.564	38	1	1	6
64.046	74	3	0	4	88.096	25	3	2	5
64.216	94	2	3	3	88.554	63	5	3	2
65.055	72	1	5	1	89.614	1	6	1	3
66.425	25	2	4	2					
66.425	25	1	4	3					
67.411	1	2	2	4					
68.514	3	1	3	4					
69.045	2	6	0	0					
69.243	1	1	0	5					
69.732	20	1	5	2					
70.135	5	3	4	0					
70.857	1	5	0	3					
71.414	4	1	1	5					
71.658	39	3	4	1					
72.295	34	2	5	0					
72.490	20	2	0	5					
73.008	3	3	3	3					
73.799	21	2	5	1					
74.074	39	4	2	3					
74.977	14	3	2	4					
75.096	11	6	0	2					
75.680	45	1	2	5					
76.151	31	4	3	2					
76.542	19	1	6	0					
77.083	49	4	1	4					
77.240	41	1	5	3					
77.780	2	3	0	5					
78.017	9	6	1	1					
78.249	61	5	2	2					
80.901	2	2	2	5					
81.248	5	5	0	4					
81.748	17	4	4	0					
81.936	11	3	1	5					
82.398	6	6	1	2					
82.398	6	6	0	3					
82.781	7	5	3	0					
83.200	11	4	4	1					
83.311	11	3	3	4					
83.466	36	3	4	3					
84.340	32	4	2	4					
84.489	16	0	0	6					
85.023	2	4	0	5					
85.519	21	2	5	3					

REFERENCES.

ANS00/ K. Anselme. Osteoblast adhesion on biomaterials. Biomaterials 21;2000:667.

ARF84/ N.J. Arfsten. Sol-gel derived transparent IR-reflecting ITO semiconductor coatings and future applications. J Non Cryst Solids 63;1984:243-9.

BAL98/ A.R. Bally, P. Hones, R. Sanjines, P.E. Schmid, F. Levy. Mechanical and electrical properties of fcc TiO_{1+x} thin films prepared by r.f. reactive sputtering. Surf Coat Technol 1-3;1998:166-170.

BAR96/ A. Barna, M. Menyhard. Study of low energy atomic mixing by means of Auger depth profiling, XTEM and TRIM simulation on Ge/Si multilayer system. Surf Interf Anal 24;1996:476-480.

BAS90/ V.A. Basyuk, A.A. Chuiko. Infrared spectra of amide products formed during the chemisorption of α-amino acid vapors on the surface of α-aminopropyl-aerosil. Zhurnal Prikladnoi Spektroscopii 52;1990:935.

BEE81/ M. Beer, R.W. Carpenter, C.E. Leyman, J.M. Thomas, L. Eyring. High resolution microscopy. Chem Eng News 17;1981:40-61.

BEN00/ A. Bendavid, P.J. Martin, H. Takikawa Deposition and modification of titanium dioxide thin films by filtered arc deposition. Thin Solid Films 360;2000:241-249.

BLA98/ A.S. Blawas, W.M. Reichert. Review: protein patterning. Biomaterials 19;1998: 595-609.

BRA78/ D.C. Bradley, R.C. Mehrotra, D.P. Gaur. Metal Alkoxides, Academic Press, London (1978)

BRE92/ T. Brendel, A. Engel, C. Rüssel. Hydroxyapatite coatings by a polymeric route. J Mater Sci: Mater Med 3;1992:175-179.

BRI90/ C.J. Brinker, G.W. Scherrer. The Physics and chemistry of sol-gel Science, Academic Press, San Diego (1990).

BRO97/ R.A. Brown, K.D. Smith, D.A. McGrouther. Strategies for cell engineering in tissue repair. Wound Rep Regen 5;1997:212-221.

BRU98/ S.P. Bruder, A.A. Kurth, M. Shea, W.C. Hayes, N. Jaiswal, S. Kadiyala. Bone regeneration by implantation of purified cultured-expanded human mesenchymal stem cells. J Orthop Res 16;1998:155.

BUR00/ 5 F. Burny, D. Muster, M Donkerwolcke, M. Magerat-Burny. Aspects of reconstructive biomaterials. Mater Res Soc Bull 25;2000:15-17.

BUR01/ M. Burgos. These Doctorale. INP Grenoble. 2001

BUR99/ M. Burgos, M. Langlet. The sol gel transformation of TIPT coatings: a FTIR study. Thin Solid Films 1999;349;19-23.

CAP91/ A.I. Caplan. Mesenchymal stem cells. J Orthp Res 9;1991:641.

CHE98/ J.S. Chen, H.Y. Juang, M.H. Hon. Calcium phosphate coating on titanium substrate by a modified electrocrystallization process. J Mat Sci: Mat Med 9;1998:297-300.

CHE99/ Q. Chen, F. Miyaji, T. Kokubo, T. Nakamura. Apatite formation on PDMS modified CaO-SiO2-TiO2 hybrids prepared by the sol-gel process. Biomaterials 20;1999:1127-1132.

CHU78/ W.R. Chu, J.M. Mayer, M.A. Nicolet. Backscattering Spectroscopy. Academic Press, New York (1978).

CHU99/ J.S. Chun, I. Petrov, J.E. Green. Dense fully 111-textured TiN difusion barriers: Enhanced lifetime through microstructure control during layer growth. J Appl Phys 86;1999:3633-41.

COU00/ C. Coutier, M. Audier, J. Fick, R. Rimet, M. Langlet. Aerosol-gel preparation of optically active layers in the system Er/SiO2-TiO2. Thin Solid Films 372;2000:177-189.

COU01/ C. Coutier. These Doctorale. INP Grenoble. 2001

CRI91/ R. von Criegern. Scanning electron Auger spectroscopy. In: Analysis of microelectronic materials and devices. Wiley. Chichester. (1991).

CUI00/ F.Z. Cui, D.J. Li. A review of investigations on biocompatibility of diamond-like carbon and carbon nitride films. Surf Coat Technol 131;2000:481-7.

DEP92/ Deptula, W. Lada, T. Olczak, A. Borello, C. Alvani, A. di Bartolomeo. Preparation of spherical powders of hydroxyapatite by sol-gel process. J Non-Cryst Solids 147&148;1992:537-541.

DIO93/ Dion I, Roques X, More N, Labrousse L, Caix J, Lefebre F, Rouais F, Gautreau J, Baquey Ch. Ex vivo leucocyte adhesion and protein adsorption on TiN. Biomaterials 14;1993:712-17.

DOO85/ L.R. Doolitle. Algorithms for the rapid simulation of Rutherford Backscattering Spectra. Nucl Instr Meth Phys Res 9;1985:344-355.

EBR93/ A. Ebrahimpour, M. Johnsson, C.F. Richardson, G.H. Nancollas. The characterisation of hydroxyapatite preparations. J Coll Interf Sci 159;1993:158-163.

ELL94/ J.C. Elliot, Hydroxyapatite and nonstoichiometric apatites, pp. 145-46, In: Structure and chemistry of the apatites and other calcium orthophosphates, Elsevier, Amsterdam, (1994).

FER01/ M. Fernández. Personal databases. 2001.

FOW74/ B.O. Fowler. Infrared studies of apatites I: vibrational assignments for calcium, strontium and barium hydroxyapatites utilising isotopic substitutions. Inorg Chem 13;1974:194-214.

FRO81/ F.W. Froben, F. Rogge. Matrix infrarred measurement of TiN. Chem Phys Lett 78;1981:264-265.

GAN89/ S. Gangully. FTIR studies on the interaction of cis-9-octadecenylamine in solution and on a salt surface. Spectrochimica Acta 45A;1989:171.

GAR97/ J. García, V.M. castaño, M.A. Mondragón, E. Ramírez, F. González, A. Campero, V. Rantería. UV radiation effects on SiO2 gels doped with organic dyes. J Sol-gel Sci Tech 8;1997:911-916.

GLA79/ A.B. Glaser, G.E. Subak-Sharpe. Integrated circuit engineering: design, fabrication, and applications. Addison-Wesley, London (1979).

GOO88/ P.J. Goodhew, F.J. Humphreys, Electron Microscopy and Analysis, Taylor & Francis (1988).

GRA01/ http://www2.cbm.uam.es/confocal/Graficofluoroforos.htm

GRO98/ K.A. Gross, C.C. Berndt, P. Stephens, R. Dinnebier, Oxyapatite in Hydroxyapatite coatings, J Mater Sci 33;1998:3985-3991.

GUI96/ O. Guillot-Noël, R. Gómez-San Roman, J. Perrière, J. Hermann, V. Craciun, C. Boulmer-Leborgne. Growth of apatite films by laser ablation: reduction of the droplet areal density. J Appl Phys 80;1996:1803-1808.

GUO96/ Y. Guo, P. Woznicky, A. Barkart, Sol-gel synthesis of microcrystalline rare earth orthophosphates. J Mater Res 11;1996:639.

GUT99/ A. Gutierrez Llorente. SiO_xN_y crecidos por sputtering reactivo. Tesis Doctoral. UAM 1999.

HAD96/ D.B. Haddow, S. Kothari, P.F. James, R.D. Short, P.V. Hatton, R. Van Noort. Synthetic implant surfaces 1. The formation and characterisation of sol-gel titania films. Biomaterials 17;1996:501-507.

HAD96-2/ D.B. Haddow, P.F. James, R. Van Noort, Characterisation of sol-gel surfaces for biomedical applications. J Mater Sci: Mater Med 7;1996:255-260.

HAY94/ K. Hayashi, T. Inadome, H. Tsumura, Y. Nakashima, Y. Sugioka. Effect of surface roughness of hydroxyapatite coated titanium on the bone implant interface shear strength. Biomaterials 15;1994:1187-1191.

HAY99/ T. Hayashi, A. Matsumuro, M. Muramatsu, Y. Takahashi, K. Yamaguchi. Synthesis of TiN thin films prepared by dynamic ion mixing technique and their mechanical properties. Thin Solid Films 349;1999:199-204.

HEN82/ L.L. Hench, E.C. Etheridge, Biomaterials, an interfacial approach. Academic Press, New York, 1982.

HEN91/ L.L. Hench. Bioceramics, from concept to clinics. J Am Ceram Soc 74;1991:1487.

HID70/ G.M. Hidy, J.R. Brock. The dynamics of aero-colloidal systems, Pergamon, New York, (1970)

HUA92/ J. Huaxia, C.B. Ponton, P.M. Marquis. Microstructural characterization of hydroxyapatite coating on titanium. J Mater Sci: Mater Med 3;1992:283-287.

HUB93/ R. Hübler, A. Schröer, W. Ensinger, G. Wolf, F.C. Stedile, W.H. Shreiner, I.J.R. Baumvol. Corrosion behavior of steel coated with thin film TiN/Ti composites. J Vac Sci Technol 11;1993:451-453.

HWA99/ K. Hwang, Y. Lim. Chemical and structural changes of hydroxyapatite films by using a sol-gel method. Surf Coat Tech 115;1999:172-175.

JAM98/ A.K. Jamting. J.M. Bell, M.V. Swain, L.S. Wielunski, R. Clissold. Measurement of the micromechanical properties of sol-gel TiO2 films. Thin Solid Films 332;1998:189-194.

JAR91/ M.Y. Al-Jaroudi, H.T.G. Hentzell, S. Gong, A. Bengston. The influence of titanium nitride magnetron sputtering on hardened tool steel surfaces. Thin Solid Films 195;1991:63-76.

JIL99/ A. Jillavenkatesa, D.T. Hoelzer, R.A. Condrate. An electron microscopy study of the formation of hydroxyapatite through sol-gel processing. J Mater Sci 34;1999:4821-4830.

JIM88/ B. Jimenez, J. Mendiola, C. Alemany, L. Del-Olmo, L. Pardo, E. Maurer, M.L. Calzada, J. De-Frutos, A.M. Gonzalez, M.C. Fandino. Contributions to the knowledge of calcium-modified lead titanate ceramics. Ferroelectrics 87;1988:97-108.

JIM91/ C. Jiménez- Arévalo. Estudio del comportamiento del nitruro de titanio como barrera de difusión. Estabilidad y cinética de oxidación. Tesis Doctoral. UAM 1991.

JIM99/ C. Jiménez, C. Sánchez-Fernández, M. Fernández, J. Sánchez Olías, C. Morant, J.M. Martínez Duart. Dependence of the mechanical and structural properties of (Ti,Al)N films on the nitrogen content. J Mater Res 14;1999:2830-37.

JON99/ M.I. Jones, I.R. McColl, D.M. Grant, K.G. Parker, T.L. Parker. Haemocompatibility of DLC and TiC-TiN interlayers on titanium. Diamond Rel Mater 8;1999:457-62.

KAO99/ W.J. Kao. Evaluation of protein modulated macrophage behaviour on biomaterials: designing biomimetic materials for cellular engineering. Biomaterials 20;1999:2213-21.

KIV98/ N. Kivrak, A.C. Tas, Synthesis of Hydroxyapatite- Tricalcium Phosphate (HA-TCP) Composite bioceramic powders and their sintering behavior. J Am Ceram Soc 81;1998:2245-52.

KOL85/ M. Kolb, H.J. Herrmann. The sol-gel transition modelled by irreversible aggregation of clusters. J Phys A (Mathem Gen) 18;1985:435-41.

KON97/ H. Kondo. Effect of double bonds on friction in the boundary lubrication of magnetic thin film media. Wear 202;1997:149.

LAN01/ M. Langlet, M. Burgos, C. Coutier, C. Jimenez, C. Morant, M. Manso. Low temperature preparation of high refractive index and mechanically resistant sol-gel TiO_2 layers for multilayer antireflective coating applications. J Sol Gel Sci Technol. In press.

LAN89/ G.L. Lange, K. Donath. Interface between bone tissue and implants of solid hydroxyapatite or hydroxyapatite-coated titanium implants. Biomaterials 10;1989:121-25.

LAN91/ M. Langlet, J.C. Joubert, European Patent 0486393 A1 (1991).

LAN95/ R. Langer. Biomaterials: Novel polymers and novel applications. Mater Res Soc Bull 20;1995:18-22.

LEN96/ D.P. Lennon, S.E. Haynesworth, S.P. Bruder, N.J. Jaiswal, A.I. Caplan. In Vitro Cell Dev Biol 32;1996:602.

LI93/ P. Li, I. Kangasniemi, K. De Groot. In vitro and in vivo evaluation of bioactivity of Gel Titania. Bioceramics 6;1993:41-45.

LI96/ T. Li, J. Lee, T. Kobayashi, H. Aoki, Hydroxyapatite coating by dipping method, and bone bonding strength. J Mater Sci: Mater Med 7;1996:355-357.

LI99/ C.Y. Li, Y. Donghang, S.Z.D. Cheng, B. Feng, J.J. Ge, B.H. Calhoun, H. Tianbai, C.C. Liang, F.W. Harris, B. Lotz. Helical single-lamellar crystals thermotropically formed in a synthetic non-ceramic chiral main-chain polyester. Phys Rev B 60;1999:12675-80.

LIN01/ P.I. Lin, C.W. Liu, C.C. Hsieh, K.H. Wu, J.Y. Juang, T.M. Uen, J.Y. Lin, Y.S. Gou. Characteristics of YBa2Cu3O7 thin films deposited on substrates buffered by various TiO2 layers. Jap J Appl Phys (lett) 40;2001:377-9.

LIV88/ Livage, M. Henry, C. Sanchez. Partial charges in sol-gel chemistry. Progr Sol State Chem. 18;1988:259.

LIV89/ J. Livage, C. Sanchez, M. Henry, S. Doeuff, The chemistry of the sol-gel process. Sol State Ionics, Diff React 32-33;1989:633-8.

LIV92/ J. Livage, P. Barboux, M.T. Vandenborre, C. Schmutz and F. Taulelle. Sol-gel synthesis of phosphates. J Non-Cryst Solids 147&148;1992:18-23.

LJU96/ H. Ljungcrantz, M. Odén, L. Hultman, J.E. Green, J.E. Sundgren. Nanoindentation studies of single crystal (001), (011) and (111) oriented TiN layers on MgO. J Appl Phys 1996;80:6725-33.

LON98/ M. Long, H.J. Rack. Titanium alloys in total joint replacement- a materials science perspective. Biomaterials 19; 998:1621-1639.

LU00/ G.Q. Lu, J. N. Calata, Adhesion strength of cordierite glass ceramic coatings on molybdenum substrates. J Mater Res 15;2000:2857-2863.

MAJ99/ B. Major, R. Ebner, P. Zieba, W. Wolzynski. Titanium-based films deposited using a Nd:YAG pulsed laser. Appl Phys-A 69;1999;921-3.

MAN00/ M. Manso, C. Jiménez, C. Morant, P. Herrero, J.M. Martinez-Duart. Electrodeposition of hydroxyapatite coatings in basic conditions. Biomaterials 21;2000:1755.

MAN01/ M. Manso, L. Fuentes Cobas, R. J. Martín Palma, M. Hernández Vélez, J. M. Martínez-Duart. BaTiO3 thin films obtained by sol-gel spin coating. Surf Coatings Tech, In press.

MAN99/ F.K. Mante, G.R. Baran, B. Lucas. Nanoindentation study of titanium single crystals. Biomaterials 20;1999:1051-1055.

MAR92/ P. Marage. Contribution à la mise au point du procedé aerosol-gel; application au depot de couches minces optiques dans le système SiO_2 TiO_2. These Doctorale. INP Grenoble. 1992.

MAR00/ R. Martín-Palma. Caracterización y desarrollo de estructuras nanométricas de silicio para aplicaciones optoelectrónicas. Doctoral Thesis, DFA- UAM. 2000.

MAS90/ Y. Masuda, K. Matubara, S. Sakka. Synthesis of Hydroxyapatite from metal alkoxides through sol-gel technique. J Ceram Soc Jap 98;1990:1255-66.

MAS91/ Y. Masuda, T. Tateishi, K. Matsubara, R. Ogawa, Y. Kawate. Preparation of YBCO superconductive film using sol-gel method. Jap J Appl Phys. Part1. 30;1991:1390-7.

MAT77/ H.J. Mathieu, J.B. Mathieu, D.E. McClure, D.Landolt. Beam effects in Auger electron spectroscopy analysis of titanium oxide films. J Vac Sci Tech 14;1977:1023-28.

MAV00/ B. Mavis, A.C. Tas. Dip coating of calcium hydroxyapatite on Ti-6Al-4V substrates. J Amer Ceram Soc 83;2000:989-91.

MAY92/ L. Mayer, H. Heinzelman. Scanning Force Microscopy. Springer Verlag Series in Surface Science, Vol 28-4, Berlin Heidelberg (1992).

MCH00/ K.P. McHugh, D.K. Hodivala, M.H. Zheng, N. Namba, J. Lam, D. Novack, X. Feng, F.P. Ross, R.O. Inés, S.L. Teitelbaum. Mice lacking beta3 integrins are osteosclerotic because of dysfunctional osteoclasts. J Clin Invest 105;2000:433.

MIR00/ C.A. Mirkin, A DNA-based methodology for preparing nanocluster circuits, arrays, and diagnostic materials. MRS Bull 25;2000;43-56.

MIT98/ A. Mitsuo, S. Uchida, N. Nihira, M. Iwaki. Improvement of high-temperature oxidation resistance of titanium nitride and titanium carbide films by aluminum ion implantation. Surf and Coat Tech 103-104;1998;98-103.

NAK97/ K. Nakamoto, Infrarred and Raman spectra of inorganic and coordination compounds: Part A, p. 182 John Wiley & Sons, New York, (1997)

NYQ97/ R.A. Nyquist, R.O. Kagel, Infrared spectra of inorganic compounds, pp. 206-207 Academic Press, San Diego, (1997).

OGU00/ S. Ogueta, I. Olaizabal, I. Santos, E. Delgado-Baeza, J.P. García Ruiz. J Endocrinology 165;2000:329.

OHB99/ Y. Ohba, T. Watanabe, E. Sakai, M. Daimon. Coating of Hap/$CaTiO_3$ coating on titanium substrates by hydrothermal method. J Ceram Soc Japan 107; 1999:907-912.

OLI92/ W.C. Oliver, G.M. Pharr, An improved technique for determining hardness and elastic modulus using load and displacement sensing indentation experiments. J Mater Res 7;1992:1564-83.

ONG/98 J.L. Ong, L.C. Lucas. Auger electron spectroscopy and its use for the characterisation of titanium and hydroxyapatite surfaces. Biomaterials 19;1998:455-464.

PAR92/ J.B. Park, R.S. Lakes. Biomaterials: An Introduction. Plenum Publishing Corporation. New York (1992).

PAR95/ K.C. Park, K.B. Kim. Effect of annealing of TiN on the diffusion barrier property in Cu metallization. J Electrochem Soc 142;1995:3109-15.

PER95/ J. Pérez Rigueiro. Tesis Doctoral. UAM 1995.

POL86/ H.M. Pollock, D. Maugis, M. Barquins. Characterisation of submicrometre surface layers by indentation. In: Microindentation techniques in materials science and engineering. American Society for testing materials, Philadelphia, 1986;47-72.

PUG94/ M. Puggeli, G. Gabrielli, G. Caminati. Langmuir-Blodget monolayers and multilayers of stearic acid and staryl amine. Thin solid films 244;1994:1050.

RAD92/ S.R. Radin, P. Ducheyne. Plasma spraying induced changes of calcium phosphate ceramic characteristics and the effect on in vitro stability. J Mater Sci: Mater Med 3;1992:33-42.

RAE84/ W. Van Raemdonck, P. Ducheyne, P. De Meester. Auger electron spectroscopy of hydroxyapatite coatings on titanium. J Am Ceram Soc 67;1984:381-4.

RAM91/ M.M.A. Ramselaar, F.C.M. Driessens, W. Kalk, J.R. De Wijn. Biodegradation of four calcium phosphate ceramics; in vivo rates and tissue interactions. J Mater Sci: Mater Med 2;1991:63-70.

RED91/ J. Redepenning, T. Schlessinger, S. Burnhum, L. Lipiello, J. Miyano. Characterization of electrolytically prepared brushite and hydroxyapatite coating on orthopaedic alloys. J Biomed Mat Res 30;1996:287-294.

ROD96/ M.T. Rodrigo Rodríguez. Caracterización de Películas delgadas mediante la técnica de nanopenetración. Degree in Physics. 1996

RHO97/ J.Y. Rho, T.Y. Tsui, G.M. Pharr. Elastic properties of human cortical and trabecular lamellar bone measured by nanoindentation. Biomaterials 18;1997:1325-1330.

RIE95/ K.T. Rie, T. Stucky, R.A. Silva, E. Leitao, K. Bordji, J.Y. Jouzeau, D. Mainard. Plasma surface treatment and PACVD on Ti alloys for surgical implants. Surf Coat Technol 32;1995:973-80.

ROK00/ P. Rokkanen, O. Bostman, E. Hirvensalo, E.A. Makela, E.K. Partio, H. Patiala, K. Vihtonen, S. Vainionpaa, P. Tormala. Totally biodegradable implants for bone fixation and ligament repair. Mater Res Soc Bull 25;2000:21-24.

ROS84/ C. Rossington, A.G. Evans, D.B. Marshal, Y. Khuri. Measurements of adherence of residually stressed thin films by nanoindentation I. Mechanics of interface delamination. J Appl Phys 56;1984:2632-38.

RUG90/ D. Rugar, P. Hansma. Atomic Force Microscopy. Physics Today 10;1990:412.

RUS96/ S.W. Russell, K.A. Luptak, C. Tres, A. Suchicital, T.L. Alford, V.B. Pizziconi. Chemical and structural evolution of sol-gel derived hydroxyapatite thin films under rapid thermal processing. J Amer Ceram Soc 79;1996:837-842.

SAM86/ L.E. Samuels. Microindentations in Metals. In: Microindentation techniques in materials science and engineering. American Society for testing materials, Philadelphia, 1986;5-25.

SCH90/ G.W. Scherrer, C.J. Brinker, Sol-Gel Science: The Physics and Chemistry of Sol-Gel, Academic Press, Boston MA, 1990.

SCH95/ M. Schlaldach. New aspects in electrostimulation of the heart. Med Prog Technol 21;1995:1-16.

SCH98/ H. Schmidt, C. Konetschny, U. Fink. Electrochemical behaviour of ion implanted Ti6Al4V in Ringer´s solution. Mater Sci Tech 14;1998:592-8.

SER99/ R.F. Service. Neurons and silicon get intimate. Science 284;1999:23-24.

SOK86 R. Sokoll, H. Hobert, I. Schmuck. Thermal desorption and infrared studies of butylamine adsorbed on SiO2, Al2O3, and CaO. J Chem Soc, Faraday Trans 82;1986:3391.

SOU96/ S.R. Sousa, M.A. Barbosa. Effect of hydroxyapatite thickness on metal ion release from Ti6Al4V substrates. Biomaterials 17;1996:397-404.

SZA99/ G. Szabo, L. Kovacs, K. Vargha, J. Barabas, Z. Nemeth, A new advanced surface modification technique- titanium oxide ceramic surface implants: the background and long term results. J Long Term Effects Med Impl 3;1999:247-259.

TAL98/ R.V. Talroze, T.L. Lebedeva, G.A. Shandryuk, N.A. Plate, N.D. Stepina, L.G. Yanusova, L.A. Feigin. Ordering phenomena in composite monolayers and Langmuir Blodget films. Thin solid films 325;1998:232.

TEM00/ J.S. Temenoff, A.G. Mikos. Review: tissue engineering for regeneration of articular cartilage. Biomaterials 21;2000:431-440.

TJI00/ J.S. Tjia, B.J. Aneskievich, P.V. Moghe. Substrate adsorbed collagen and cell secreted fibronectin concertedly induce cell migration on poly(lactide-glycolide) substrates. Biomaterials 20;2000:2223-2233.

TOR87/ E. Török, J. Perry, L. Chollet, W.D. Sproul. Young modulus of TiN, TiC, ZrN, and HfN. Thin Solid Films 153;1987:37-43.

TOR93/ L. Torrisi, R. Setola. Thermally asisted hydroxyapatite obtained by pulsed laser deposition. Thin solid Films. 227;1993:32-36.

TOR95/ F. Torregrosa, L. Barrallier, L. Roux. Phase analysis, microhardness and tribological behaviour of Ti6Al4V after ion implantation of nitrogen with its application for hip-joint prosthesis. Thin Solid Films 2;1995:245-53.

TRE00/ M. Trejo. Projet de These. INP Grenoble 2000.

VAS95/ L.L. Vasiljeva, F.N. Dultsev, A.H. Milekhin. IR spectroscopic study of SO2 adsorption on polysiloxane layers containing tertiary amino groups. Thin Solid Films 261;1995:296-298.

VAU98/ C. Vautey. Depot aerosol-gel et characterisation FTIR de couches minces de sílice. These Doctorale. INP Grenoble. 1998

VII00/ R.I. Viitala, M. Langlet, J. Simola, M. Lindén, J.B. Rosenholm. Aerosol-gel deposition of doped titania thin films. Thin Solid Films 2000;368;35-40.

WAI78/ R.K. Waits. Planar magnetron sputtering. In: Thin film processes. Academic press. San Diego. (1978)

WEI99/ S. Weiner, A. Veis, E. Beniash, T. Arad, J.W. Dillon, B. Sabsay, F. Siddiqui. Peritubular dentin formation: crystal organisation and the macromolecular constituents of human teeth. J Struct Biol 126;1999:27-41.

WEN99/ W. Weng, J. Lopes Baptista, Preparation and characterization of hydroxyapatite coatings on Ti6AL4V alloy by a sol-gel method. J Amer Ceram Soc 82;1999:27-32.

WHI94/ J.K. Whitesell, H.K. Chang. Surface oriented polymers for non linear optics. Mol Cryst Liq Cryst 240;1994:251.

WIL85/ R.H. Williams, I.T. McGovern. Surface characterisation of InP. Surf Sci 149;1985: 20-5.

WIL90/ D. Williams. Medical and Dental Materials. Pergamon press, Oxford, 1990.

WIL96/ G. Willmann. Medical grade hydroxyapatite: state of the art, Brit Ceram Transact 95;1996:212-216.

YAM88/ K. Yamaguchi, T. Fujii, S. Kuranouchi, A. Kaneko. Fabrication of transparent iron-oxide films by means of sol-gel synthesis. J Appl Phys 64;1988:5452.

YAM94/ K. Yamashita, T. Arashi, K. Kitagaki, S. Yamada, T. Umegaki, K. Ogawa. Preparation of apatite thin films through rf-sputtering from calcium phosphate glasses. J Am Ceram Soc 77;1994:2401-2407.

ZHA98/ L. Zhang, Z. Bo, B. Zhao, Y. Wu, X. Zhang, J. Shen. Dendritic growth strategies for construction of ultrathin organic films on solid substrate. Thin solid Films 221;1998:327-329.

ZHO96/ B.L. Zhou. Some progress in the biomimetic study of composite materials. Mater Chem Phys 45;1996:114-19.

ZUS90/ R. Zusman, C. Rottman, M. Ottolenghi, D. Avnir. Doped sol-gel glasses as chemical sensors. J Non-Cryst Solids. 122;1990:107-9.

Reunido el tribunal que suscribe en el día de la fecha, acordó calificar la presente Tesis doctoral con SOBRESALIENTE CUM LAUDE (UNANIMIDAD)

MADRID 21 DE NOVIEMBRE DE 2001

F. Agulló